UNIVERSITY OF HAWAII LIBRARY

4212

THERMAL AND HYDRAULIC PERFORMANCE OF SINGLE-PHASE AND TWO-PHASE MICRO-CHANNEL HEAT SINKS

A THESIS SUBMITTED TO THE GRADUATE DIVISION OF THE UNIVERSITY OF HAWAI'I IN PARTIAL FULFILLMENT OF THE REQUIREMENTS FOR THE DEGREE OF

MASTER OF SCIENCE

IN

MECHANICAL ENIGINEERING

AUGUST 2007

By
Scott W. C. H. Lee

Thesis Committee:

Weilin Qu, Chairperson
Alexandre K. da Silva
Marcelo H. Kobayashi

We certify that we have read this thesis and that, in our opinion, it is satisfactory in scope and quality as a thesis for the degree of Master of Science in Mechanical Engineering.

THESIS COMMITTEE

Chairperson

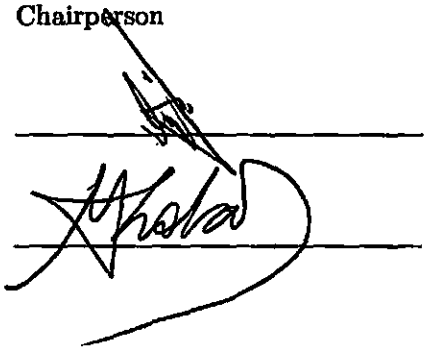

© Copyright 2007
by
Scott W. C. H. Lee
All Rights Reserved

Acknowledgements

I would like to acknowledge first, and foremost, Dr. Weilin Qu, my advisor and committee chair. It is because of his support and guidance that allowed me accomplish what I have so far and his teachings which will allow me accomplish so much more. I have experienced and learned many things in these past two years of which I am very grateful. I also want to acknowledge the support from Dr. da Silva and Dr. Kobayashi who have helped in many of technical aspects of my research through the various classes I have taken from them.

I would also like to acknowledge my fellow graduate students who have helped me and encouraged me to keep going: Abel, Jasen, Kin Wai, Hugo, Chris, Ruey, Victor, Qian, and extra kudos to Lynnette and Lance for their help with using LATEX to write this thesis.

I would also like to acknowledge financial support from Trex Enterprises and Pipeline Communications and Technology for funding my research.

Abstract

The hydraulic and thermal performance for single-phase and two-phase heat sinks are examined. One-dimensional (1D), three-dimensional (3D), and two-dimensional (2D) approaches to analyze heat sink in single-phase micro-channel heat sinks were investigated. A 1D model is very simple and quick and can give good results under certain circumstances such as a thin heat sink base substrate. A 3D numerical analysis can provide detailed and accurate information of temperature distribution, but can be time consuming. A new 2D model was developed and found to be a good compromise for speed and accuracy. A systematic thermal design methodology was developed for both single-phase and two-phase micro-channel heat sinks under a low fixed liquid coolant flow rate. A single-phase micro-channel heat sink experimental system was designed, fabricated, and tested. The design for the heat sink test section was comprised of two pieces, heater and heat sink, which lead to an interface resistance which increased the temperatures that were recorded in the heater. Using a combination of the 2D and 1D models the temperature distributions within the test heater could be found. Results from the experiment show a good agreement with the model predictions. Finally a design of a two-phase heat sink testing system was performed. The two-phase heat sink will use FC-72 fluorinert as the coolant. This fluid has a lower boiling temperature of 56 degree, which will be better for electronic components than water. The fluid is also dielectric and so any leaks from the fluid onto electronic components will not do any damage. Design of the test section will incorporate the use of a single piece combining the heater and heat sink to avoid any issues of interface contact resistance. Designs for the enhanced micro-structure and flow loop components were done.

Table of Contents

Acknowledgements iv

Abstract v

List of Tables ix

List of Figures x

Nomenclature xvi

Chapter 1: Introduction 1

1.1 Background 1

1.2 Research Objectives 6

Chapter 2: One-Dimensional Modeling and Three-Dimensional Numerical Analysis of Single-Phase Heat Sinks 7

2.1 One-Dimensional Modeling 7

2.1.1 Major Assumptions 7

2.1.2 Temperature Distribution 8

2.1.3 Determination of Nusselt Number 10

2.1.4 Calculation Procedure 11

2.2 Three-Dimensional Numerical Analysis 11

2.3 Results and Discussion 13

2.3.1 Effect of Substrate Thickness, H_w 13

2.3.2 Effect of Reynolds Number, Re 14

2.3.3 Effect of Heat Flux, q''_{eff} 14

2.3.4 Effect of Substrate Material, k_s 14
2.4 Summary 21
Chapter 3: New Two-Dimensional Modeling of Single-Phase Heat Sinks 22
3.1 2-D Numerical Model 22
3.1.1 Objective 23
3.1.2 Model Setup 23
3.1.3 Grid 25
3.1.4 Solution Technique 26
3.2 Results and Discussion 26
3.3 Summary 27
Chapter 4: Thermal Design of Single-Phase and Two-Phase Heat Sinks Using One-Dimensional Model 35
4.1 Heat Sink Parameters 35
4.1.1 Geometrical Parameters 36
4.1.2 Operating Parameters 37
4.1.3 Thermal/Fluid Parameters 37
4.1.4 Characterstics of Heat Sink Parameters 43
4.2 Heat Sink Thermal Design 49
4.2.1 Single-phase heat sink 49
4.2.2 Two-phase heat sink 50
4.3 Summary 53
Chapter 5: Design, Fabrication, and Testing of a Water Cooled Single-Phase Heat Sink 58
5.1 Design Parameters 58
5.2 Experimental Design 59
5.2.1 Test Heater Design 59
5.2.2 Bulk Heat Sink Design 59
5.2.3 Micro-Channel Design 60
5.3 Experimental System 61

5.3.1 Micro-Channel Heat Sink Test Section 61
5.3.2 Flow Loop 76
5.3.3 Instrumentation 78
5.3.4 Construction 84
5.4 Results and Discussion 94
5.4.1 Experimental Error 94
5.4.2 Experimental Results 94
5.5 Summary 101
Chapter 6: Design of a FC-72 Cooled Two-Phase Heat Sink 102
6.1 Design Parameters 102
6.1.1 Geometrical Parameters 102
6.1.2 Operating Parameters 103
6.1.3 Thermal Fluid Parameters 104
6.2 Experimental Design 110
6.2.1 Fluid Properties 110
6.2.2 Test Section Design 115
6.2.3 Flowloop Design 122
6.2.4 Pump 122
6.2.5 Instrumentation Cart 124
6.3 Summary 124
Chapter 7: Conclusions 128
Appendix: Predictive tools for single-phase and two-phase micro-channel heat sinks 130
A.1 Single-phase 130
A.1.1 Heat transfer coefficient 130
A.1.2 Pressure drop components 131
A.2 Two-phase 132
A.2.1 Saturated flow boiling heat transfer coefficient 132
A.2.2 Pressure drop components 133

A.2.3 Critical heat flux CHF 134

List of Tables

2.1 Heat sink geometrical parameters 13

2.2 Key properties 15

5.1 Heat sink geometrical parameters 95

List of Figures

1.1 Typical micro-channel heat sink construction. 3

1.2 Stream-wise temperature profile for (a) single-phase and (b) two-phase heat sinks. 5

2.1 Comparison of Nusselt numbers 12

2.2 1D and 3D temperature distribution of the substrate base, channel bottom wall, and bulk fluid temperature for copper substrate (k_s=401), H_w = 50 μm, q''_{eff} = 100 W/cm^2, Re = 100 15

2.3 1D and 3D temperature distribution of the substrate base, channel bottom wall, and bulk fluid temperature for copper substrate (k_s=401), H_w = 5000 μm, q''_{eff} = 100 W/cm^2, Re = 100 16

2.4 1D and 3D temperature distribution of the substrate base, channel bottom wall, and bulk fluid temperature for copper substrate (k_s=401), H_w = 5000 μm, q''_{eff} = 100 W/cm^2, Re = 1000 17

2.5 1D and 3D temperature distribution of the substrate base, channel bottom wall, and bulk fluid temperature for copper substrate (k_s=401), H_w = 5000 μm, q''_{eff} = 100 W/cm^2, Re = 100 18

2.6 1D and 3D temperature distribution of the substrate base, channel bottom wall, and bulk fluid temperature for silicon substrate (k_s=148), H_w = 50 μm, q''_{eff} = 100 W/cm^2, Re = 100 19

2.7 1D and 3D temperature distribution of the substrate base, channel bottom wall, and bulk fluid temperature for silicon substrate (k_s=148), H_w = 5000 μm, q''_{eff} = 100 W/cm^2, Re = 100 20

3.1 2D grid 28

3.2 1D, 2D, and 3D temperature distribution of the substrate base, channel bottom wall, and bulk fluid temperature for copper substrate (k_s=401), H_w = 50 μm, q''_{eff} = 100 W/cm^2, Re = 100 29

3.3 1D, 2D, and 3D temperature distribution of the substrate base, channel bottom wall, and bulk fluid temperature for copper substrate (k_s=401), H_w = 5000 μm, q''_{eff} = 100 W/cm^2, Re = 100 30

3.4 1D, 2D, and 3D temperature distribution of the substrate base, channel bottom wall, and bulk fluid temperature for copper substrate (k_s=401), H_w = 5000 μm, q''_{eff} = 100 W/cm^2, Re = 1000 31

3.5 1D, 2D, and 3D temperature distribution of the substrate base, channel bottom wall, and bulk fluid temperature for copper substrate (k_s=401), H_w = 5000 μm, q''_{eff} = 100 W/cm^2, Re = 100 32

3.6 1D, 2D, and 3D temperature distribution of the substrate base, channel bottom wall, and bulk fluid temperature for silicon substrate (k_s=148), H_w = 50 μm, q''_{eff} = 100 W/cm^2, Re = 100 33

3.7 1D, 2D, and 3D temperature distribution of the substrate base, channel bottom wall, and bulk fluid temperature for silicon substrate (k_s=148), H_w = 5000 μm, q''_{eff} = 100 W/cm^2, Re = 100 34

4.1 Flow regions. 40

4.2 Variations of limiting flow rates. 44

4.3 Variations of single-phase heat sink channel bottom temperature at the outlet and pressure drop. 46

4.4 Variations of two-phase heat sink channel bottom temperature at the outlet and pressure drop. 47
4.5 Single-phase performance map. 48
4.6 Two-phase performance map. 48
4.7 Single-phase performance map. 51
4.8 Single-phase performance map. 52
4.9 Two-phase performance map. 54
4.10 Two-phase performance map. 55
4.11 Design flow chart. 56

5.1 Example of the radar amplifier to be cooled 62
5.2 Test heater design. 63
5.3 Heat sink design solid model, top view. 64
5.4 Heat sink design solid model, bottom view. 65
5.5 Heat sink cover design solid model. 66
5.6 Heat sink assembly design solid model. 67
5.7 Single-phase micro-channel heat sink design region 68
5.8 Micro-channels, magnified 69
5.9 Single-phase heat sink 70
5.10 Single-phase heat sink cover 70
5.11 Test heater 72
5.12 Heat sink test section components 73
5.13 Heat sink assembly 74
5.14 Heater system 75
5.15 Schematic of a typical flow loop 77
5.16 Thermocouple inidcators 79
5.17 Thermocouples 80
5.18 Pressure measurement system 81

5.19 Data acquisition unit 82
5.20 LabVIEW program 83
5.21 Reservoir 85
5.22 Pump 85
5.23 Compact brazed heat exchangers 86
5.24 Rotameters 87
5.25 Pressure gauge 88
5.26 Refrigeration bath 88
5.27 Flow loop cart, internal 89
5.28 Flow loop cart panels 90
5.29 Flow loop cart 91
5.30 Test cart 92
5.31 Full heat sink testing system 93
5.32 Single-phase heat sink thermal performance results for 80 W with a coolant flow rate of 200 ml/min without accounting for the interface resistance. . . 96
5.33 Single-phase heat sink thermal performance results for 80 W with a coolant flow rate of 200 ml/min accounting for the interface resistance. 97
5.34 Single-phase heat sink thermal performance results for 100 W with a coolant flow rate of 200 ml/min accounting for the interface resistance. 98
5.35 Temperature variation with coolant flow rate. 99
5.36 Single-phase heat sink hydraulic performance for varying flow rates. 100

6.1 Variation of two-phase minimum flow rate and two-phase maximum flow rate with effective heat flux. 105
6.2 Variation of highest heat sink temperature and pressure drop for $W_{ch} = 100$ μm and $W_w = 100$ μm 106
6.3 Variation of highest heat sink temperature and pressure drop for $W_{ch} = 200$ μm and $W_w = 200$ μm 107

6.4 Variation of highest heat sink temperature and pressure drop for $W_{ch} = 300$ μm and $W_w = 300$ μm 108
6.5 Variation of highest heat sink temperature and pressure drop for $W_{ch} = 400$ μm and $W_w = 400$ μm 109
6.6 Best-fit equation for FC-72 saturated liquid density versus temperature from 20 °C to 80 °C. 111
6.7 Best-fit equation for FC-72 saturated vapor density versus temperature from 20 °C to 80 °C. 112
6.8 Best-fit equation for FC-72 saturated enthalpy versus temperature from 20 °C to 80 °C. 113
6.9 FC-72 saturated liquid viscosity data versus temperature. 114
6.10 Two-phase heat sink test section, drawings 117
6.11 Two-phase heat sink test section, solid model 118
6.12 Two-phase heat sink housing, solid model 119
6.13 Two-phase heat sink sample surface, drawings 120
6.14 Two-phase heat sink test section assembly, solid model 121
6.15 Pump with analog pump drive remote 123
6.16 FC-72 Reservoir 125
6.17 Instrumentation cart 126

Nomenclature

A_{eff} effective heated area of the heat sink chanel walls, m^2

Bo boiling number

C parameter in pressure drop relations

c_p specific heat at constant pressure, kJ/kg·°C

d_e heated equivalent diameter, m

ΔP pressure drop across heat sink, bar

ΔP_c contraction pressure loss, bar

ΔP_e expansion pressure recovery, bar

$\Delta P_{sp,dh}$ pressure drop in single-phase hydrodynamically developing region, bar

$\Delta P_{sp,fh}$ pressure drop in single-phase hydrodynamically fully-developed region, bar

ΔP_{tp} pressure drop in two-phase region, bar

$\Delta P_{tp,a}$ accelerational two-phase pressure drop, bar

$\Delta P_{tp,f}$ frictional two-phase pressure drop, par

Δl division of length of heat sink, m

d_h hydraulic diameter of micro-channel, m

E parameter in heat transfer relations

$f_{app,dh}$ apparent friction factor for single-phase hydrodynamically developing flow

f_f friction factor based on local liquid flow rate

$f_{sp,fh}$ friction factor in single-phase hydrodynamically fully-developed region

G mass velocity, $kg/m^2 \cdot s$

h_{fg} enthalpy of saturated liquid kJ/kg

H height of heat sink, m

h_{sp} single-phase convective heat transfer coefficient, $W/m^2 \cdot °C$

H_c cover plate thickness, m

H_{ch} height of micro-channel, m

H_w distance from micro-channel bottom wall to heat sink bottom wall, m

K_c contraction loss coefficient

k_f thermal conductivity of the liquid coolant, $W/m \cdot °C$

$K(\infty)$ entrance loss coefficient

k_s thermal conductivity of substrate, $W/m \cdot °C$

$L^+_{sp,dh}$ non-dimensional length of single-phase hydrodynamically developing region

L length of heat sink, m

$L_{sp,dh}$ length of single-phase hydrodynamcially developing region, m

$L_{sp,fh}$ length of single-phase hydrodynamcially fully-developed region, m

L^* non-dimensional length of heat sink

L_{tp} length of two-phase region

$\dot{m}$ mass flow rate, kg/s

m fin parameter, 1/m

N number of channels

Nu_3 Nusselt number for laminar fully-developed flow for three wall heat transfer

Nu_4 Nusselt number for laminar fully-developed flow for four wall heat transfer

P_{out} outlet pressure, bar

Pr_f Prandtl number

P_w total rate of heat supplied to heat sink, W

q''_{eff} Dissipative heat flux based on heat sink planform area, W/cm^2

q''_{max} critical heat flux (CHF) in heat sink, W/cm^2

q''_p mean heat flux over heated inside area of micro-channel

Q_t total volume flow rate, ml/min

$Q_{t,spmin}$ single-phase minimum volume flow rate, ml/min

$Q_{t,tpmax}$ two-phase maximum volume flow rate, ml/min

R_{cap} thermal resistance due to the coolant heat capacity, °C/W

R_{cond} thermal resistance due to the conduction through the substrate base, °C/W

Re_f Reynolds number based on local liquid flow rate

Re_{in} Reynolds number based on inlet liquid conditions

Re_{sp} Reynolds number based on properties at mean temperature in single-phase region

R_{fin} thermal resistance due to fin effects, °C/W

R_{hs} thermal resistance of the heat sink, °C/W

T_c coolant mean temperature, °C

$T_{c,out}$ coolant mean temperature at channel exit, °C

$T_{c,x}$ coolant mean temperature at location x, °C

T_{in} inlet temperature

T_{max} highest temperature in thermal design procedure ($T_{max} = T_{w,out}$), °C

T_s heat sink bottom wall temperature, °C

T_{sat} saturation temperature, °C

$T_{s,out}$ heat sink bottom wall temperature at channel exit, °C

$T_{s,x}$ heat sink bottom wall temperature at location x, °C

T_w micro-channel bottom wall temperature, °C

$T_{w,out}$ micro=channel bottom wall temperature at channel exit, °C

$T_{w,x}$ micro-channel bottom wall temperature at location x, °C

v_f specific volume, m^3/kg

W width of heat sink, m

W_{ch} width of micro-channel, m

We Weber number

W_w thickness of wall separating micro-channels, m

x_e thermodynamic equilibrium quality

$x_{e,out}$ thermodynamic equilibrium quality at channel outlet

X_{vv} Martinelli parameter for laminar liquid – laminar vapor flow

Greek Symbols

α_{out} void fraction at the channel outlet

β aspect ratio of micro-channel

η fin efficiency

μ_b viscosity evaluated at coolant mean temperature, N·s/m^2

μ_w viscosity evaluated at channel bottom wall temperature, N·s/m^2

ρ density kg/m^3

ρ_f liquid density kg/m^3

ρ_g vapor density kg/m^3

σ surface tension, N/m

Chapter 1

Introduction

1.1 Background

The past decades have witnessed a significant increase in the levels of waste heat that need to be dissipated from electronic systems and devices. This is due to the advancements in circuit integration and system miniaturization which have enabled the use of smaller components to produce smaller, faster, and better performing electronic systems. The increases in dissipative waste heat require more efficient electronic cooling techniques in order to maintain a reliable operation.

Liquid-cooled micro-channel heat sinks have emerged recently as a prime contender for thermal management of next generation high-power-density electronic devices. A heat sink is classified as a micro-channel heat sink by the characteristic dimensions of the liquid coolant flow passages. A micro-channel heat sink is comprised of flow channels whose characteristic dimensions range from 10 to 1000 micrometers. Key technical merits of micro-channel heat sinks include low thermal resistance, small coolant inventory requirement, small coolant flow rate requirement, and small heat sink mass and volume. Figure 1.1 illustrates the construction of a typical micro-channel heat sink. The heat sink base substrate is often fabricated from a high thermal conductivity solid material such as copper or silicon. A series of parallel rectangular micro-slots are machined into the substrate. Closed micro-channels are formed by using a cover plate and serve as flow passages for

liquid coolant. The cover plate is often fabricated from a low thermal conductivity material to ensure that the heat entering the heat sink is removed by the liquid coolant.

Depending on whether liquid coolant boils inside the micro-channels, micro-channel heat sinks can be classified as single-phase or two-phase. For a fixed heat input and relatively high coolant flow rate, the coolant may maintain its liquid single-phase state throughout micro-channels, which leads to a single-phase heat sink. When coolant flow rate is relatively low, the liquid coolant may reach its boiling point while still flowing in micro-channels and flow boiling occurs, which results in a two-phase heat sink. While single-phase heat sinks generally require less complicated flow delivery and control systems to operate, two-phase heat sinks offer additional advantages over their single-phase counterparts as a result of enhanced heat transfer associated with flow boiling, including much smaller coolant flow rate requirements, much higher convective heat transfer coefficients, and better stream-wise temperature uniformity.

Figure 1.1 shows the key geometrical parameters of a micro-channel heat sink, including heat sink length L, heat sink width W, heat sink height H, cover plate thickness H_c, micro-channel height H_{ch}, distance between channel bottom wall and heat sink bottom wall H_w, micro-channel height H_{ch}, micro-channel width W_{ch}, and wall thickness W_w between neighboring micro-channels. Figure 1.1 also shows a unit cell containing a single micro-channel and surrounding solid. Because of symmetry, the unit cell is often used to analyze the performance of the heat sink.

During operation, a micro-channel heat sink is attached to the top surface of the electronic device that needs to be cooled. The heat generated by the device is first transferred through the base substrate of the heat sink through heat conduction, and then carried away by the liquid coolant that flows through the micro-channels. In the present analysis, the heat generating electronic device is idealized as a constant heat flux boundary condition at the heat sink bottom wall. Figure 1.1 illustrates the heat flux distributions along the heat sink bottom wall as well as the micro-channel side walls and bottom wall.

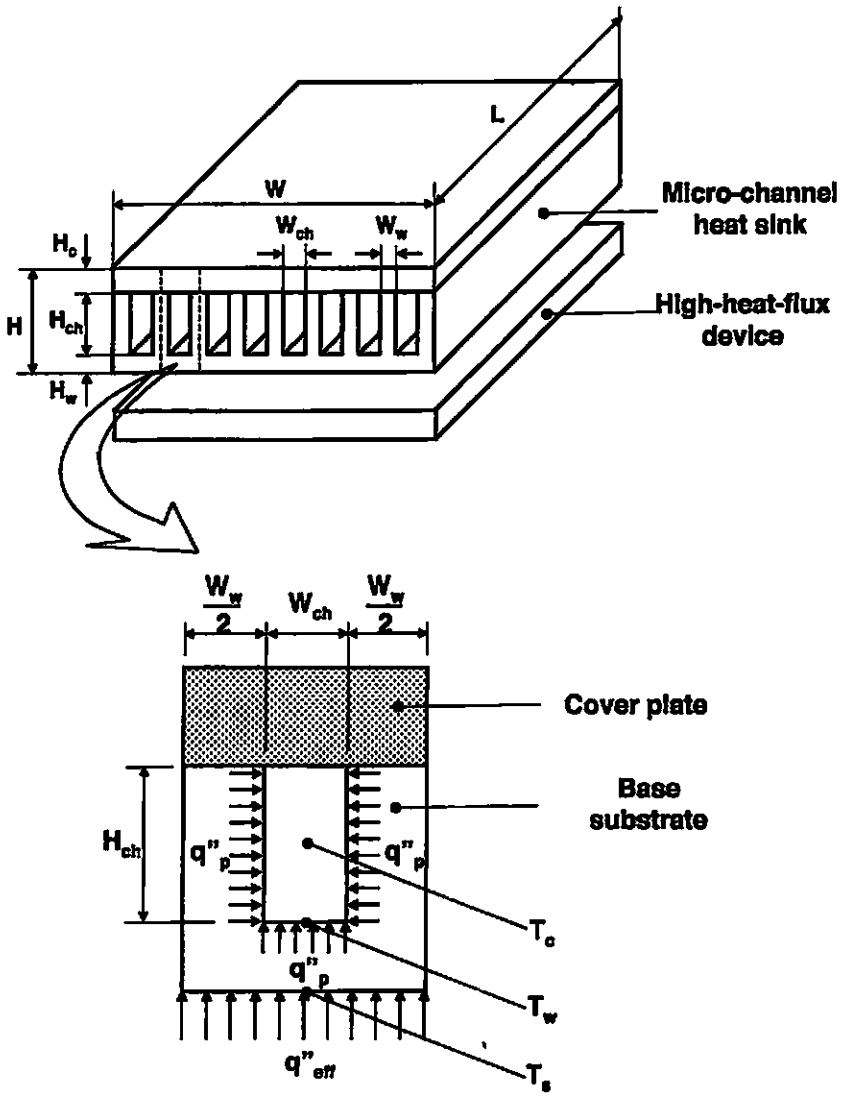

Figure 1.1: Construction of typical micro-channel heat sinks.

Temperature distribution inside a micro-channel heat sink under specified operating conditions is often used to describe the heat sink thermal performance. The most important temperatures within the heat sink are the temperature of heat sink bottom wall T_s, the temperature of micro-channel bottom wall T_w, and mean temperature of the coolant T_c. Figures 1.2 (a) and 1.2 (b) illustrate the profiles of the coolant mean temperature T_c, micro-channel bottom wall temperature T_w, and heat sink bottom wall temperature T_s along the stream-wise direction in single-phase and two-phase heat sinks, respectively. Single-phase micro-channel heat sinks rely on sensible heat exchange of the liquid coolant to remove heat, and coolant mean temperature T_c increases along the stream-wise direction. Two-phase micro-channel heat sinks, on the other hand, capitalize on the latent heat exchange. The maximum coolant temperature is set by the saturation temperature corresponding to local pressure.

Practical implementation of micro-channel heat sinks depends on the availability of (a) reliable predictive tools based on a fundamental understanding of the thermal/fluid transport processes in micro-channels, and (b) effective thermal design methodology. Due to its inherent technical advantages, single-phase micro-channel heat sink have been studied quite extensively ever since the concept was first proposed by Tuckerman and Pease [1]. Most published studies in the area of single-phase heat sink were focused on experimental investigation of micro-channel thermal/fluid transport phenomena and development of accurate predictive tools [2]–[7]. Excellent reviews on the subject have been provided by Garimella and Sobhan [28] and Morini [29]. Most recent studies showed that conventional macro-channel predictive tools are fairly accurate at predicting micro-channel pressure drop and heat transfer characteristics [6],[7]. Two-phase studies on flow boiling in micro-channels, on the other hand, revealed predictions of macro-channel models and correlations often showed appreciable deviation from experimental results, and several new predictive tools specifically tailored to micro-channel flow boiling were proposed [8]–[21]. A few studies on thermal design of single-phase [22]–[27], and two-phase micro-channel heat sinks [30] are also available. These studies optimized heat sink geometry by minimizing the overall thermal

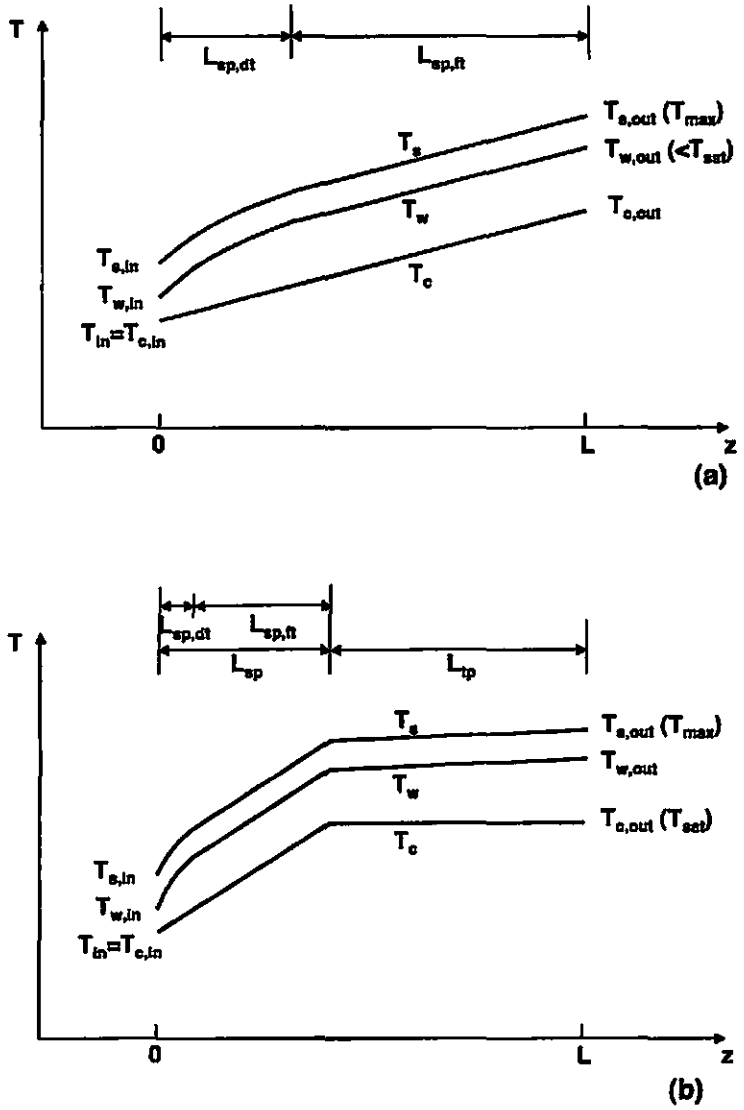

Figure 1.2: Temperature profile along stream-wise direction in (a) single-phase and (b) two-phase heat sinks.

resistance under the constraint of either constant pressure drop or constant pumping power. While rectangular micro-channels were used in these optimization studies due to ease of fabrication, Fisher and Torance proposed schemes to also optimize shape of micro-channels for single-phase heat sinks [31], [32].

1.2 Research Objectives

The focus of the present thesis work is on modeling, design, and testing of single-phase and two-phase micro-channel heat sinks for pratical electronic cooling applications. Chapter 2 describes one-dimensional (1D) modeling and three-dimensional (3D) numerical analysis of heat transfer process in single-phase micro-channel heat sinks. Results from the two methods are compared to evaluate the accuracy of the 1D model as a predictive tool for heat sink design. Chapter 3 proposes a new two-dimensional (2D) heat transfer model. The new 2D modeling method can be considered as a compromise of the aforementioned 1D and 3D approaches, and has the advantages of high accuracy and less computational time. Chapter 4 develops a systematic thermal design methodology for both single-phase and two-phase micro-channel heat sinks based on one-dimensional (1D) modeling. Chapter 5 presents design, fabrication, and testing of a water cooled single-phase micro-channel heat sink. Chapter 6 presents design of a FC-72 cooled two-phase micro-channel heat sink. Finally, chapter 7 summarizes the key results of this thesis work.

Chapter 2

One-Dimensional Modeling and Three-Dimensional Numerical Analysis of Single-Phase Heat Sinks

Two approaches are often used to describe the heat transfer process in single-phase heat sinks: one-dimensional (1D) modeling and three-dimensional (3D) numerical analysis. One-dimensional modeling is the simplest way to describe the heat transfer process in micro-channel heat sinks, and has been widely used as predictive tools in micro-channel heat sink design. The approach is less accurate because of several major assumptions it adopts. Three-dimensional analysis can provide a more accurate description of the heat transfer process. But it is more computation-intensive. Incorporation of the approach into a heat sink design scheme can be difficult. In this chapter, both methods are used to predict the temperature distribution in single-phase heat sinks, and results are compared.

2.1 One-Dimensional Modeling

2.1.1 Major Assumptions

The major assumptions that are used in the 1D modeling include:

1. the solid wall separating two flow channels is approximated as a thin fin,

2. heat transfer at each heat sink cross-section is one-dimensional,

3. fluid temperature changes only along the flow direction and is uniform at each channel cross-section,

4. the convective heat transfer coefficient along the micro-channel wall is constant and known,

5. steady heat transfer,

6. laminar flow,

7. constant solid properties

2.1.2 Temperature Distribution

The key temperatures within the heat sink, the temperature of the heat sink bottom (substrate base) T_s, the temperature of the channel bottom wall T_w, and the mean temperature of the coolant T_c, can be calculated by using the thermal resistance of the micro-channel heat sink. The mean coolant temperature T_c can be calculated by finding the thermal resistance due to the heat capacity of the liquid coolant.

$$R_{cap} = \frac{1}{\dot{m} c_p} \tag{2.1}$$

$$T_{c,x} = T_{c,x-1} + q''_{eff} W \Delta l R_{cap} \tag{2.2}$$

The temperature of the heat sink channel bottom wall T_w can be calculated by finding the thermal resistance due to the fin effects.

$$R_{fin} = \frac{1}{h_{sp} A_{eff}} \tag{2.3}$$

where,

$$A_{eff} = N(W_{ch}\Delta l + 2\eta H_{ch}\Delta l), \tag{2.4}$$

$$N = \frac{W}{W_{ch} + W_w}, \tag{2.5}$$

$$\eta = \frac{tanh(mH_{ch})}{mH_{ch}}, \tag{2.6}$$

$$m = \sqrt{\frac{2h_{sp}}{k_s W_w}} \tag{2.7}$$

$$T_{w,x} = T_{c,x} + q''_{eff} W \Delta l R_{fin} \tag{2.8}$$

and h_{sp}, is calculated by A.1.

Finally the temperature of the heat sink bottom wall T_s can be calculated using the thermal resistance due to heat conduction through the heat sink base substrate.

$$R_{cond} = \frac{H_w}{k_s W \Delta l} \tag{2.9}$$

$$T_{s,x} = T_{w,x} + q''_{eff} W \Delta l R_{cond} \tag{2.10}$$

Typically the thermal resistance of the heat sink is calculated at the exit of the of the channels where the values will be the greatest and will encompass the entire length of the heat sink.

$$R_{hs} = R_{cap} + R_{fin} + R_{cond} \tag{2.11}$$

where, Δl = L in the previously defined resistances.

2.1.3 Determination of Nusselt Number

A new correlation is developed to evaluate the Nusselt number that is used to calculate the single phase heat transfer coefficient, h_{sp}.

$$Nu = Nu_4 + 8.68\left(10^3 L^*\right)^{-0.506} \exp[(9.9776\ln(\beta) - 26.379)L^*] \tag{2.12}$$

A curve fit from the data from Wibulswas [33] in Shah & London [34] was done to produce this correlation. This correlation was developed to allow for a continuous calculation of the Nusselt number between the thermally developing and the fully developed regions. As the non-dimensional length of the heat sink, L^*, increases the term on the right hand side goes to zero giving the Nusselt number for the fully developed value. The present correlation is compared to work by Lee & Garimella [35], Perkins et al. [36], and also data from Chandrupalta [37], and Wibulswas [33] as shown in Figure 2.1. The main advantage over the correlation purposed by Lee & Garimella is that the present correlation is continuous, where as the previous has two distinct regions, thermally developing and thermally fully

developed, which are disconnected. The present correlation shows a good fit throughout the entire field.

2.1.4 Calculation Procedure

The distribution of the mean coolant temperature, the heat sink substrate bottom temperature, and the channel bottom wall temperature can be calculated by using the thermal resistance equations developed in the previous section. Once the heat sink geometry and other operating parameters are provided, the length of the heat sink can be divided into a large number of small segment to conduct the calculations. Calculations proceed from micro-channel upstream to downstream.

2.2 Three-Dimensional Numerical Analysis

A three-dimensional fluid flow and heat transfer numerical analysis was done by Dr. Qu using a finite difference FORTRAN program, as used in [38]. In this analysis the conjugate heat transfer problem, combing heat conduction in the solid and convective heat transfer to the coolant, is solved by solving governing differential equations numerically in both liquid and solid regions. The temperature and heat flux are continuous at the liquid-solid boundary interface. The major assumptions of the 3D analysis are:

1. steady fluid flow and heat transfer,
2. incompressible fluid,
3. laminar flow,
4. constant solid properties,
5. negligible radiation heat transfer,
6. negligible superimposed natural convective heat transfer.

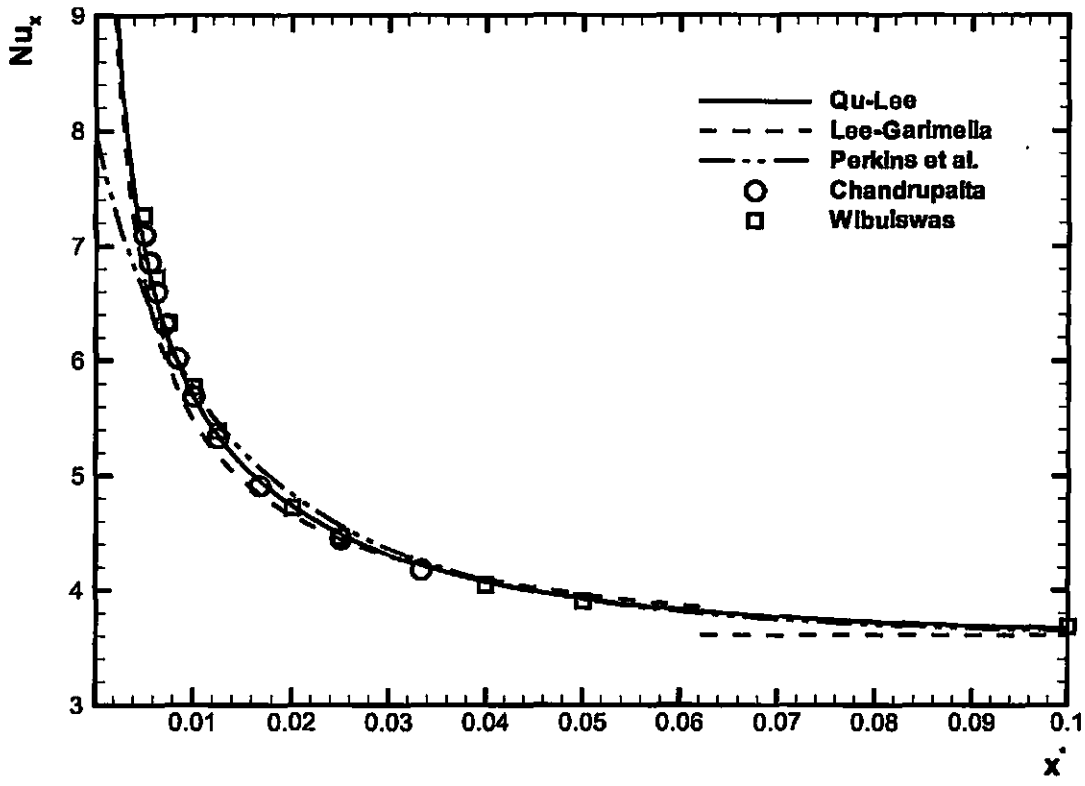

Figure 2.1: Comparison of Nusselt numbers for square ducts/channels with four heated sides obtained from a revised curve fit from [34] by Qu & Lee, correlations from Lee & Garimella[35] and Perkins et al. [36] also with data from Chandrupalta [37] and Wibulswas [33]

The thee-dimensional finite difference problem is solved using the SIMPLE algorithm [39]. The computational domain is the unit cell.

2.3 Results and Discussion

The 1-D modeling provides a simplified means to evaluate the global heat transfer characteristics and is widely used in the design of micro-channel heat sink geometry. However, it should be noted that a number of major assumptions are employed. Some of them may deviate significantly from the real situation, which may reduce the accuracy of the 1-D model. In particular, the axial heat conduction in heat sink solid substrate may lead to a redistribution of heat flux inside the heat sink, and the one-dimensional heat transfer approximation may no longer hold. A more accurate description of the heat transfer characteristics within the heat sink can be obtained by direct 3D numerical analysis of heat transfer in both the solid and liquid coolant.

A sample heat sink with geometrical parameters shown in Table 2.1 is used as the basis for calculating the temperature distributions along the flow direction for the substrate base, channel bottom wall, and bulk fluid temperature using both 1D modeling and 3D analysis. Results from the two methods are compared to each other to evaluate the accuracy of the 1D model as well as the effects of axial heat conduction. Other parameters that are needed in the calculation are provided in Table 2.2

Table 2.1: Heat sink geometrical parameters

W (cm)	L (cm)	H_{ch} (μm)	W_{ch} (μm)	W_w (μm)
1	1	150	50	50

2.3.1 Effect of Substrate Thickness, H_w

For a thin substrate thickness, 50 μm, the 1D and 3D temperature distributions match well for the majority of the length as can be seen in Figure 2.2 which means that the effect of

axial conduction is weak. The places where the temperatures differed were near the inlet and exit, which may be due to inlet and exit effects which were not considered in the 1D model. The temperature difference in those regions were not very significant.

As the substrate thickness is increased, however, the 1D and 3D results diverge as the axial conduction becomes more important as can be seen in Figure 2.3. For this case the temperature distributions for the 1D and 3D cases do not follow the same trend, showing that the heat has been conducted from the heat sink downstream to the upstream as the downstream has a lower temperature and the upstream has a higher temperature for the 3D case than for the 1D case. The results show the accuracy of the 1D modeling decreases with increasing heat sink base substrate thickness.

2.3.2 Effect of Reynolds Number, Re

As the reynolds number of the fluid increases, the temperature distribution of the fluid in the 1D and 3D cases match. The temperature distribution for the substrate and channel bottom wall temperature shows a slight reduction in the axial conduction, although there still seems to be a redistribution of the temperature at the substrate base. The results show the accuracy of the 1D modeling increases with increasing flow Reynolds number.

2.3.3 Effect of Heat Flux, q''_{eff}

As the heat flux is decreased all the temperatures decrease, however, qualitatively the trends remain the same. The results show the accuracy of the 1D modeling is not affected by the input heat flux.

2.3.4 Effect of Substrate Material, k_s

By changing the substrate material to silicon the thermal conductivity decreased. The effects of the axial conduction decreases. The results show the accuracy of the 1D modeling increases with decreasing solid substrate thermal conductivity.

Table 2.2: Key properties

Case	*Figure*	*Material – (Thermal Conductivity)* (W/m K)	H_w (μm)	*Heat Flux* (W/cm^2)	*Re*
1	2.2, 3.2	Copper – (401)	50	100	100
2	2.3, 3.3	Copper – (401)	5000	100	100
3	2.4, 3.4	Copper – (401)	5000	100	1000
4	2.5, 3.5	Copper – (401)	5000	10	100
5	2.6, 3.6	Silicon – (148)	50	100	100
6	2.7, 3.7	Silicon – (148)	5000	100	100

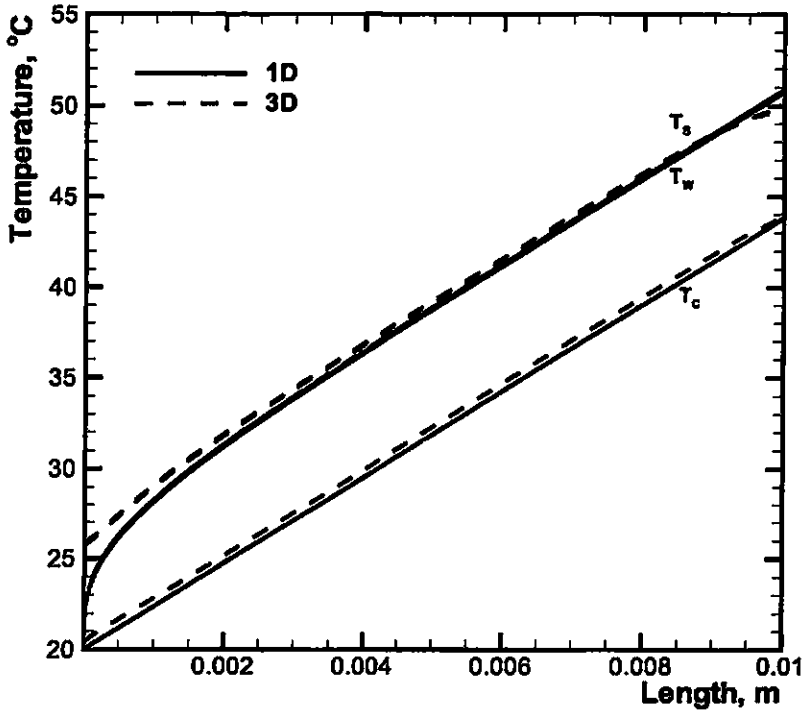

Figure 2.2: 1D and 3D temperature distribution of the substrate base, channel bottom wall, and bulk fluid temperature for copper substrate (k_s=401), H_w = 50 μm, q''_{eff} = 100 W/cm^2, Re = 100

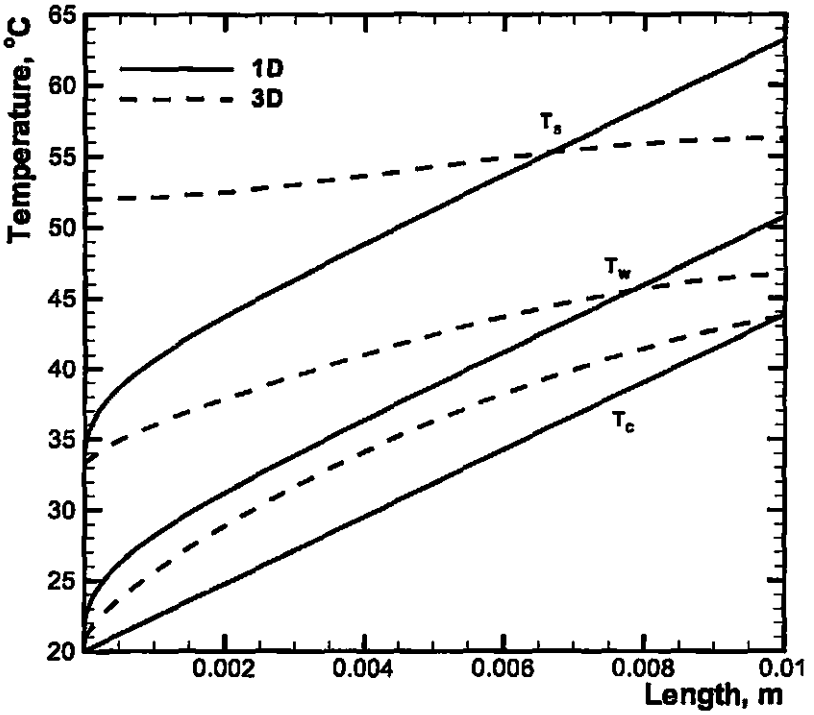

Figure 2.3: 1D and 3D temperature distribution of the substrate base, channel bottom wall, and bulk fluid temperature for copper substrate (k_s=401), $H_w = 5000$ μm, $q''_{eff} = 100$ W/cm^2, Re = 100

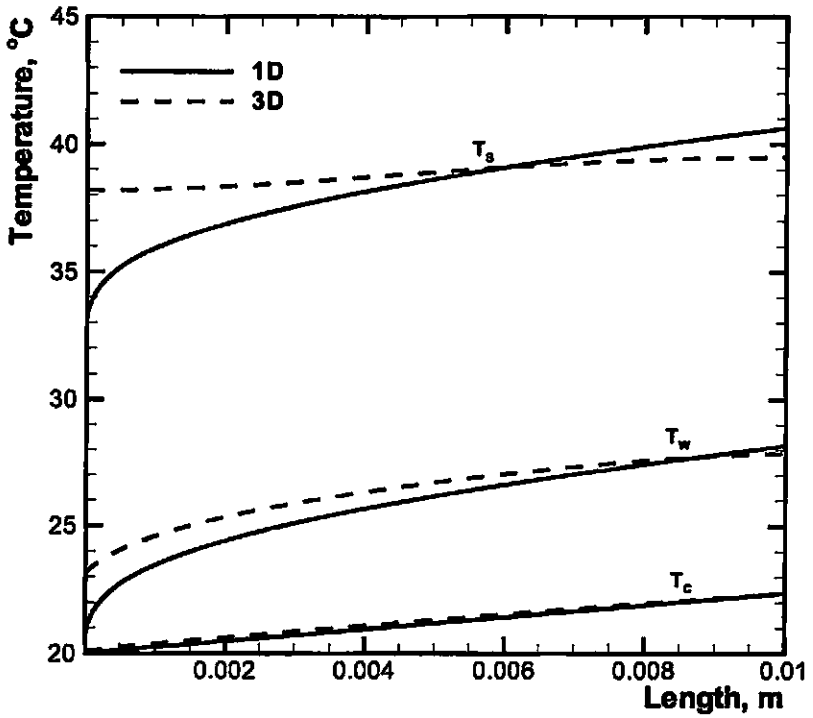

Figure 2.4: 1Dand 3D temperature distribution of the substrate base, channel bottom wall, and bulk fluid temperature for copper substrate (k_s=401), H_w = 5000 μm, q''_{eff} = 100 W/cm^2, Re = 1000

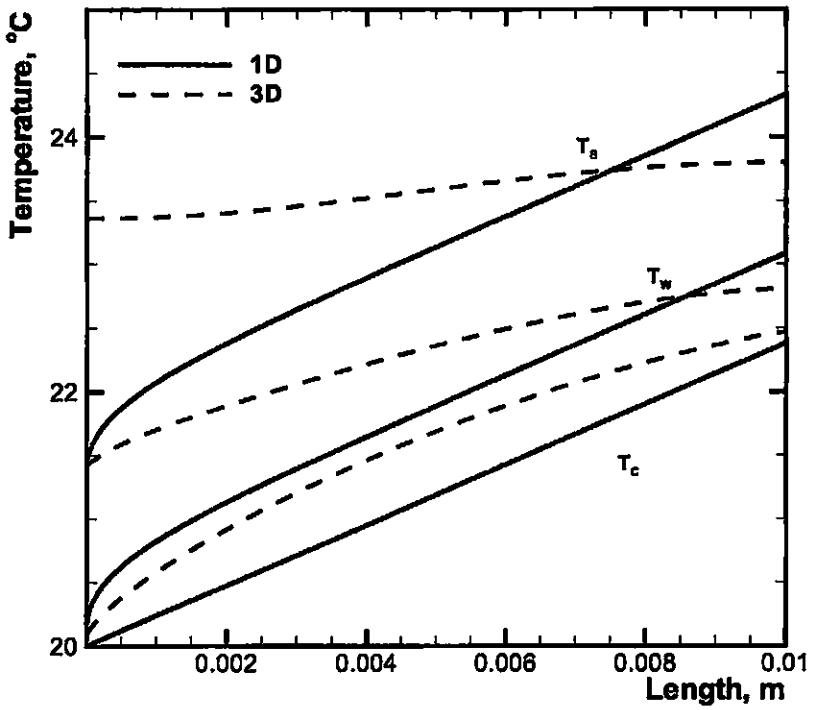

Figure 2.5: 1D and 3D temperature distribution of the substrate base, channel bottom wall, and bulk fluid temperature for copper substrate (k_s=401), H_w = 5000 μm, q''_{eff} = 10 W/cm^2, Re = 100

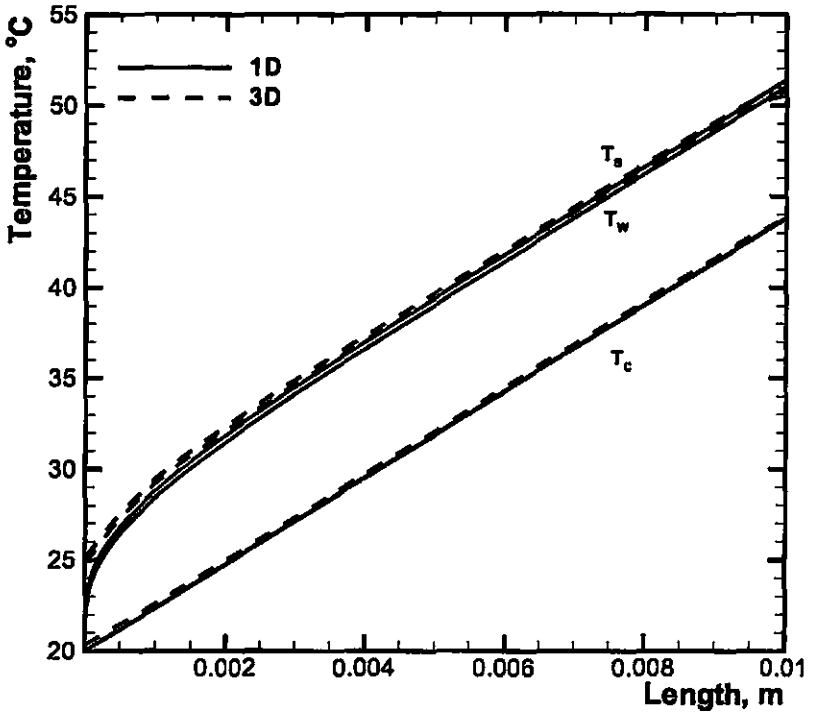

Figure 2.6: 1D and 3D temperature distribution of the substrate base, channel bottom wall, and bulk fluid temperature for silicon substrate (k_s=148), $H_w = 50$ μm, $q''_{eff} = 100$ W/cm^2, Re = 100

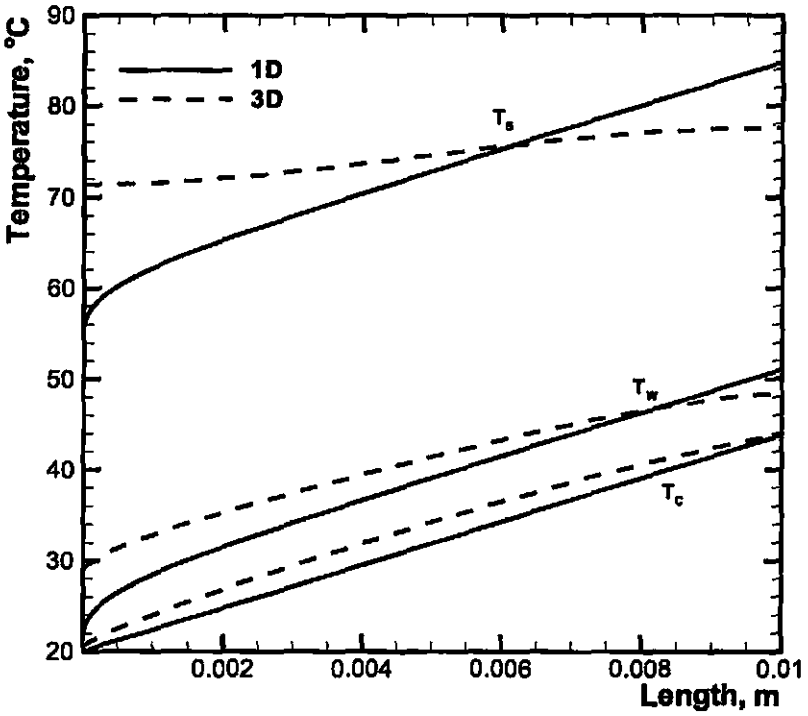

Figure 2.7: 1D and 3D temperature distribution of the substrate base, channel bottom wall, and bulk fluid temperature for silicon substrate (k_s=148), H_w = 5000 μm, q''_{eff} = 100 W/cm^2, Re = 100

2.4 Summary

A one-dimensional approach can be useful to estimate the conduction through the substrate base when it is thin, however, as the substrate thickness increases the effectiveness decreases. As shown with figures 2.2–2.7 the 1D and 3D results can differ significantly below the entrance and exit of the flow channels where the heat has conducted from the exit back to the entrance. The next chapter will introduce a 2D model which can incorporate this "axial" conduction. By adding this component to the analysis an improvement in the results from the 1D model will be seen.

Chapter 3

New Two-Dimensional Modeling of Single-Phase Heat Sinks

As discussed in the previous chapter, the advantage of the 1D model is its simplicity. The important temperature profiles in the micro-channel heat sink can be calculated in a very short period of time. Unfortunately, because of the 1D assumption, the axial heat conduction is not taken into account making it less accurate under certain conditions. The advantage of the 3D analysis is its ability to provide a more accurate temperature distribution in the heat sink. The disadvantage, however, is the amount of computational time it takes to perform the analysis. A new two-dimensional (2D) model is developed in the present thesis work which accounts for the axial heat conduction effect. The 2D model has an high accuracy when compared with 3D analysis, but requires far less computational time.

3.1 2-D Numerical Model

A two-dimensional finite volume code was written in FOTRAN 77 to solve the 2D conduction problem within the substrate base and to calculate the mean coolant temperature based on the heat flux distribution resulting from the temperature field in the solid base substrate.

In the two dimensional model the heat flux is assumed to be constant and uniform only at the base of the heat sink. A redistribution of heat flux may occur within the substrate

such that the heat flux at the top surface (corresponding to the micro-channel bottom wall) varies along the length of the heat sink.

3.1.1 Objective

The objective of the 2D code is to find the temperature field inside of a micro-channel heat sink base substrate. The key locations of temperatures are the base of the substrate that would interface with a high heat flux device, the bottom of the channel walls, and the bulk fluid temperature. Solving the problem while allowing axial heat conduction will improve the results from the 1D model and will need less computational time than a full 3D model and therefore the 2D analysis will be a compromise of the two.

3.1.2 Model Setup

The two-dimensional problem is solved using the same heat sink geometry as the given in Table 2.1. A rectangular area represents the heat sink substrate and is used as the computational domain. The area is broken down into smaller rectangular areas or "control volumes" by selecting the number of control volumes in both the x and y direction (length and height, respectively). The arrangement of these smaller areas form the grid. Once the number of control volumes are selected the nodes are then placed at the center of each control volume and at the center of each face along the boundaries. The sum of the heat conduction out of each control volume is equal to zero (3.4).

Keeping the idea of thermal resistances, the mean temperature in the coolant can be calculated in the same way as done previously with the one dimensional model with Equation 2.2. The heat flux that is used to calculate those temperatures will be the heat flux at the top surface (representing the channel bottom wall), equivalent to the heat conduction at the surface. The effective heat transfer coefficient that is used will account for the difference in geometry.

$$h_{eff} = h_{sp}\frac{W_{ch} + 2\eta H_{ch}}{W_{ch} + W_w} \tag{3.1}$$

Governing Equations

The basic equation that is solved within the computational domain is,

$$\int_v \nabla \cdot (k_s \nabla T) dv = 0 \tag{3.2}$$

using the Gauss Divergence Theorm then becomes,

$$\int_{\partial v} k_s \nabla T \cdot \vec{n} ds = 0 \tag{3.3}$$

which then can be expanded to,

$$\int_n k_{s,n} \frac{\partial T}{\partial y} dx - \int_w k_{s,w} \frac{\partial T}{\partial x} dy + \int_e k_{s,e} \frac{\partial T}{\partial x} dy - \int_s k_{s,s} \frac{\partial T}{\partial y} dx = 0 \tag{3.4}$$

and can be approximated and rearranged to ultimately get what is used,

$$\left(\frac{k_n \Delta x}{\delta y_n}\right) T_N + \left(\frac{k_w \Delta y}{\delta x_w}\right) T_W - \left(\frac{k_n \Delta x}{\delta y_n} + \frac{k_w \Delta y}{\delta x_w} + \frac{k_e \Delta y}{\delta x_e} + \frac{k_s \Delta x}{\delta y_s}\right) T_P + \left(\frac{k_e \Delta y}{\delta x_e}\right) T_E + \left(\frac{k_s \Delta x}{\delta y_s}\right) T_S = 0 \tag{3.5}$$

For the internal points a first order approximation for the derivative is used.

Boundary Conditions

At the boundaries a second order approximation of the derivative is used, which required three points instead of two.

The inlet and exit faces (west and east) of the domain are insulated,

$$\frac{dT}{dx}|_w = \frac{dT}{dx}|_e = 0 \tag{3.6}$$

The heat sink substrate bottom (south face) the conduction at the bottom is equal to the heat flux,

$$-k_s \frac{dT}{dy}|_{y=0} = q'' \tag{3.7}$$

At the heat sink channel bottom (north face) the conduction at the interface is equal to the convection. Where h_{eff} is given by 3.1

$$-k_s \frac{dT}{dy}|_{y=H_w} = h(effT - T_c) \tag{3.8}$$

3.1.3 Grid

The length and height of the substrate were each divided into two sub-regions, where a non uniform grid was used so that the number of control volumes was greater close to the boundaries where the gradients were expected to be larger.

Grid convergence

The grid was tested for convergence for both number of control volumes and for expansion coefficient (effectively control volume spacing) in the horizontal and vertical direction for a substrate thickness of 5000 μm.

The number of control volumes in the horizontal direction was tested from 10 - 120 control volumes in eight runs while keeping the number of control volumes in the vertical direction fixed at 80 and an expansion coefficient of 1.05 and 0.9524. The results were compared with the other runs and with the results from the 3D model. The temperature distributions converge when the number of control volumes is about 80.

Similarly, the temperature distributions converge when the number of control volumes in the vertical direction is about 40.

For the expansion coefficient there appeared to be little change when the number of control volumes was adequately large and so the initial value of 1.05 and 0.9524 was kept.

When the number of control volumes was small, 10 in the horizontal direction, a small coefficient with a more even distribution was favored.

3.1.4 Solution Technique

The bulk temperature of the coolant is initially calculated assuming that the heat flux at the interface between the channel wall and the fluid is uniform. Using the conservation of energy the outlet temperature of the fluid can be calculated.

Next the temperature field within the substrate is calculated. An alternating line by line tri-diagonal matrix algorithm was used to solve the temperature field within the micro-channel substrate. Four sweeps, one in each direction, was used in the TDMA per iteration. The order of the sweeps were from bottom to top, top to bottom, right to left, and then left to right. A subroutine for an ALBL TDMA from Peric [40] was modified and incorporated into the program.

Once the temperature field in the substrate is calculated the heat flux at the wall can be calculated. Using this temperature distribution a new bulk coolant temperature can be calculated.

This process is then repeated until the bulk fluid temperature distribution converges.

3.2 Results and Discussion

Figures 3.2 – 3.7 show the results of the 1D, 3D, and 2D analyses compared together. The 2D results show a very good agreement with the 3D results, within 1 degree, showing that a 2D approximation can be used in place of the 3D analysis for quicker results that are still reasonably accurate. Further differences are most likely due to not solving the fluid problem and entrance effects that cannot be captured with this approach.

3.3 Summary

Figures 3.2–3.7 show that the 2D model results and 3D model results match very well and differ by a maximum of one degree whereas the 1D and 3D results have differed by almost 10 degrees maximum. This shows that the axial conduction is a key component in the heat transfer within a micro-channel heat sink. The difference between the 2D and 3D models are mainly in the entrance region of the heat sink. A difference can mostly likely be attributed to either fluid effects which were not captured with this method as the fluid problem was not solved or to other effects which may appear in the transverse direction. The improvement in the results from the 1D to the 2D model is significant enough to use the 2D analysis and also the differences between the 2D and 3D models show that a 2D analysis would be sufficient in most cases. The use of the 2D model over the 3D model will decrease the amount computational time significantly while capturing the key heat transfer aspects. The 2D analysis will be used later in chapter 5 to verify experimental results.

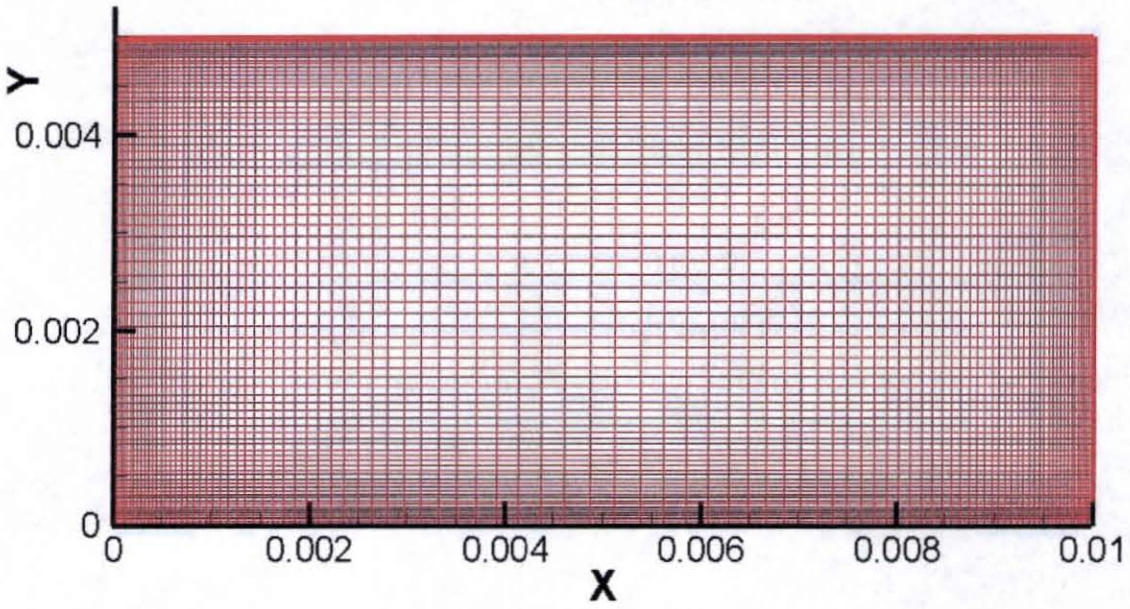

Figure 3.1: Grid

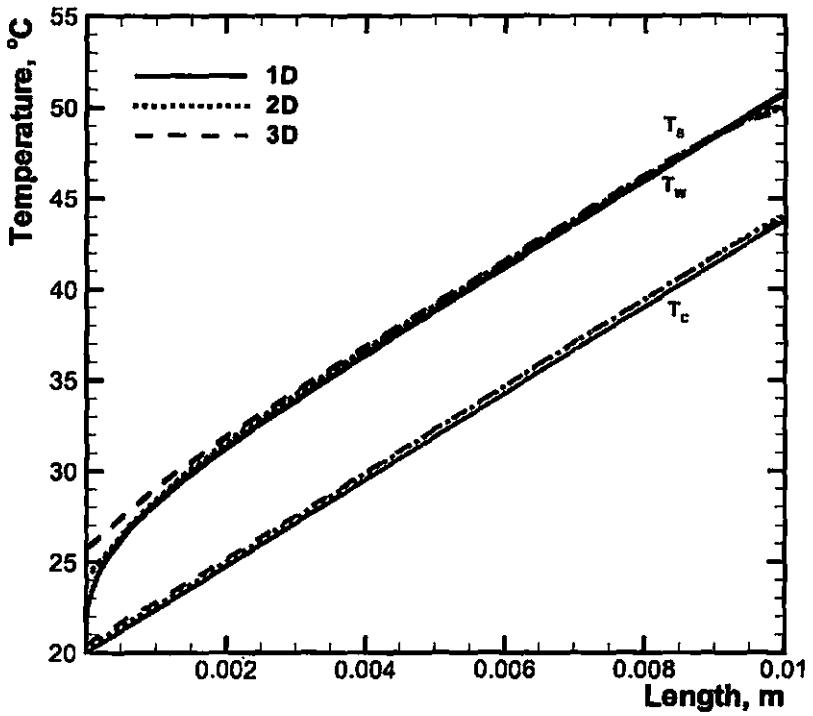

Figure 3.2: 1D, 2D, and 3D temperature distribution of the substrate base, channel bottom wall, and bulk fluid temperature for copper substrate (k_s=401), H_w = 50 μm, q''_{eff} = 100 W/cm^2, Re = 100

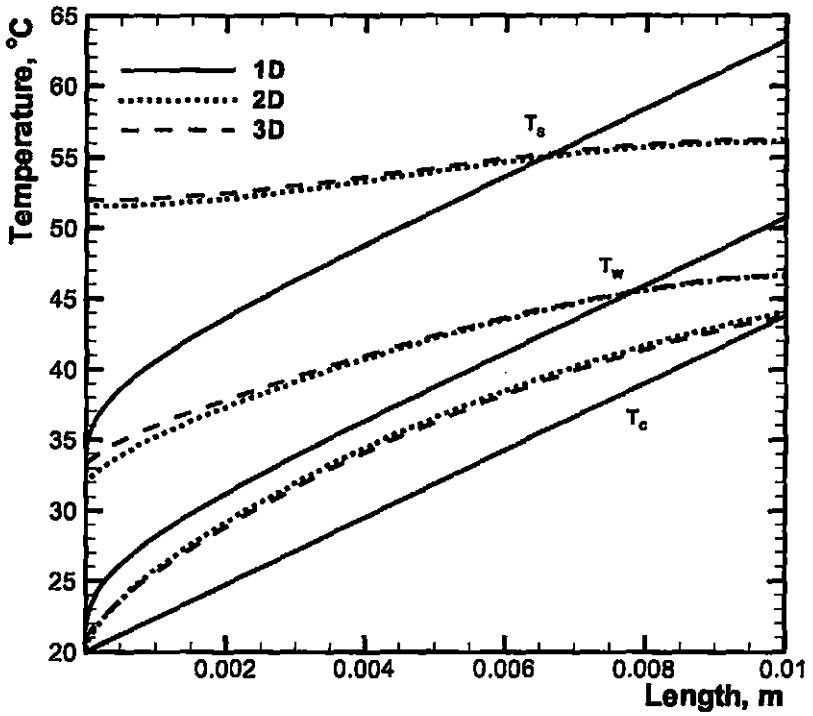

Figure 3.3: 1D, 2D, and 3D temperature distribution of the substrate base, channel bottom wall, and bulk fluid temperature for copper substrate (k_s=401), $H_w = 5000$ μm, $q''_{eff} = 100$ W/cm^2, Re = 100

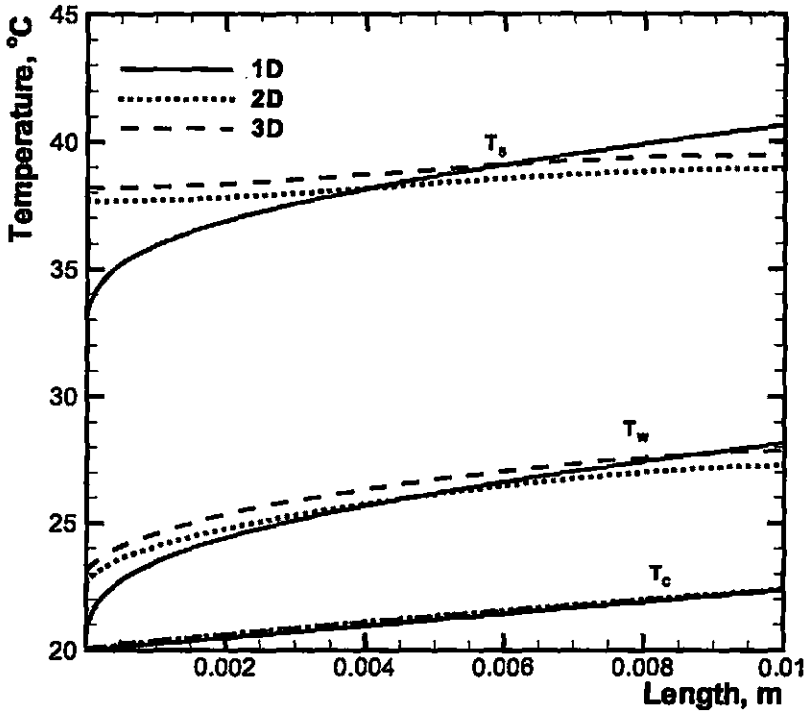

Figure 3.4: 1D, 2D, and 3D temperature distribution of the substrate base, channel bottom wall, and bulk fluid temperature for copper substrate (k_s=401), $H_w = 5000$ μm, $q''_{eff} = 100$ W/cm^2, Re = 1000

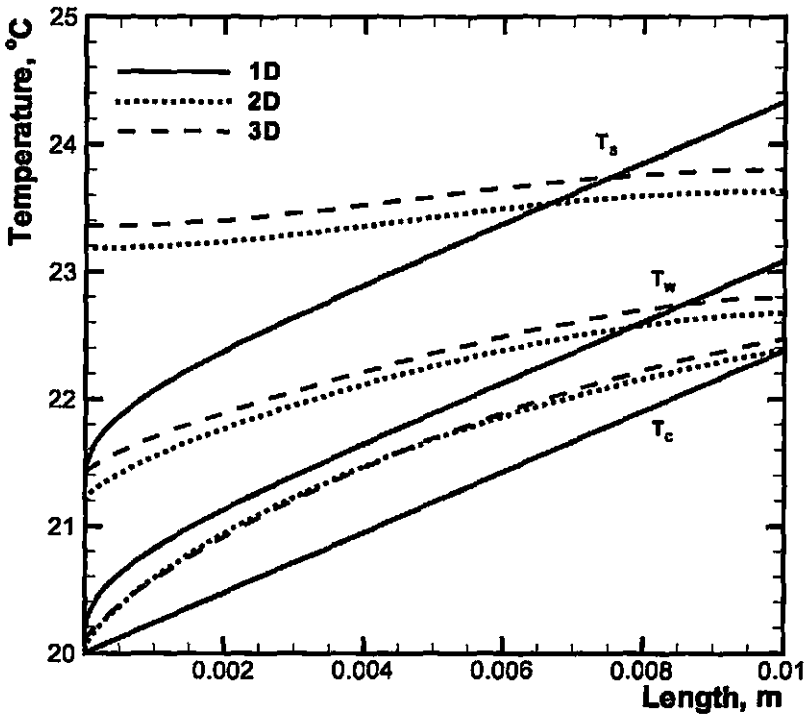

Figure 3.5: 1D, 2D, and 3D temperature distribution of the substrate base, channel bottom wall, and bulk fluid temperature for copper substrate (k_s=401), H_w = 5000 μm, q''_{eff} = 10 W/cm^2, Re = 100

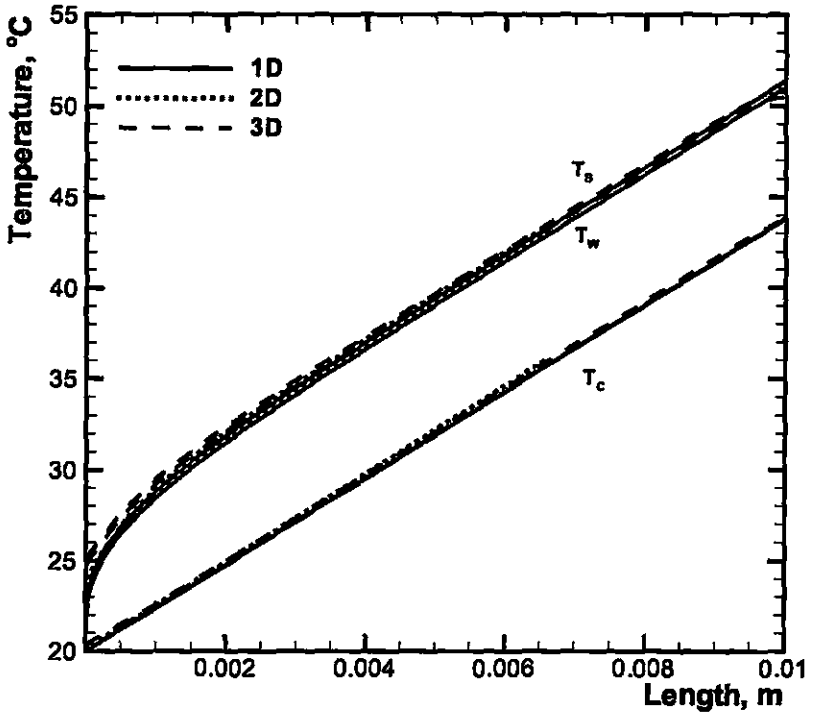

Figure 3.6: 1D, 2D, and 3D temperature distribution of the substrate base, channel bottom wall, and bulk fluid temperature for silicon substrate (k_s=148), H_w = 50 μm, q''_{eff} = 100 W/cm^2, Re = 100

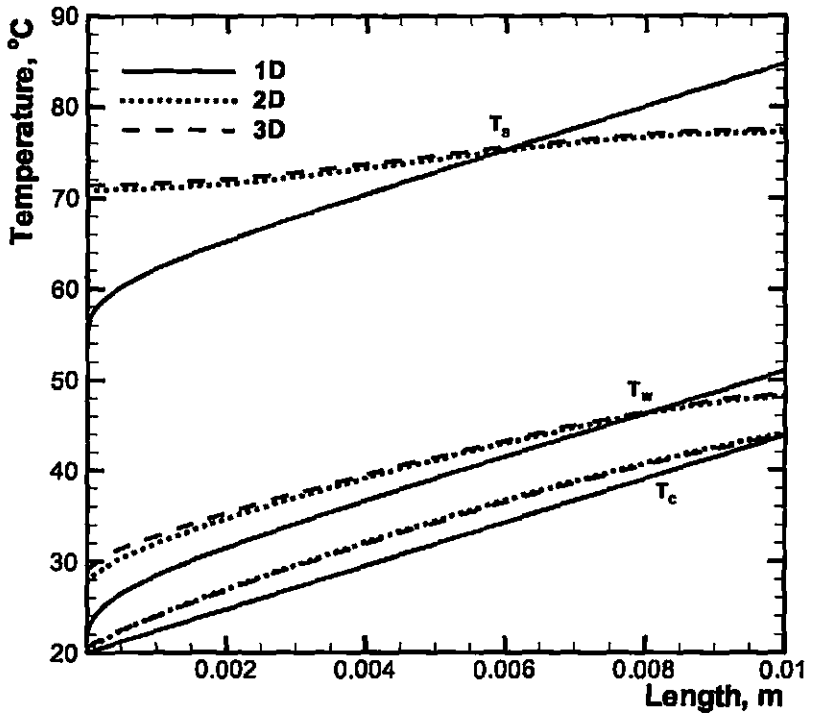

Figure 3.7: 1D, 2D, and 3D temperature distribution of the substrate base, channel bottom wall, and bulk fluid temperature for silicon substrate (k_s=148), H_w = 5000 μm, q''_{eff} = 100 W/cm^2, Re = 100

Chapter 4

Thermal Design of Single-Phase and Two-Phase Heat Sinks Using One-Dimensional Model

This chapter develops a systematic thermal design methodology for both single-phase and two-phase micro-channel heat sinks. The proposed thermal design methodology will determine micro-channel dimensions leading to the most desirable heat sink performance corresponding to a given dissipative heat flux and liquid coolant flow rate. An acceptable design region is first identified which encompasses all possible micro-channel dimensions corresponding to the prescribed dissipative heat flux and liquid coolant flow rate. Heat sink performance maps are then constructed within the acceptable design region. Finally, micro-channel dimensions yielding most desirable heat sink performance can be selected using the performance maps. The work constitutes a first step towards a comprehensive thermal design scheme that accommodates all possible flow regimes (two-phase, single-phase laminar, single-phase transition, single-phase turbulent) and design constraints (constant flow rate, constant pressure drop, constant pumping power).

4.1 Heat Sink Parameters

Parameters important to heat sink thermal design can be grouped into (1) geometrical parameters, (2) operating parameters, and (3) thermal/fluid parameters.

4.1.1 Geometrical Parameters

Geometrical parameters include both heat sink and micro-channel dimensions as illustrated in Fig. 1.1. Figure 1.1 also shows a unit cell containing a single micro-channel and surrounding solid. Because of symmetry, the unit cell can be used to analyze performance of the heat sink.

Heat sink dimensions are length L, width W, and height H. L and W are often set equal to those of the high-heat-flux device to which the heat sink is attached, and specified beforehand. H is the sum of cover plate thickness H_c, channel height H_{ch}, and distance between channel bottom wall and heat sink bottom wall H_w. The cover plate is often made from a low thermal conductivity material such as glass or high-temperature plastic and serves as a thermal insulation layer. When the cover plate is made of a high thermal conductivity material then all four walls of the channels will transfer heat. However, the average heat flux and Nusselt numbers from the side walls of a channel is found to be approximately 2 times greater than that of the top and bottom walls [38]. The effect of a high aspect ratio channel would result in a contribution of less than 5 percent for an aspect ratio of 5. Therefore, H_c does not affect the overall heat sink performance. H_w, is proportional to the thermal conduction resistance of the base substrate, and should be made as small as possible. In practice, there is always a practical minimum value for Hw that is set by machining and/or structural limitations. Both H_c, and H_w, are excluded from the present thermal design methodology.

Micro-channel dimensions are channel height H_{ch}, width W_{ch}, and wall thickness W_w between neighboring channels. Channel height H_{ch} was usually specified beforehand and not treated as a primary geometrical parameter for micro-channel heat sink design in several early studies [22]–[26]. The effect of H_{ch} on the thermal performance of single-phase as well as two-phase micro-channel heat sinks has been recently examined by Li and Peterson [27] and Qu and Mudawar [30], respectively. Using a three-dimension conjugate heat transfer model, Li and Peterson found that deeper micro-channels yielded better heat sink performance and therefore channels should be made as deep as possible [27]. The same

tendency was observed by Qu and Mudawar for two-phase micro-channel heat sinks[30]. H_{ch} should therefore be made as large as possible, and can also be specified beforehand. Again, there is always a practical maximum value for H_{ch} that is set by machining and/or structural limitations. The ultimate objective of the present thermal design methodology is to select values for W_{ch} and W_w that yield the most desirable heat sink performance.

4.1.2 Operating Parameters

Operating parameters represent conditions under which the heat sink is to operate. Common operating parameters include heat sink base substrate material, type of coolant, inlet temperature T_{in}, outlet pressure P_{out}, total coolant volume flow rate Q_t, and dissipative heat flux q''_{eff}. q''_{eff} is defined based on the heat sink's planform area, $q''_{eff} = \frac{P_w}{WL}$. Values of operating parameters are often specified beforehand.

4.1.3 Thermal/Fluid Parameters

Thermal/fluid parameters include highest heat sink temperature T_{max} and pressure drop ΔP, which indicate the heat sink performance, as well as single-phase minimum flow rate $Q_{t,spmin}$, two-phase maximum flow rate $Q_{t,tpmax}$, and two-phase minimum flow rate $Q_{t,tpmin}$, which set limits on Q_t to ensure that heat sinks operate in the designated flow regimes for a given q''_{eff}.

Highest temperature T_{max}

The highest temperature in a micro-channel heat sink T_{max} is one of the most important parameters to indicate the heat sink's thermal performance.

Figures 1.2 (a) and 1.2 (b) show the profiles of the coolant mean temperature T_c, micro-channel bottom wall temperature T_w, and heat sink bottom wall temperature T_s along the stream-wise direction in single-phase and two-phase heat sinks, respectively. Definitions of these three temperatures are given in Fig. 1.1. For single-phase heat sinks, T_c increases fairly linearly with increasing stream-wise distance, and T_w and T_s also increase accordingly

in both thermally developing ($L_{sp,dh}$) and fully-developed ($L_{sp,ft}$) regions. The highest heat sink temperature is always encountered in the heat sink's bottom wall immediately below the micro-channel outlet as shown in Fig. 1.2(a). Assuming one-dimensional heat conduction in the base substrate, $T_{s,out}$ can be related to the micro-channel bottom wall temperature at the outlet $T_{w,out}$ by

$$T_{s,out} = T_{w,out} + \frac{q''_{eff} H_w}{k_s} \tag{4.1}$$

Since H_w is not part of the present thermal design procedure and should be made as small as possible, $T_{w,out}$ is used in the present study to represent T_{max}, $T_{max} = T_{w,out}$. $T_{w,out}$ is related to the coolant mean temperature at the outlet $T_{c,out}$ by applying the fin analysis method [30] to the unit cell shown in Fig. 1.1.

$$T_{w,out} = T_{c,out} + \frac{q''_{eff}(W_{ch} + W_w)}{h_{sp}(W_{ch} + 2\eta H_{ch})} \tag{4.2}$$

where h_{sp} and η are the single-phase heat transfer coefficient and fin efficiency, respectively. Fin efficiency η is evaluated from 2.6 where m is the fin parameter, 2.7. $T_{c,out}$ can be evaluated from

$$T_{c,out} = T_{in} + \frac{q''_{eff} W L}{\rho Q_t c_{p,f}} \tag{4.3}$$

Once h_{sp} is known, $T_{w,out}$ can be calculated from Eqs. 4.2 – 4.3 Predictive tools for h_{sp} are summarized in Appendix A.

For two-phase heat sinks, liquid coolant is often supplied into the heat sink in subcooled state ($T_{in} < T_{sat}$). The coolant maintains liquid state along the channel up to a location where thermodynamic equilibrium quality,

$$x_e = \frac{h - h_f}{h_{fg}} \tag{4.4}$$

reaches zero. Thereafter, the flow changes into a saturated two-phase mixture. Figure 1.2(b) illustrates the two flow regions: a single-phase liquid region,

$$L_{sp} = \frac{\rho Q_t c_{p,f}(T_{sat} T_{in})}{q''_{eff} W} \tag{4.5}$$

and a two-phase region, $L_{tp} = L - L_{sp}$. T_{sat} in Eq. (4.5) is the saturation temperature at the location of $x_e = 0$, which is evaluated using the given outlet pressure P_{out}, assuming a small pressure drop across the heat sink. In the two-phase region, T_c maintains a fairly constant value equal to T_{sat}, and T_w and T_s increase only slightly with distance [30]. $T_{w,out}$ can be evaluated from Eqs. 4.2 – 4.3 with $T_{c,out}$ replaced by T_{sat} and h_{sp} by h_{tp}, the flow boiling heat transfer coefficient. Predictive tools for h_{tp} are also summarized in Appendix A.

Pressure drop ΔP

Pressure drop ΔP across a micro-channel heat sink dictates the pump power required to operate the heat sink.

Figures 4.1(a) and 4.1(b) illustrates the flow regions in single-phase and two-phase heat sinks, respectively. For single-phase heat sinks, ΔP is the sum of pressure drops across hydrodynamically developing ($L_{sp,dh}$) and fully-developed ($L_{sp,fh}$) flow regions, as well as pressure losses and recoveries associated with the contraction and expansion, respectively, at channel inlet and outlet. The total pressure drop can be expressed as

$$\Delta P = \Delta P_c + \Delta P_{sp,dh} + \Delta P_{sp,fh} + \Delta P_e \tag{4.6}$$

Predictive tools for evaluating the pressure drop components in Eqs. (4.6) are summarized in Appendix A.

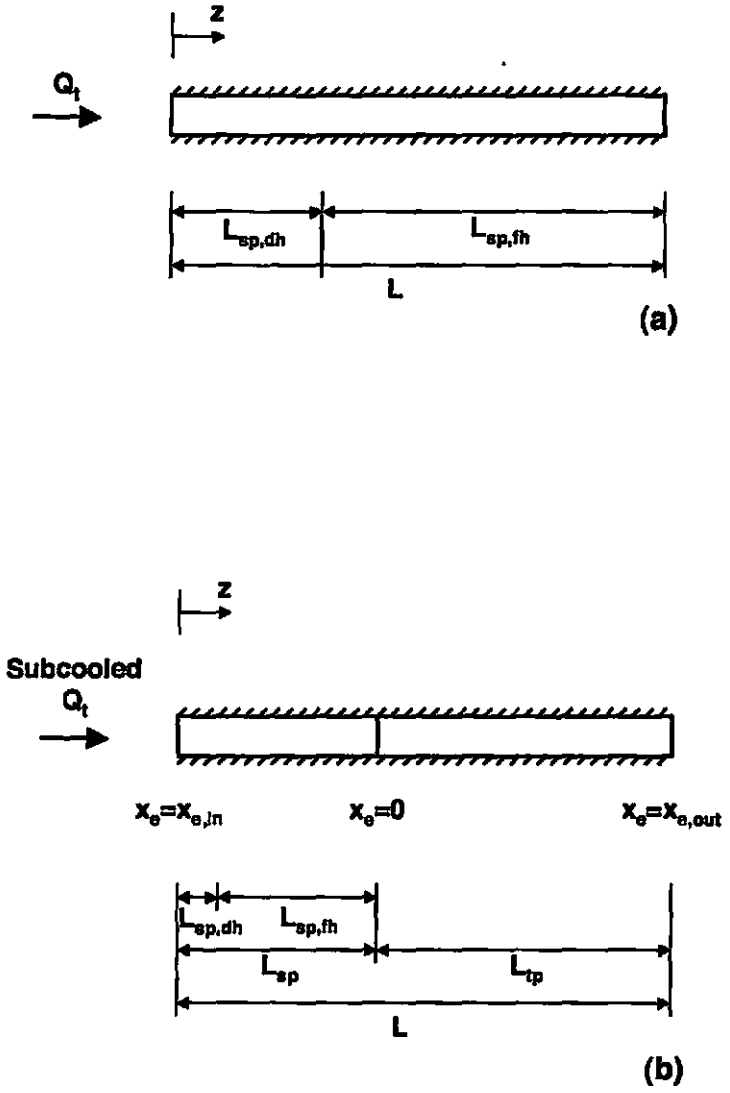

Figure 4.1: Flow regions in (a) single-phase and (b) two-phase heat sinks.

For two-phase heat sinks,ΔP includes pressure drops across both single-phase and two-phase regions, as shown in Fig. 4.1(b). The total pressure drop can be expressed as

$$\Delta P = \Delta P_c + \Delta P_{sp,dh} + \Delta P_{sp,fh} + \Delta P_{tp} + \Delta P_e \tag{4.7}$$

where ΔP_{tp} is the pressure drop across the two-phase region, which can be further expressed as the sum of frictional and accelerational components.

$$\Delta P_{tp} = \Delta P_{tp,f} + \Delta P_{tp,a} \tag{4.8}$$

Predictive tools for evaluating all the pressure drop components in Eqs. (4.7) and (4.8) are summarized in Table Appendix A.

Single-phase minimum flow rate $Q_{t,spmin}$

Single-phase minimum flow rate $Q_{t,spmin}$ is the lowest flow rate that can sustain coolant liquid single-phase flow in the micro-channels for a given q''_{eff}. It represents the coolant flow rate that causes boiling incipience to first occur at the channel outlet and below which any Q_t value would yield subcooled flow boiling in the micro-channels. Subcooled flow boiling indicates a transitional flow boiling regime between single-phase flow and saturated flow boiling. The conditions of subcooled flow boiling can be represented by $T_{w,out} > T_{sat}$ and $x_{e,out}$. It is undesirable to operate micro-channel heat sinks in subcooled flow boiling regime due to its transitional nature that often causes severe flow instability. Because of this there are few studies available in the literature on subcooled flow boiling heat transfer in micro-channel heat sinks. In the present thermal design methodology, $Q_{t,spmin}$ is set equal to the flow rate value when the micro-channel bottom wall temperature at the outlet $T_{w,out}$ is equal to the coolant saturation temperature T_{sat} corresponding to P_{out}.

$$T_{w,out}(Q_{t,spmin}) = T_{sat} \tag{4.9}$$

Equation (4.9) together with Eqs. (4.2)-(4.3) can be used to determine $Q_{t,spmin}$. To design a single-phase heat sink, the following condition has to be satisfied.

$$Q_t > Q_{t,spmin} \tag{4.10}$$

Two-phase maximum flow rate $Q_{t,tpmax}$

Two-phase maximum flow rate $Q_{t,tpmax}$ is the highest flow rate that can sustain saturated flow boiling in the micro-channels for a given q''_{eff}. It represents the total coolant flow rate that causes saturated flow boiling to first occur at the channel outlet and above which any Q_t value would yield subcooled flow boiling in the micro-channels. Therefore, $Q_{t,tpmax}$ is set equal to the coolant flow rate value corresponding to zero thermodynamic equilibrium quality at the channel outlet, $x_{e,out}$. From Eq. (4.5),

$$L = L_{sp} = \frac{\rho Q_{t,tpmax} c_{p,f}(T_{sat} - Tin)}{q''_{eff} W} \tag{4.11}$$

Rearranging Eq. (4.11) yields the relation for $Q_{t,tpmax}$.

$$Q_{t,tpmax} = \frac{q''_{eff} W L}{\rho Q_{t,tpmax} c_{p,f}(T_{sat} - Tin)} \tag{4.12}$$

Two-phase minimum flow rate $Q_{t,tpmin}$

Two-phase minimum flow rate $Q_{t,tpmin}$ is the lowest flow rate that can still sustain effective cooling by saturated flow boiling in the micro-channels for a given heat flux q''_{eff}. It represents the coolant flow rate that causes critical heat flux (CHF) condition to first occur in the micro-channels and below which any Q_t value would precipitate a sudden large decrease in heat transfer coefficient and increase in heat sink temperature, which can lead to permanent device failure. In the present thermal design methodology, $Q_{t,tpmin}$ is set equal to the flow rate value when the critical heat flux (CHF), q''_{max}, in the heat sink is

equal to q''_{eff}.

$$q''_{max}(Q_{t,tpmin}) = q''_{eff} \tag{4.13}$$

Critical heat flux in two-phase micro-channel heat sinks q''_{max} is evaluated by a recent CHF correlation [18]. At very low coolant flow rates, however, the CHF correlation yields a heat flux value higher than the input heat flux value required to convert all the liquid to saturated vapor at channel outlet, $x_{e,out} = 1$. Under these conditions, the input heat flux corresponding to $x_{e,out} = 1$ is used for q''_{max}. A summary of the predictive relations for q''_{max} is given in Appendix A. To design a two-phase heat sink, the following condition has to be satisfied.

$$Q_{t,tpmin} \leq Q_t \leq Q_{t,tpmax} \tag{4.14}$$

4.1.4 Characterstics of Heat Sink Parameters

A water-cooled copper micro-channel heat sink with planform dimensions (W×L) of 1×1 cm^2 is used to illustrate the general trends of the aforementioned thermal/fluid parameters. The micro-channel height H_{ch} is selected to be 1000 μm. Four (W_{ch},W_w) combinations (50 × 50, 50 × 100, 100 × 50, 100 × 100 μm^2) are examined. T_{in} and P_{out} are set to be 25°C and 1.2 bar, respectively.

Figure 4.2(a) shows the variations of $Q_{t,spmin}$, $Q_{t,tpmax}$, and $Q_{t,tpmin}$ with q''_{eff} for the (W_{ch},W_w) combination of (50 × 50 μ m^2). $Q_{t,spmin}$, $Q_{t,tpmax}$, and $Q_{t,tpmin}$ increase with increasing q''_{eff}. The three lines divide the plot into four regions: a single-phase region ($Q_t \geq Q_{t,spmin}$), a subcooled flow boiling region ($Q_{t,tpmax} \leq Q_t \leq Q_{t,spmin}$), a two-phase (saturated flow boiling) region ($Q_{t,tpmin} \leq Q_t \leq Q_{t,tpmax}$), and a post-CHF region ($Q_t \leq Q_{t,tpmin}$).

Figure 4.2(b) shows the variations of $Q_{t,spmin}$, $Q_{t,tpmax}$, and $Q_{t,tpmin}$ with q''_{eff} for the four (W_{ch},W_w) combinations. It is shown that $Q_{t,tpmax}$ is a function of q''_{eff} alone and

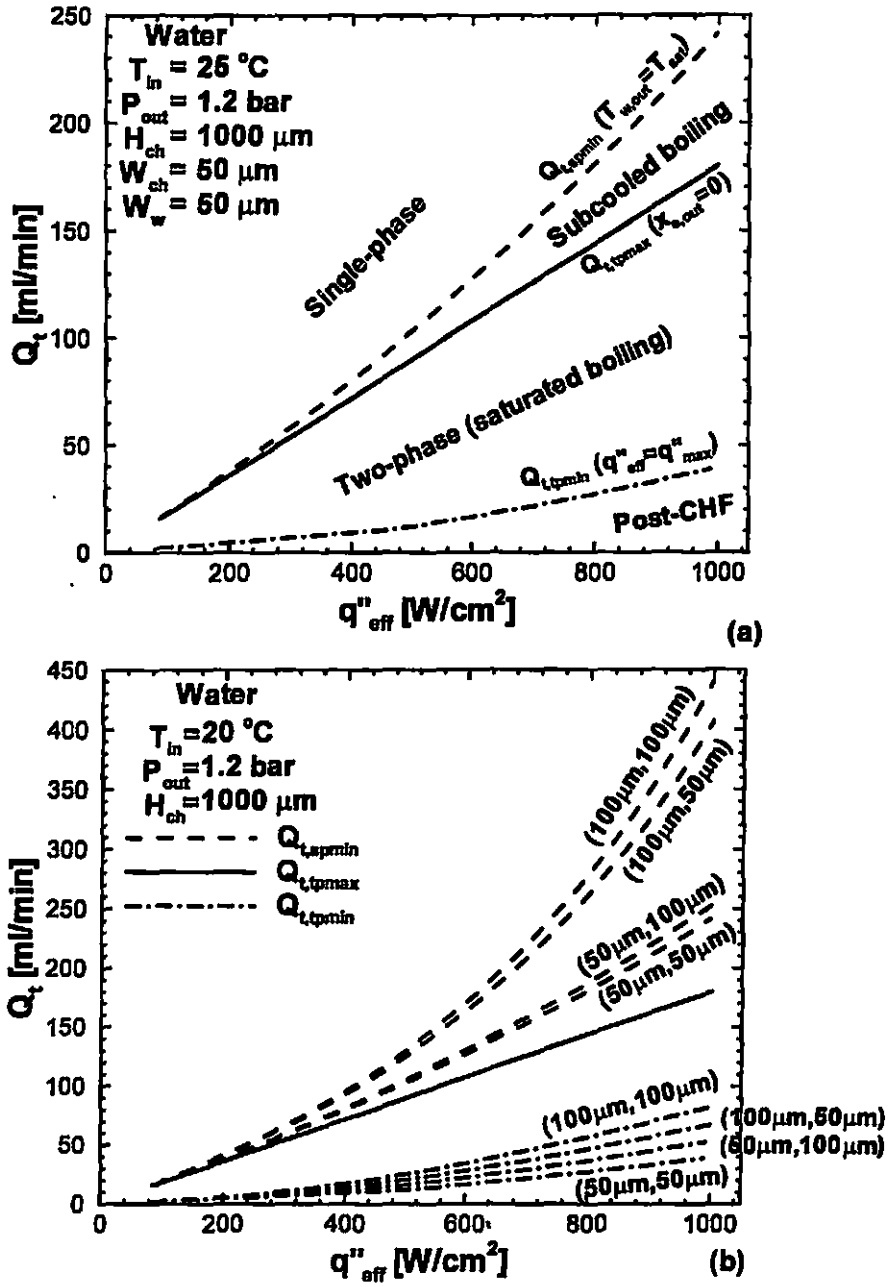

Figure 4.2: Variations of single-phase minimum flow rate, two-phase maximum flow rate, and two-phase minimum flow rate with effective heat flux for (a) (W_{ch}, W_w) combination of (50×50 μm^2), and (b) (W_{ch}, W_w) combinations of (50×50, 50×100, 100×50, 100×100 μm^2).

increases with increasing q''_{eff}. $Q_{t,spmin}$ and $Q_{t,tpmin}$, on the other hand, depend not only on q''_{eff} but channel dimensions (W_{ch},W_w) as well. The dependence of $Q_{t,spmin}$ and $Q_{t,tpmin}$ on the micro-channel dimensions will be discussed in a later section. For given micro-channel dimensions, $Q_{t,spmin}$ and $Q_{t,tpmin}$ increase with increasing q''_{eff}.

Figure 4.3 shows the variations of $T_{w,out}$ and ΔP with Q_t in single-phase region ($Q_t \geq Q_{t,spmin}$) for the four (W_{ch},W_w) combinations and $q''_{eff} = 600$ W/cm^2. $T_{w,out}$ and ΔP are functions of both Q_t and micro-channel dimensions as illustrated in Fig. 4.3. For fixed channel dimensions, $T_{w,out}$ decreases with increasing Q_t, while ΔP increases with increasing Q_t. The dependence of $T_{w,out}$ and ΔP on micro-channel dimensions will be discussed in a later section.

Figure 4.4 shows the variations of $T_{w,out}$ and ΔP with Q_t in two-phase region ($Q_{t,tpmin} \leq Q_t \leq Q_{t,tpmax}$) for the four ($W_{ch}$,$W_w$) combinations and $q''_{eff} = 600$ W/cm^2. $T_{w,out}$ and ΔP are also functions of both Q_t and micro-channel dimensions as shown in Fig. 4.4. For fixed channel dimensions, $T_{w,out}$ increases with increasing Q_t in the low Q_t region, and decreases slightly in the high Q_t region. ΔP decreases with increasing Q_t in the low Q_t region, but could either increase or decrease in the high Q_t region depending on micro-channel dimensions. The dependence of ΔP and $T_{w,out}$ on micro-channel dimensions will be discussed in a later section.

Figure 4.5 illustrates the dependence of $Q_{t,spmin}$ on micro-channel dimensions by showing constant $Q_{t,spmin}$ lines in a W_{ch}–W_w plane for $q''_{eff} = 600$ W/cm^2. $Q_{t,spmin}$ decreases with decreasing W_{ch} and W_w, and reaches the lowest value at the left lower corner of each plot, i.e., for the lowest W_{ch} and W_w values.

Figure 4.6 illustrates the dependence of $Q_{t,tpmin}$ on micro-channel dimensions by showing constant $Q_{t,tpmin}$ lines in a W_{ch}–W_w plane for $q''_{eff} = 600$ W/cm^2. $Q_{t,tpmin}$ also decreases with decreasing W_{ch} and W_w, and reaches the lowest value at the lowest W_{ch} and W_w values. For $q''_{eff} = 600$ W/cm^2, Eq. (4.14) yields $Q_{t,tpmax} = 108.05$ ml/min, independent of W_{ch} or W_w. The dashed line corresponding to in Fig. 4.4 sets an upper limit for the region of the W_{ch}–W_w plane where Eq. (4.14) is valid, i.e. where $Q_{t,tpmin} \leq Q_t \leq Q_{t,tpmax}$.

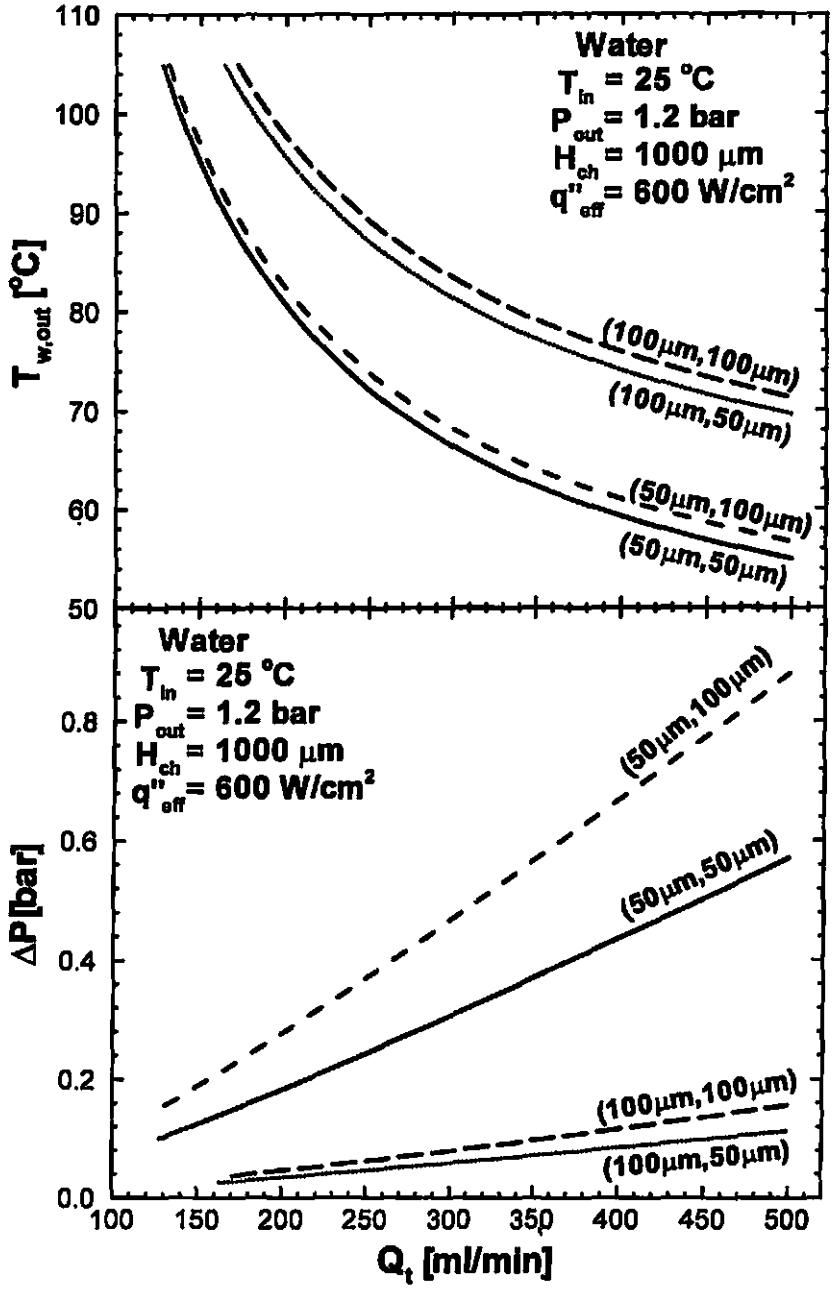

Figure 4.3: Variations of single-phase heat sink channel bottom temperature at the outlet and pressure drop with flow rate for $q''_{eff} = 600 W/cm^2$.

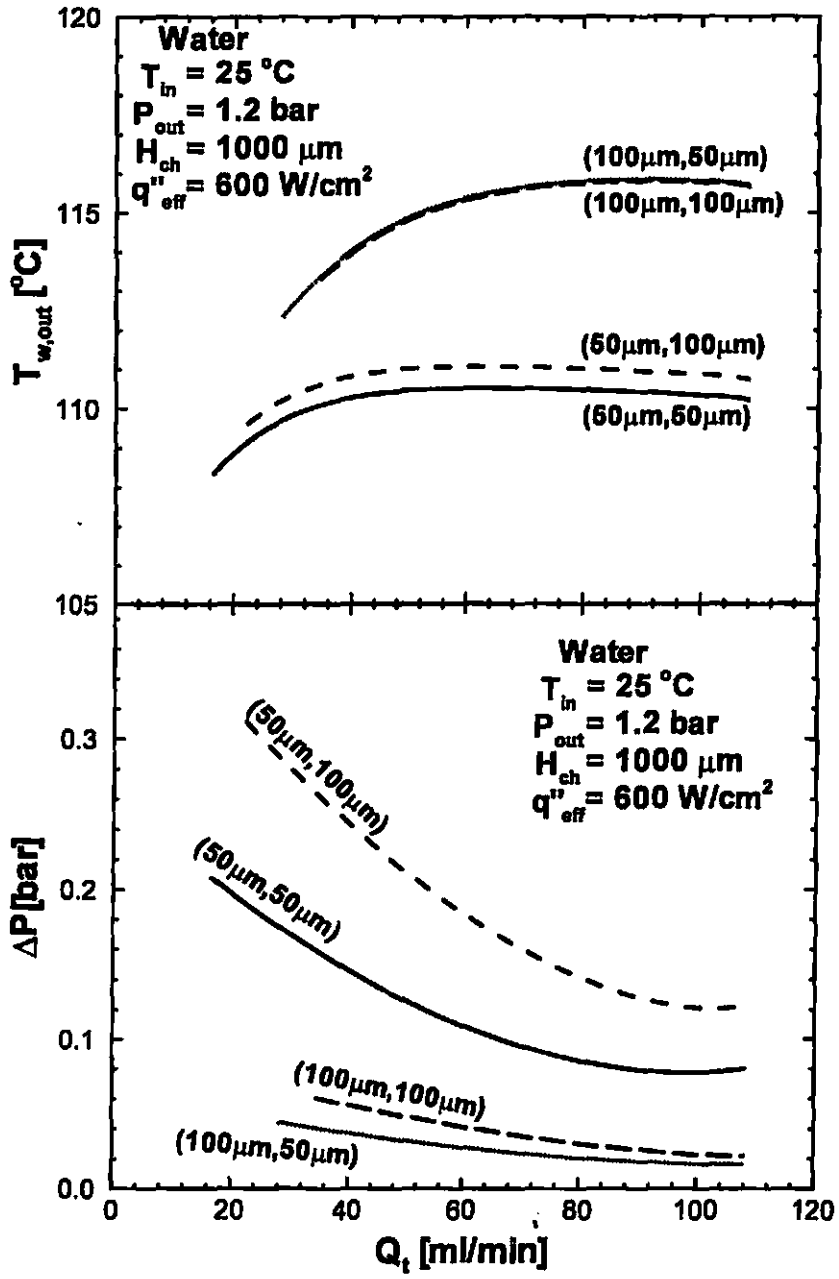

Figure 4.4: Variations of two-phase heat sink channel bottom temperature at the outlet and pressure drop with flow rate for $q''_{eff} = 600 W/cm^2$.

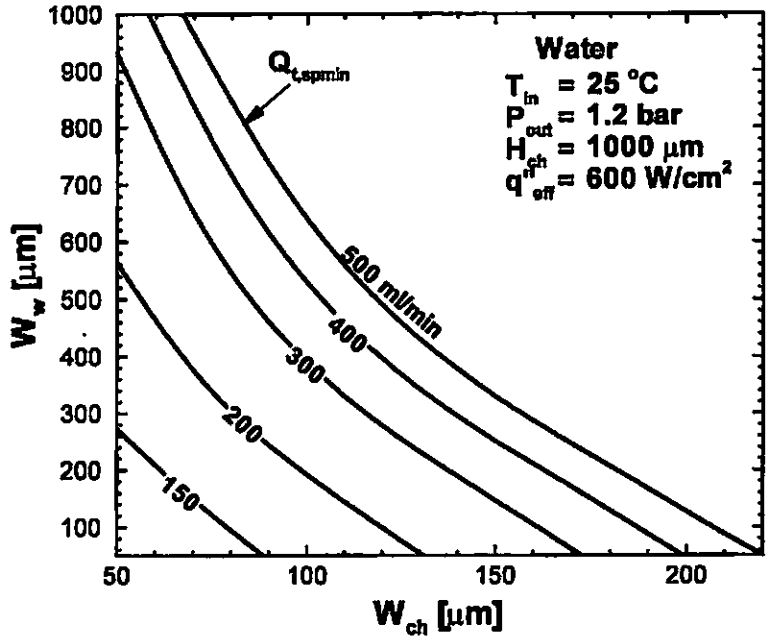

Figure 4.5: Performance map for single-phase minimum flow rate at $q''_{eff} = 600 W/cm^2$.

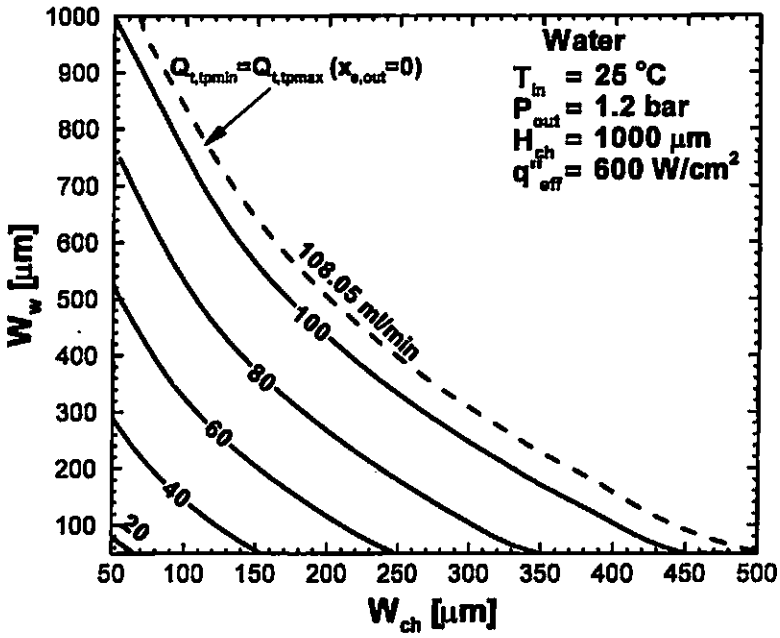

Figure 4.6: Performance map for two-phase minimum flow rate at $q''_{eff} = 600 W/cm^2$.

4.2 Heat Sink Thermal Design

In this section, a thermal design methodology for single-phase and two-phase micro-channel heat sinks under fixed coolant flow rate Q_t is explored. The water-cooled copper micro-channel heat sink is again employed to illustrate the thermal design methodology. Input parameters are summarized as follows: heat sink planform dimensions (W×L) of 1×1 cm^2, T_{in} and P_{out} of 25 $^{\circ}C$ and 1.2 bar, respectively, and device heat flux of $q''_{eff} = 600$ W/cm^2.

Maximum channel height $H_{ch,max}$, minimum channel width $W_{ch,min}$, and minimum wall thickness $W_{w,min}$ should be first identified by examining machining and/or structural limitations. In the present study, $H_{ch,max}$ is set at 1000 μm, and both $W_{ch,min}$ and $W_{w,min}$ at 50 μm. As deeper micro-channels produce better thermal performance, $H_{ch,max}$ is employed for H_{ch}, i.e. $H_{ch} = H_{ch,max}$. However, it should be noted that deeper channels will also produce a higher pressure drop. During thermal design, W_{ch} and W_w should satisfy the following relations: $W_{ch} \geq W_{ch,min}$ and $W_w \geq W_{w,min}$.

For single-phase and two-phase heat sinks, Q_t needs to satisfy Eqs. (4.10) and (4.14), respectively. When evaluating $Q_{t,spmin}$ and $Q_{t,tpmin}$ from Eqs. (4.9) and (4.13), respectively, $W_{ch,min}$ and $W_{w,min}$ should be used for micro-channel dimensions as this combination yields the lowest $Q_{t,spmin}$ and $Q_{t,tpmin}$. $Q_{t,tpmin}$, $Q_{t,tpmax}$, and $Q_{t,spmin}$ corresponding to parameters listed above are determined to be 16.52 ml/min, 108.05 ml/min, and 127.70 ml/min respectively.

4.2.1 Single-phase heat sink

A fixed flow rate of $Q_t = 500$ ml/min ($Q_t \geq Q_{t,spmin}$) is selected to illustrate the thermal design procedure for a single-phase micro-channel heat sink. Figures 4.7(a) and 4.7(b) show the output of the thermal design methodology in a W_{ch}–W_w plane. For a device heat flux of $q''_{eff} = 600W/cm^2$, the acceptable range of single-phase operation is confined to the region below the dashed line corresponding to $Q_{t,spmin} = Q_t = 500$ ml/min since only (W_{ch}, W_w) combinations that are located in this region satisfy the requirement $Q_t \geq Q_{t,spmin}$.

The next step involves evaluating $T_{w,out}$ and ΔP corresponding to micro-channel dimensions in the acceptable design region. Predictive tools given Appendix A are employed to perform the evaluation. Figures 4.7(a) and 4.7(b) show lines of constant $T_{w,out}$ and constant ΔP, respectively. Figure 4.7(a) shows Tw,out is low for small W_{ch} and small W_w, and increases with increasing W_{ch} and W_w. Figure 4.7(b), on the other hand, shows ΔP is low for large W_{ch} and small W_w, and increases with decreasing W_{ch} and increasing W_w.

Figures 4.8(a) and 4.8(b) show similar plots corresponding to a lower flow rate of Q_t = 300 ml/min. The general trends in these figures are similar to those of Figs. 4.7(a) and 4.7(b), respectively, except that the $Q_{t,spmin}$ limit is shifted towards smaller channel dimensions. A comparison of Figs. 4.7(a) and 4.8(a) shows Tw,out increases with decreasing Q_t. Comparing Figs. 4.7(b) and 4.8(b) reveals that for the same micro-channel dimensions, ΔP decreases with decreasing Q_t.

Figures such as 4.7(a)-(b) and 4.8(a)-(b) are the final output of the thermal design procedure for single-phase micro-channel heat sinks. They provide the end user with an acceptable range of (W_{ch}, W_w) combinations which can safely remove the heat for a given flow rate. The heat sink designer is left with the decision to select an acceptable combination of $T_{w,out}$ and ΔP; this latter combination dictates the dimensions (W_{ch} and W_w) of the micro-channel.

4.2.2 Two-phase heat sink

A flow rate of Q_t = 100 ml/min ($Q_{t,tpmin} \leq Q_t \leq Q_{t,tpmax}$) is selected to illustrate the thermal design procedure for a two-phase micro-channel heat sink. The design procedure is very similar to that discussed in the previous section for single- phase heat sinks. As indicated in Figs. 4.9(a) and 4.9(b), the acceptable design region under fixed Q_t is that below the dashed line corresponding to $Q_{t,tpmin} = Q_t = 100$ ml/min. Again only (W_{ch}, W_w) combinations that are located in this region satisfy the requirement . Lines corresponding to constant values of $T_{w,out}$ and ΔP are constructed in Figs. 4.9(a) and 4.9(b), respectively, within the acceptable design region. Predictive tools given in Appendix A are employed to

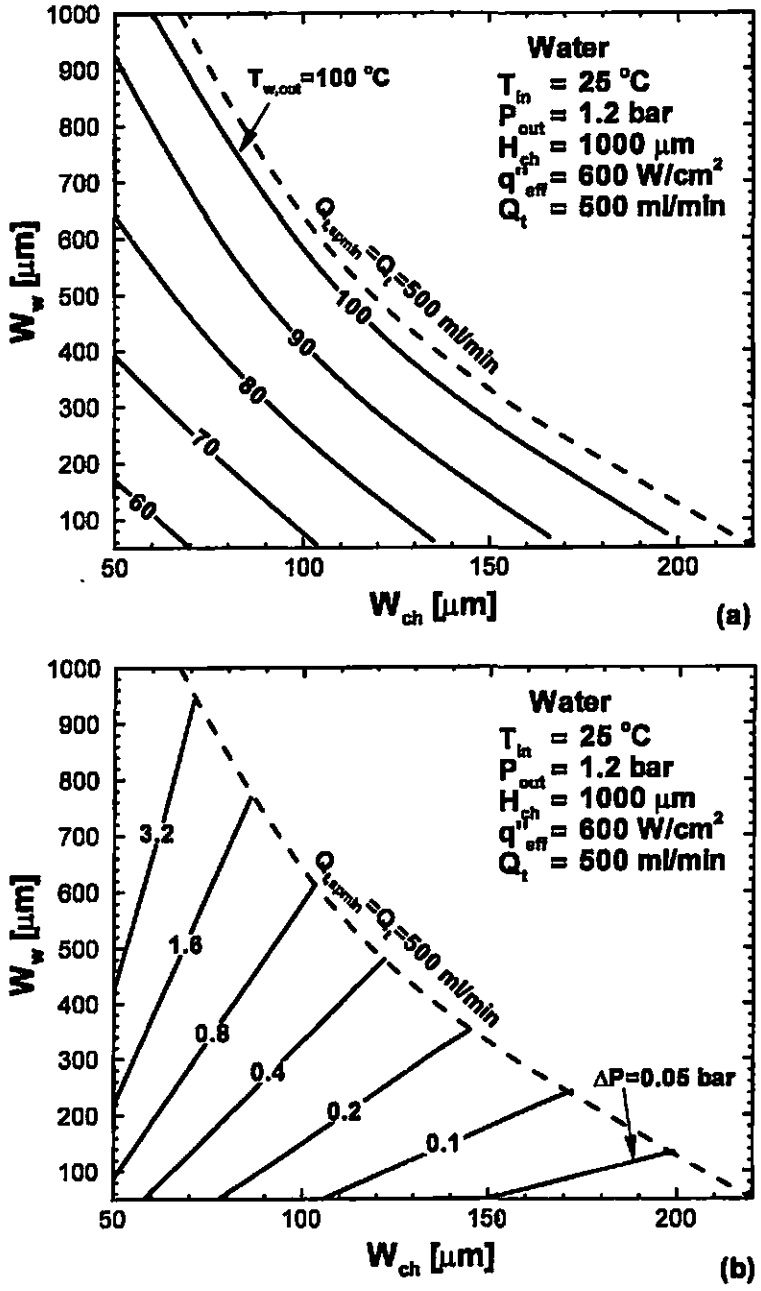

Figure 4.7: Single-phase heat sink performance map for (a) channel bottom temperature at the outlet and (b) pressure drop for $q''_{eff} = 600 W/cm^2$and Q_t = 500 ml/min.

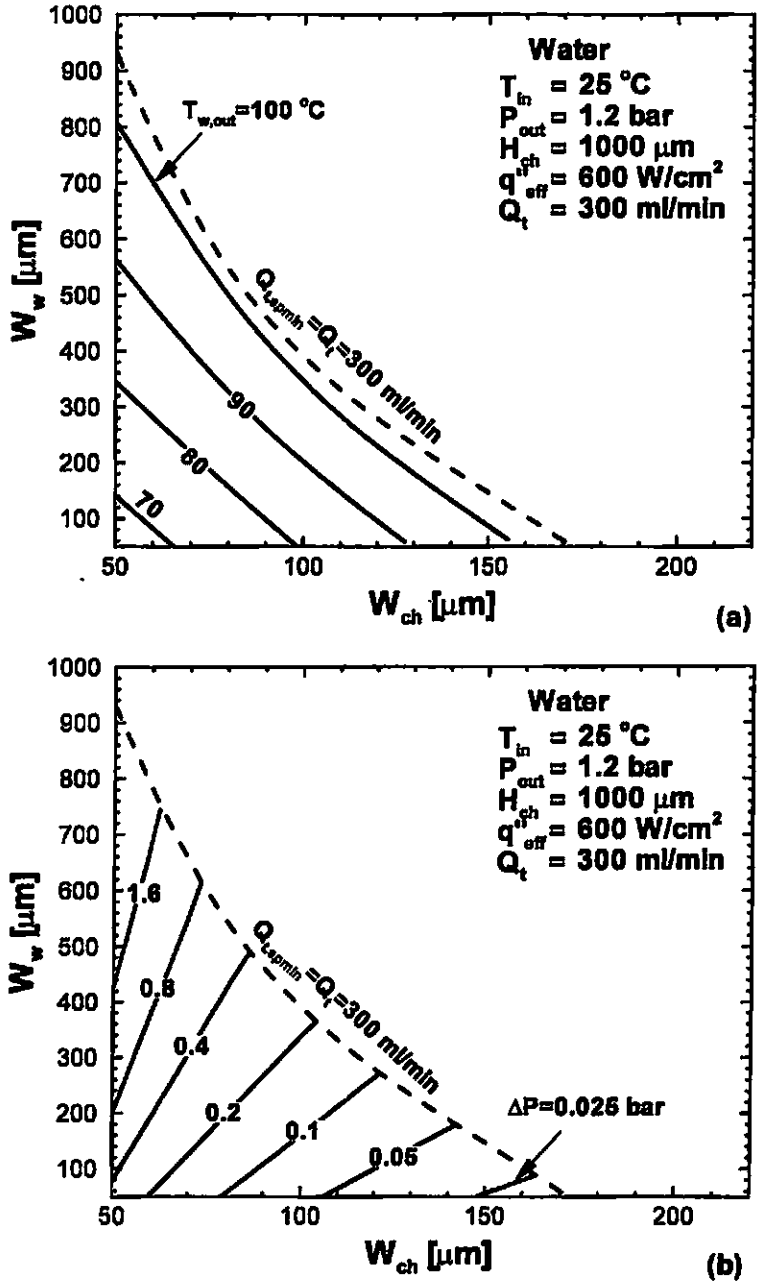

Figure 4.8: Single-phase heat sink performance map for (a) channel bottom temperature at the outlet and (b) pressure drop for $q''_{eff} = 600 W/cm^2$and $Q_t = 300$ ml/min.

conduct the evaluation of Tw,out and ΔP. Figure 4.9(a) shows $T_{w,out}$ is low for small W_{ch} and small W_w, and increases with increasing W_{ch}h. Figure 4.9(b), on the other hand, shows ΔP is low for large W_{ch} and small W_w, and increases with decreasing Wch and increasing W_w.

Figures 4.10(a) and 4.10(b) show similar plots corresponding to a lower flow rate of Q_t = 60 ml/min. The general trends in these figures are similar to those of Figs. 4.9(a) and 4.9(b), respectively, except that the $Q_{t,tpmin}$ limit is shifted towards smaller channel dimensions. A comparison of Figs. 4.9(a) and 4.10(a) shows $T_{w,out}$ decreases with decreasing Q_t. These trends are valid only for low values of Q_t; high Q_t values are expected to yield the opposite trend as shown in Fig. 4.4. Comparing Figs. 4.9(b) and 4.10(b) reveals that for the same micro-channel dimensions, ΔP increases with decreasing Q_t. This is because pressure drop in the two-phase region is higher than in the single-phase region. With a lower flow rate, two-phase flow occupies a larger portion of the micro-channel length, resulting in higher total pressure drop.

Similar to thermal design of single-phase heat sinks, figures such as 4.9(a)-(b) and 4.10(a)-(b) are the final output of the design methodology corresponding to a fixed Q_t for two-phase micro-channel heat sinks. The heat sink designer is left with the decision to select an acceptable combination of $T_{w,out}$ and ΔP based upon which the channel dimensions (W_{ch} and W_w) are determined.

4.3 Summary

Figure 4.11 shows a flow chart that summarizes the procedure for thermal design of a single-phase or two-phase micro-channel heat sink under fixed coolant flow rate.

This chapter concerns thermal design of single-phase and two-phase micro-channel heat sinks. Heat sink parameters and predictive tools were first summarized, and followed by a discussion of the characteristics of thermal/fluid parameters. Finally, a thermal design

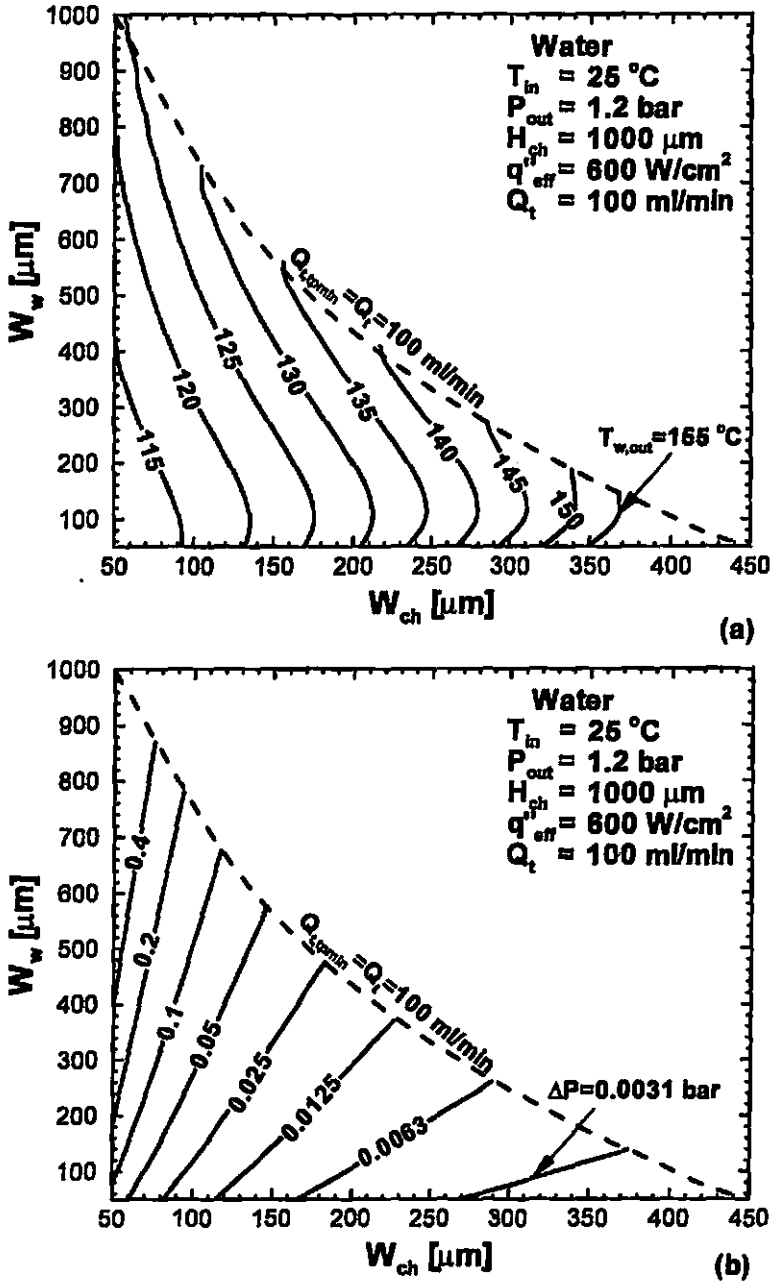

Figure 4.9: Two-phase heat sink performance map for (a) channel bottom temperature at the outlet and (b) pressure drop for $q''_{eff} = 600 W/cm^2$ and $Q_t = 100$ ml/min.

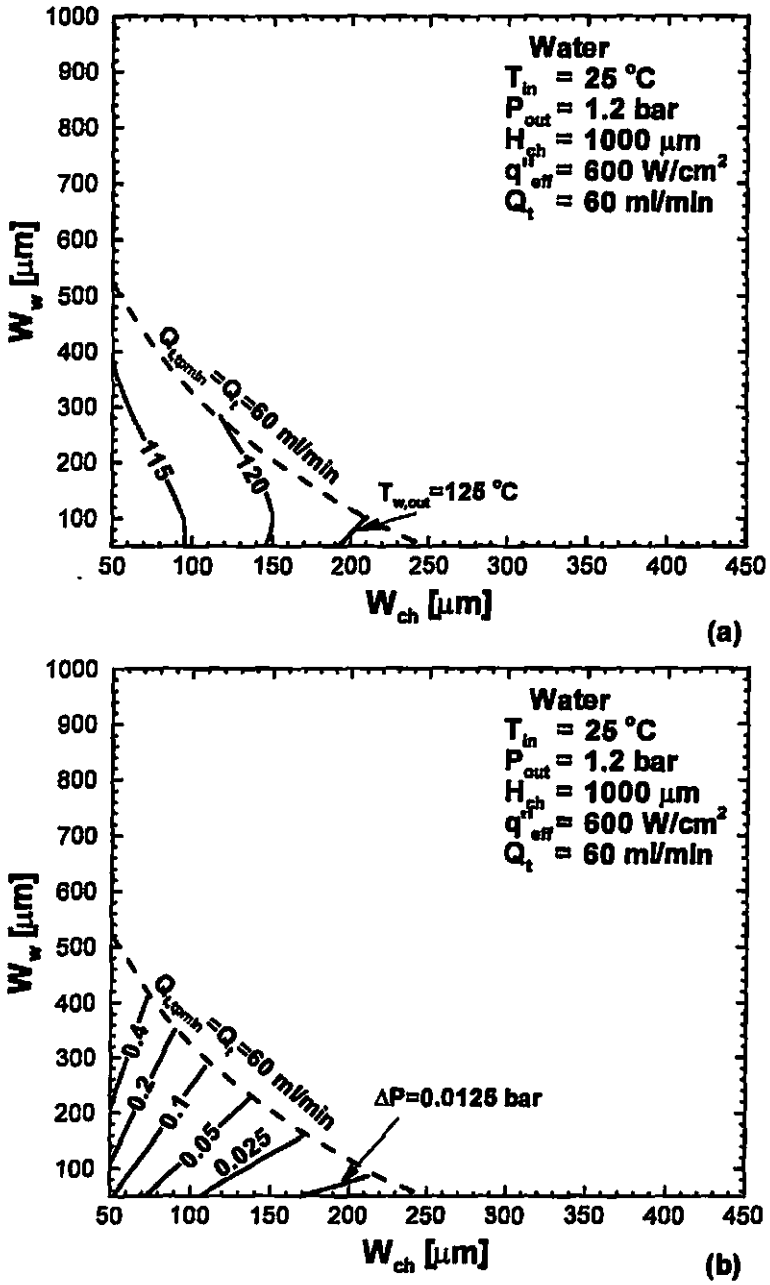

Figure 4.10: Two-phase heat sink performance map for (a) channel bottom temperature at the outlet and (b) pressure drop for $q''_{eff} = 600 W/cm^2$ and $Q_t = 60$ ml/min.

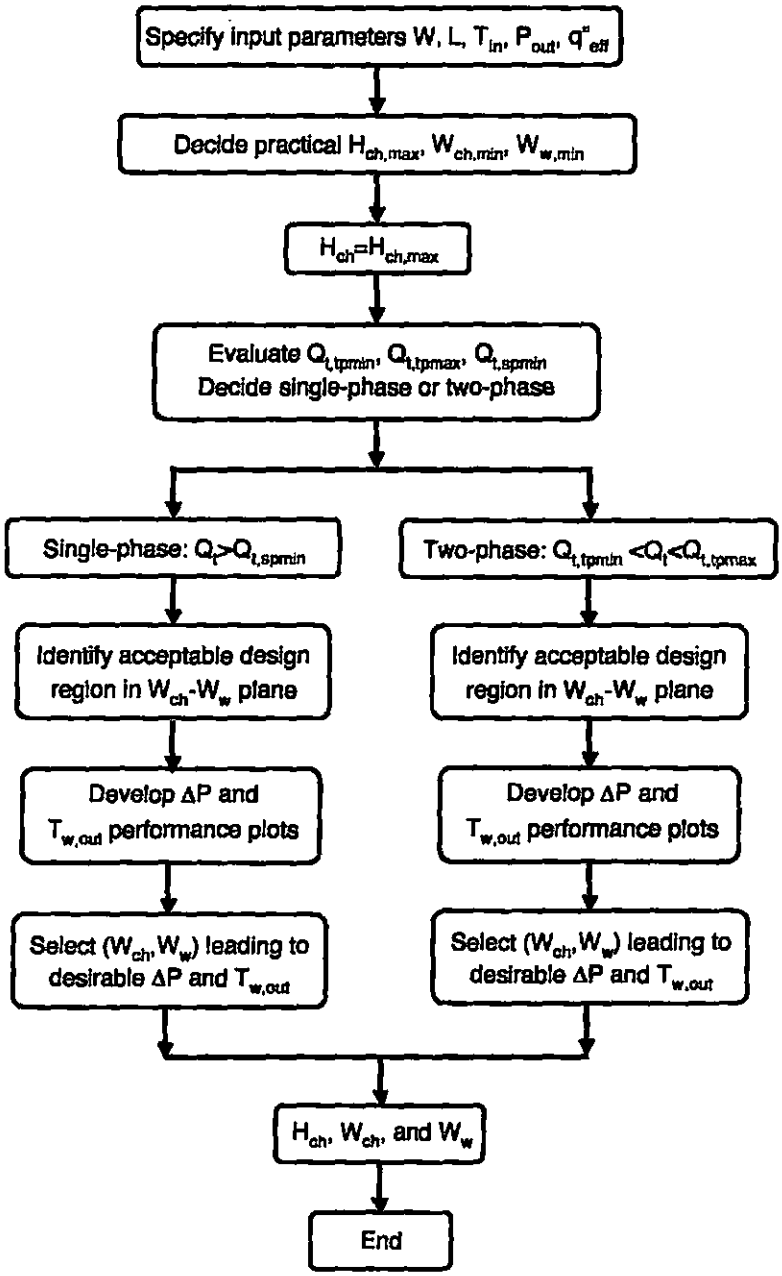

Figure 4.11: Flow chart of design procedure for single-phase and two-phase micro-channel heat sinks under fixed coolant flow rate.

methodology was developed for the condition of fixed coolant flow rate. Only low flow rate corresponding to laminar flow in micro-channels is considered.

The heat sink parameters can be grouped into geometrical parameters, operating parameters, and thermal/fluid parameters. Geometrical parameters include heat sink and micro-channel dimensions. In heat sink design, heat sink dimensions and operating parameters are often specified beforehand. Thermal/fluid parameters are output parameters of this methodology that describe the heat sink and is used to guide the designer in selecting most desirable micro-channel dimensions.

A design procedure for single-phase and two-phase micro-channel heat sinks under the conditions of a fixed, uniform, device heat flux and fixed coolant flow rate is developed. This procedure yields an acceptable design region encompassing all possible micro-channel dimensions, and provides predictions for highest heat sink temperature and pressure drop from which a designer can select most desirable channel dimensions.

This design methodology is used in the experimental design for the single-phase and two-phase micro-channel heat sinks in the following chapters.

Chapter 5

Design, Fabrication, and Testing of a Water Cooled Single-Phase Heat Sink

A single-phase micro-channel heat sink is designed using the thermal design methodology that was developed in Chapter 4. An experimental system that is composed of micro-channel heat sink test module, flow loop, and instrumentation was constructed. Experiments were conducted to evaluate the thermal performance of the heat sink. This heat sink cooling system is designed for a radar amplifier.

5.1 Design Parameters

The radar amplifier had an available attachment area of 2 inches by 1.1 inches. The heat load generated by the amplifier is 80 W. The maximum allowable temperature of the amplifier is 65 $°C$. The material that the heat sink will be attached to is gold plated copper.

The approximate heat generation will be from 2 sources inside the amplifier. The sources are thermally and electrically connected to a ceramic-style plate internally which forces the heat out towards the packaging. Each heat source will generate approximately 40W of heat, for a total of 80W. The distribution of heat is that it will be primarily focused towards the bottom of the package, however due to the size and high conductivity, the heat gets distributed all around fairly rapidly with no external changes.

5.2 Experimental Design

5.2.1 Test Heater Design

The test heater is designed to simulate the amplifier. The tester heater is designed to be 2 inches in height, 2 inches in width, and 1.1 inch long. Eight holes will be made in the bottom of the test heater for insertion of cartridge heaters, each able to produce 20 W of heat for a total of 160 W, double that of the amplifier. Two rows of thermocouple holes are made along the 1.1 inch length to measure temperature in the flow direction and also to calculate the heat flux.

5.2.2 Bulk Heat Sink Design

The initial design for the micro-channel heat sink needed to have a thin substrate base to minimize the thermal resistance due to conduction through the base, but at the same time needed to be strong to support the heat sink plenums. A thin base might easily bend or break, but making it too thick would increase the maximum temperature and might cause the heat flux to no longer be uniform along the channel length.

The design also needed to be easy to put together and align all the necessary parts: the heat sink, the heat source, and the heat sink cover with a leak-proof seal.

The heat sink base substrate should be made from a solid material that has high thermal conductivity in order to reduce thermal resistance to the heat flow due to conduction. In the present design, the oxygen-free copper is used as the base substrate material, which has a thermal conductivity of 401 W/cm^2 with a polycarbonate cover plate. The two parts are bolted together to form the closed heat sink. An O-ring in the housing maintains a leak-proof seal. The heat sink will be attached to the top surface of the amplifier by using a high-thermal-conductivity epoxy that is designed for attaching heat sinks to electronic components, but for the experiment the heat sink will be pressed against the test heater with some thermal paste in between.

The final design of the assembly requires only two parts, the heat sink and the heat sink cover. This is to minimize leakage due to spaces between heat sink components.

The heat sink base substrate is a square piece of oxygen-free copper measuring 3 inch by 3 inch. Top view of the base substrate is given in Fig. 5.3. The effective heat transfer area measures 2 inch wide and 1.1 inch long. A lip around the edge ensures alignment with the cover plate. Eight holes are drilled through the base substrate for screws that will secure the cover plate to the base substrate.

Bottom view of the base substrate is provided in Fig. 5.4. The bottom of the base substrate has a machined area 2×1.1 inch that is indented for the test heater. This allows an easy alignment of the heat source (test heater with 2×1.1 inch top surface) with the aforementioned effective heat transfer area on top of the base substrate.

The cover plate is a transparent Lexan polycarbonate piece that matches that dimensions of the base substrate itself. Design of the cover plate is shown in Fig. 5.5. There are two threaded holes in the cover for the tube fittings that are later used to interface with the flow loop. An o-ring groove is made in the cover plate to hold O-ring for leak-proof seal. Eight holes are also drilled through for screws that will secure the cover plate to the base substrate. The heat sink is assembled by bolt the cover plate atop the base substrate. The cover plate and micro-slots in the base substrate top surface forms closed micro-channels. An O-ring in the cover plate maintains a leak-proof seal. The assembled micro-channel heat sink is illustrated in Fig. 5.6.

5.2.3 Micro-Channel Design

The thermal design methodology that was developed in Chapter 4 is applied to construct the performance map within the acceptable design region. The final of the heat sink has seventy-five rectangular micro-slots in the effective heat transfer area. The micro-slots are equidistantly spaced within the 2 inch width and have the cross-sectional dimensions of 370 μm wide and 750 μm deep. A practical thickness of the substrate, H_w, is made to be 6.5 mm.

With this micro-channel design the highest heat sink bottom surface temperature, $T_{s,max}$, should be 35 °C and the pressure drop across the heat sink ΔP should be 0.005 bar.

5.3 Experimental System

5.3.1 Micro-Channel Heat Sink Test Section

Micro-channels were machined into the base substrate top surface by a precision micro-end mill technique. Figure 5.8 shows close view of the micro-channels. The actual dimensions of micro-channels were measured using a microscope and determined to be 396 μm wide and 740 μm deep, which are slightly different from the designed values.

The heat sink base substrate was fabricated from a piece of oxygen-free high thermal conductivity copper. Figure 5.9 shows the complete base substrate.

Figure 5.10 shows the heat sink cover plate that was fabricated from a piece of Lexan. The cover plate is transparent so that the coolant flow in the heat sink can be visually observed.

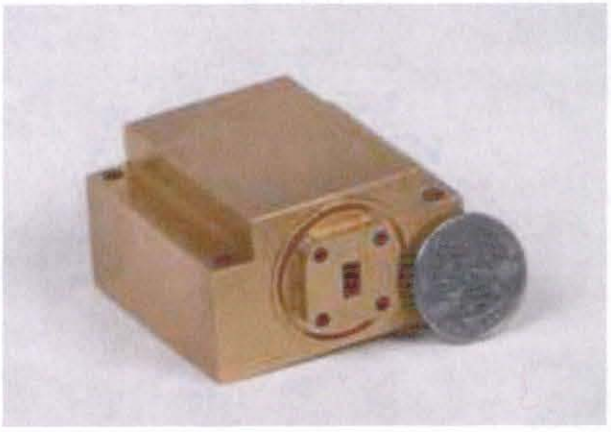

Figure 5.1: Example of the radar amplifier to be cooled

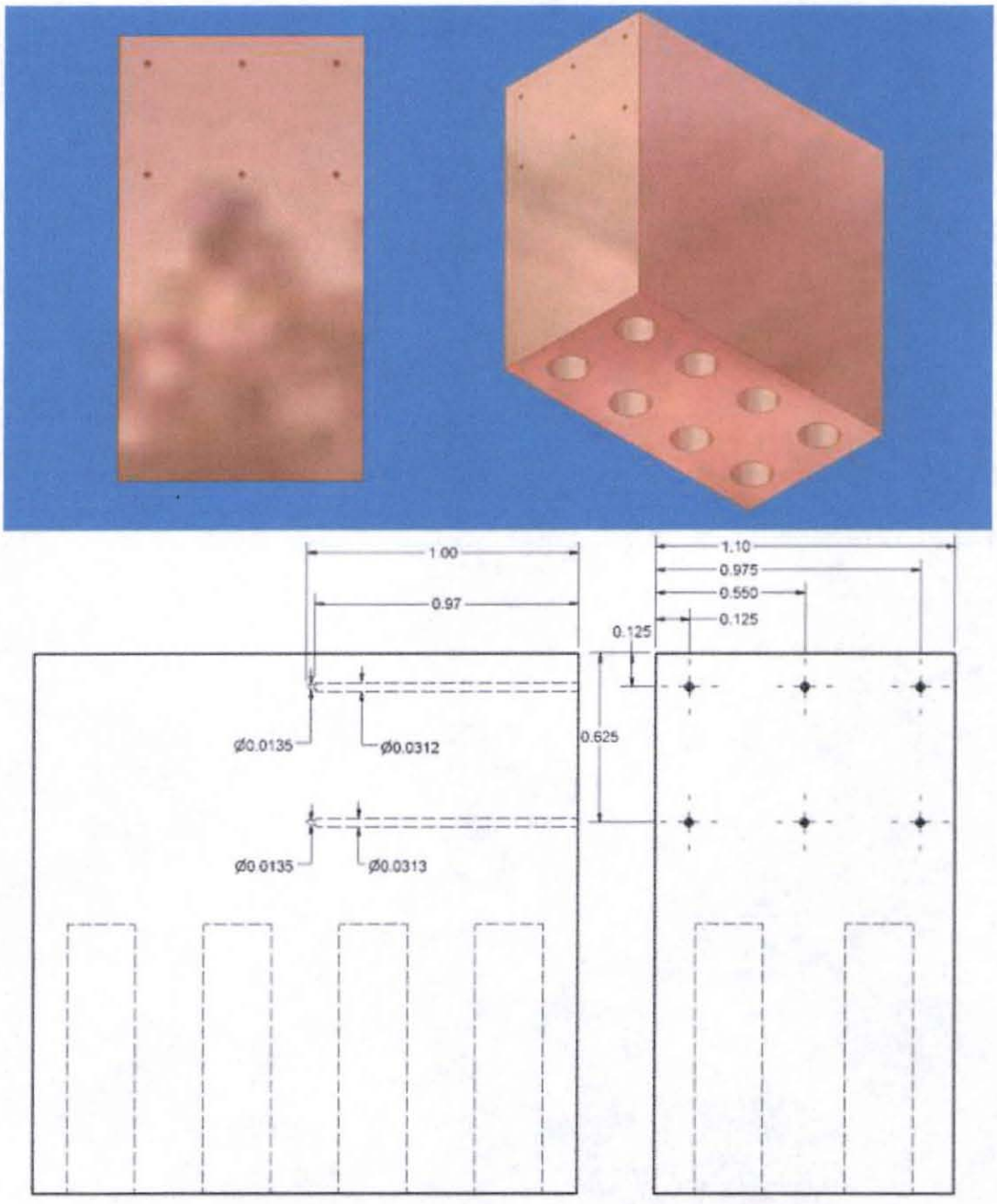

Figure 5.2: Test heater design

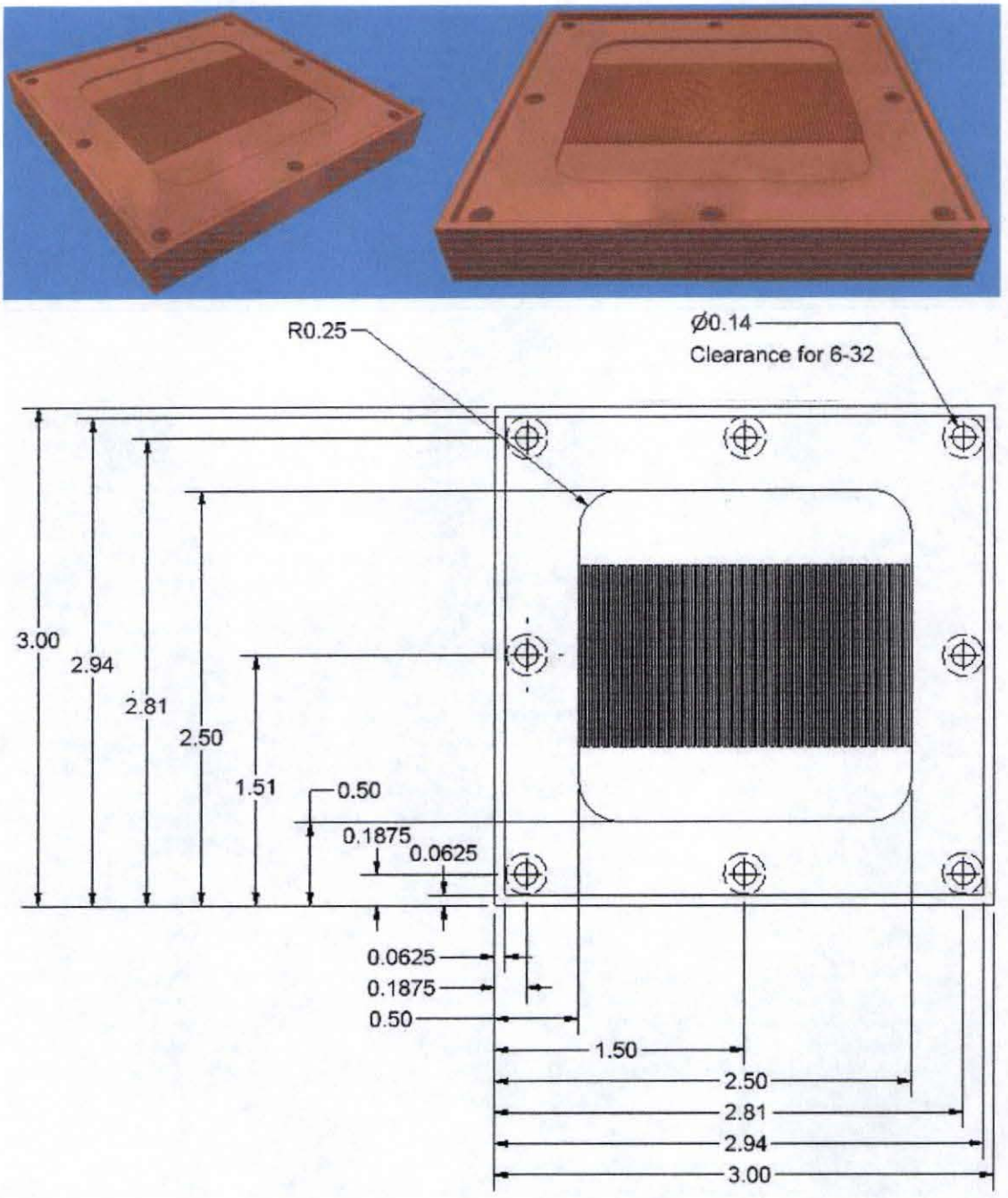

Figure 5.3: Top view of heat sink base peice

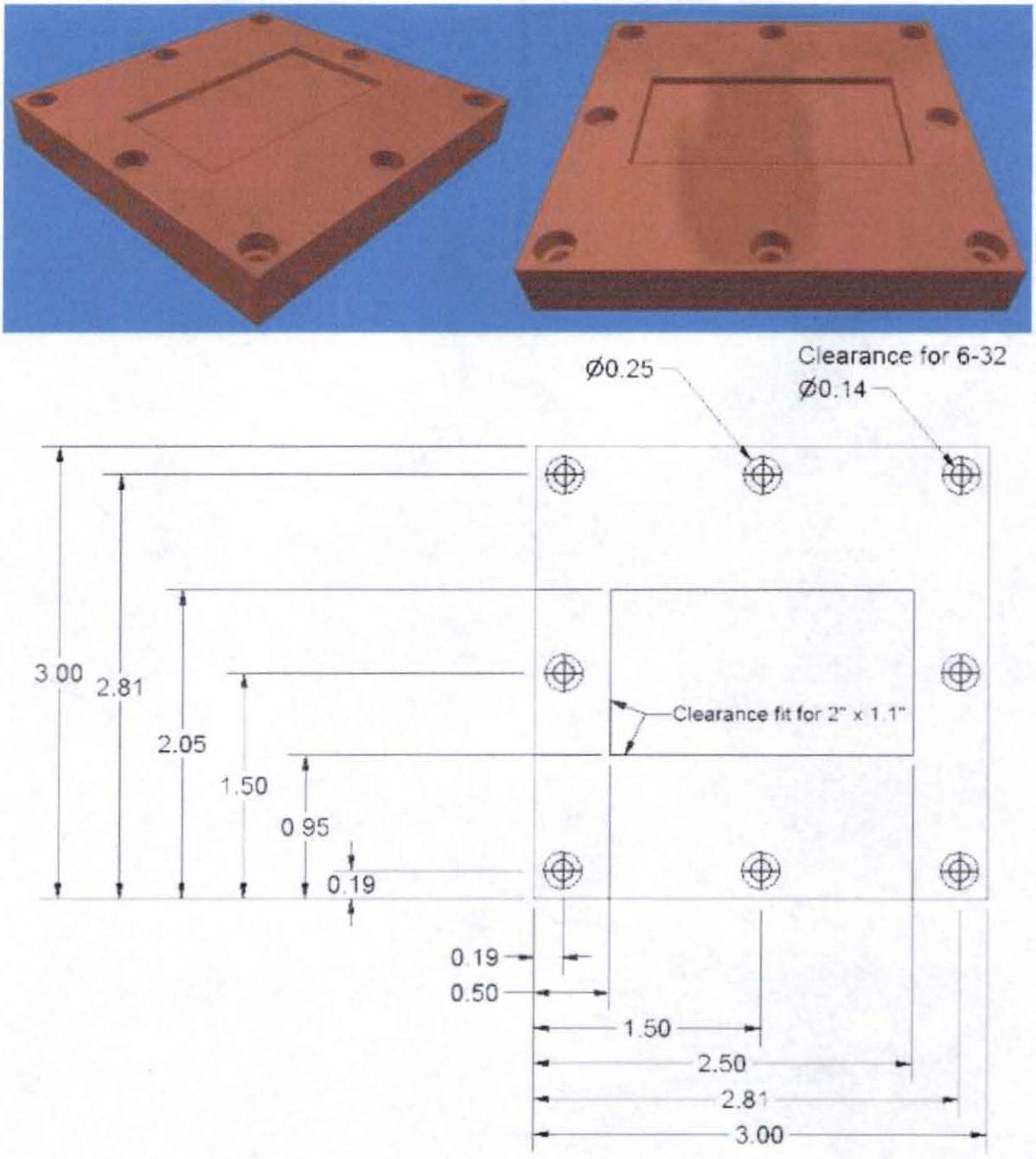

Figure 5.4: Bottom view of heat sink base piece.

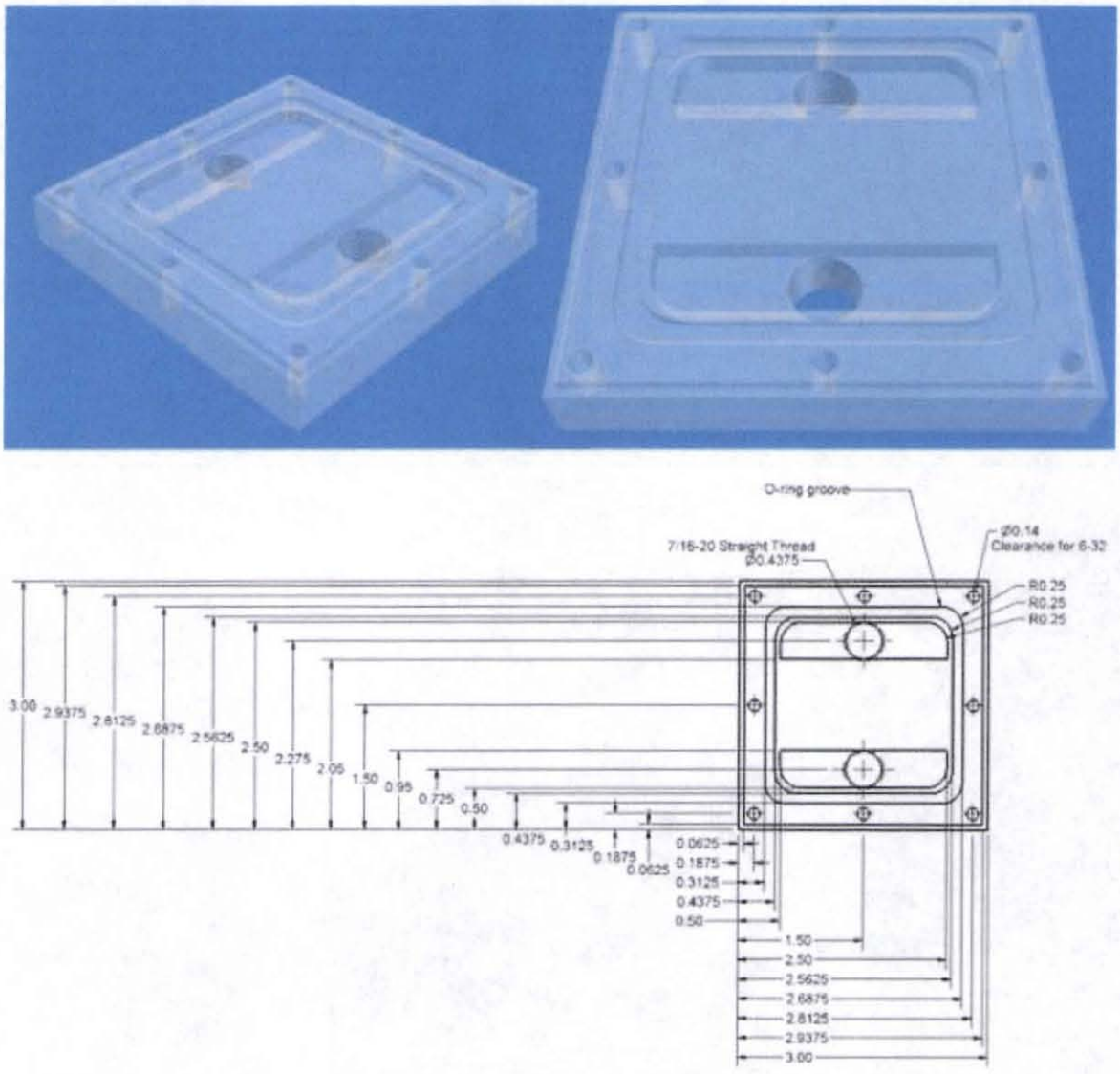

Figure 5.5: Solid model and drawing for the heat sink cover

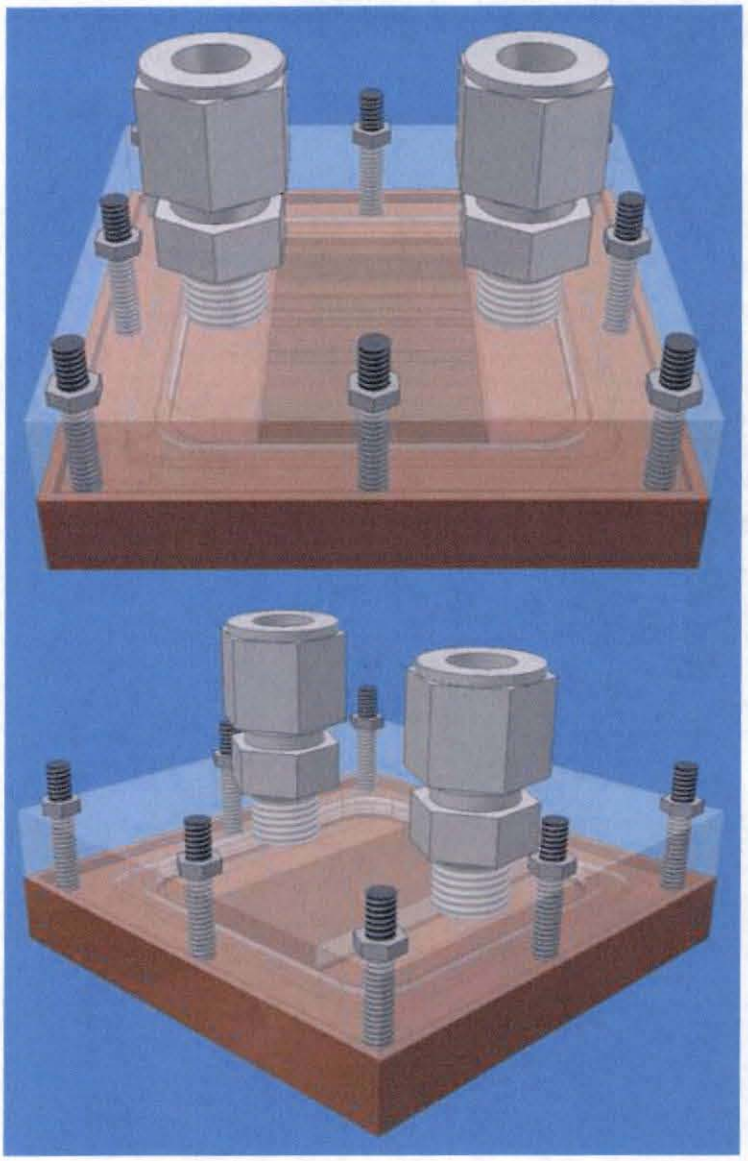

Figure 5.6: Solid model for the heat sink assembly

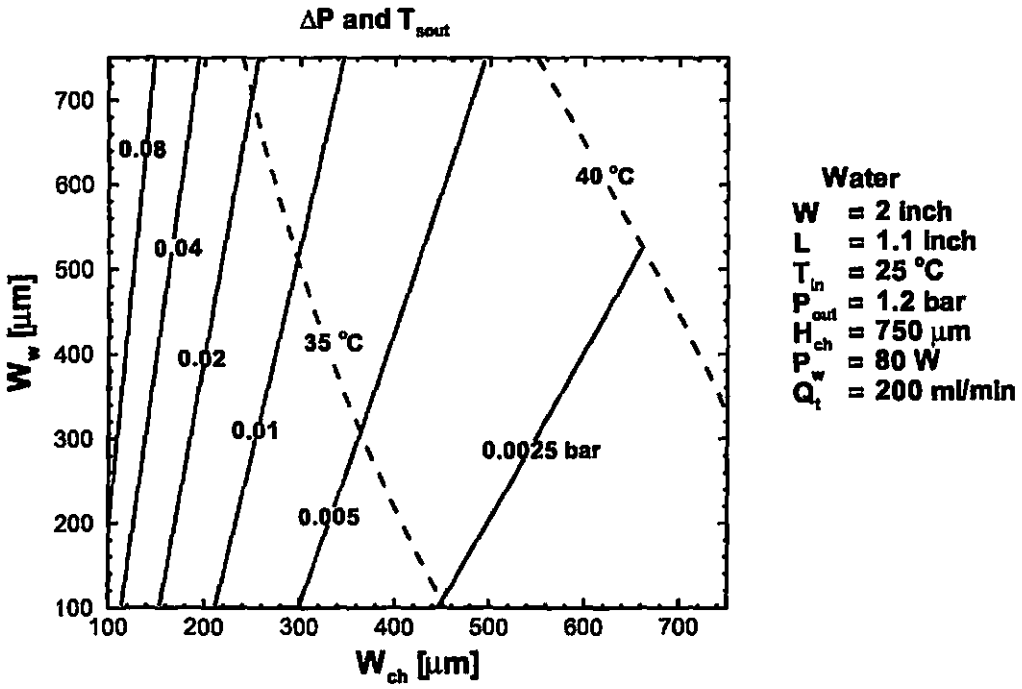

Figure 5.7: The design region for the single-phase heat sink.

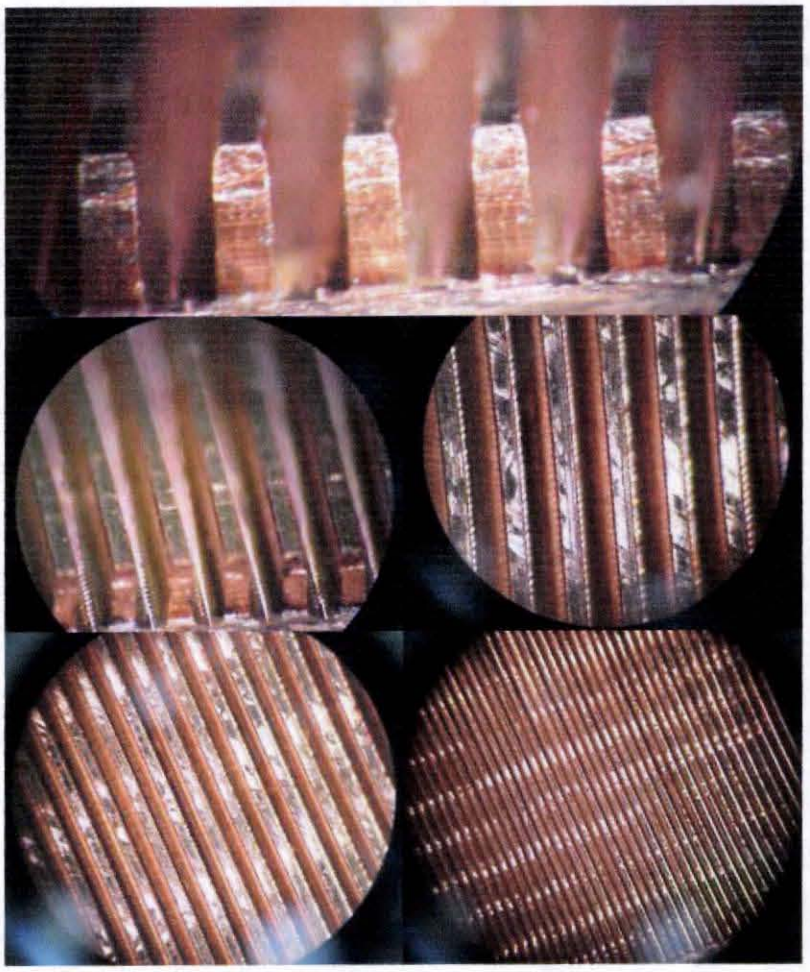

Figure 5.8: Actual micro-channels for the heat sink at various magnifications

Figure 5.9: Finished heat sink

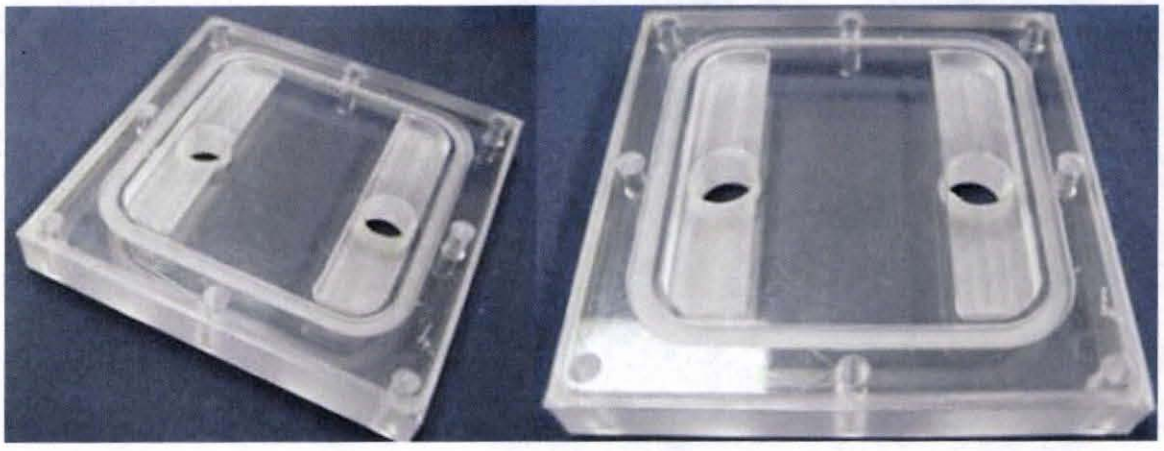

Figure 5.10: Finished heat sink cover

A test heater was employed to simulate the heat transfer characteristics of the amplifier. Figure 5.11 shows the test heater. The test heater was a block of oxygen-free copper 2 inch high by 2 inch long and 1.1 inch wide with eight holes on the drilled through the bottom to accommodate cartridge heaters that provided the desired heat load of 80 W during testing. Six small holes were drilled into the side of the test heater to accommodate thermocouples that measured the temperature distribution within the test heater along the flow direction. The test heater was attached to bottom surface of the heat sink base substrate as shown in Fig. 5.11. A small amount of thermal paste was applied to the interface to reduce the interfacial thermal resistance. During testing, insulation material was wrapped around the copper heater to prevent heat loss to the ambient.

Figure 5.13 shows the assembled heat sink that was mounted on a testing cart. Two tube fittings were connected to the cover plate, which were used to interface the heat sink with the flow loop.

Eight cartridge heaters were used to generate the desired heat load within the test heater. Each cartridge heater was 1 inch long and .25 inches in diameter. To control the power input a variable transformer was used along with a Yokogawa WT210 power meter. Cartridge heaters, the variable transformer, and the power meter are illustrated in Fig. 5.14.

Figure 5.11: Finished test heater

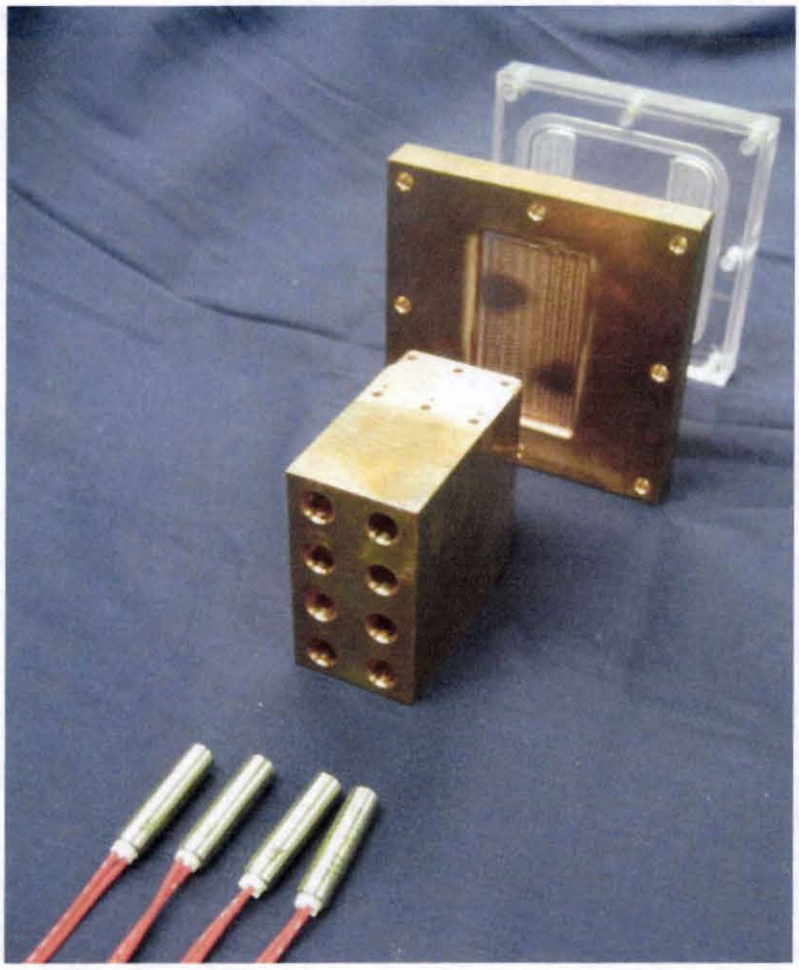

Figure 5.12: Main components of the test section, cartridge heaters, test heater, heat sink base, and cover plate.

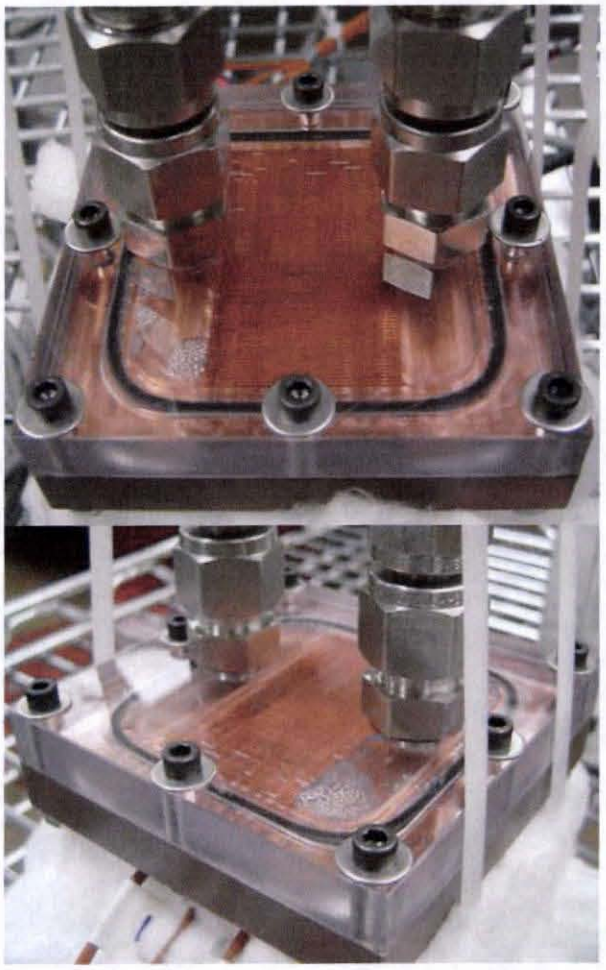

Figure 5.13: Heat sink assembled

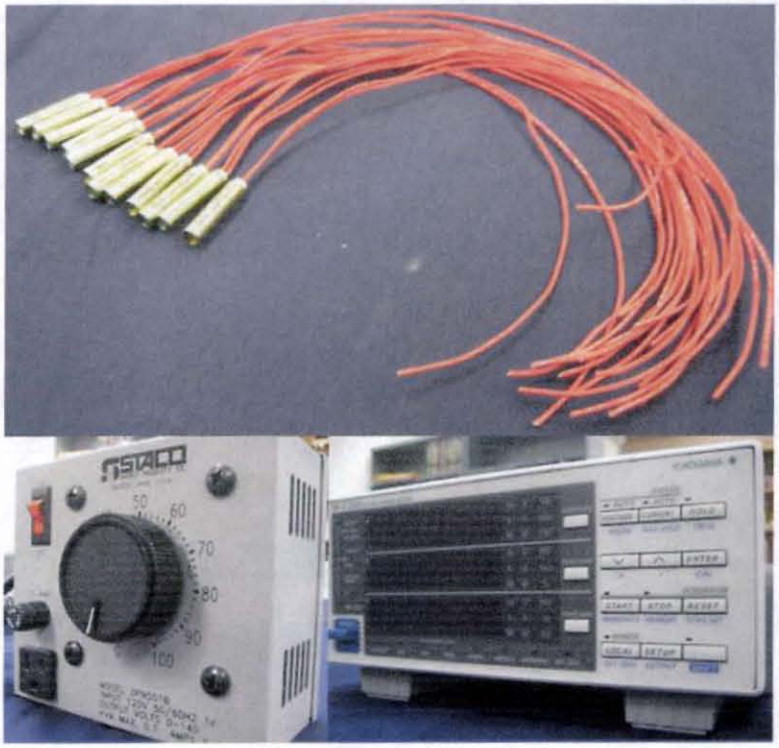

Figure 5.14: Cartridge heater power is controlled by the variable output transformer and monitored by the power meter

5.3.2 Flow Loop

The flow loop needed to be small and easy to move. The flow loop cart need to be easily interfaced with the heat sink and the device requiring cooling.

The flow loop adjusts the liquid coolant, water, to its desired operating conditions and supplies it to the mico-channel heat sink. The designed operating conditions include a water inlet temperature, T_{in}, of 25 °C, a water outlet pressure, P_{out}, of 1 atm, and a water volumetric flow rate, Q_t, of 200 ml/min.

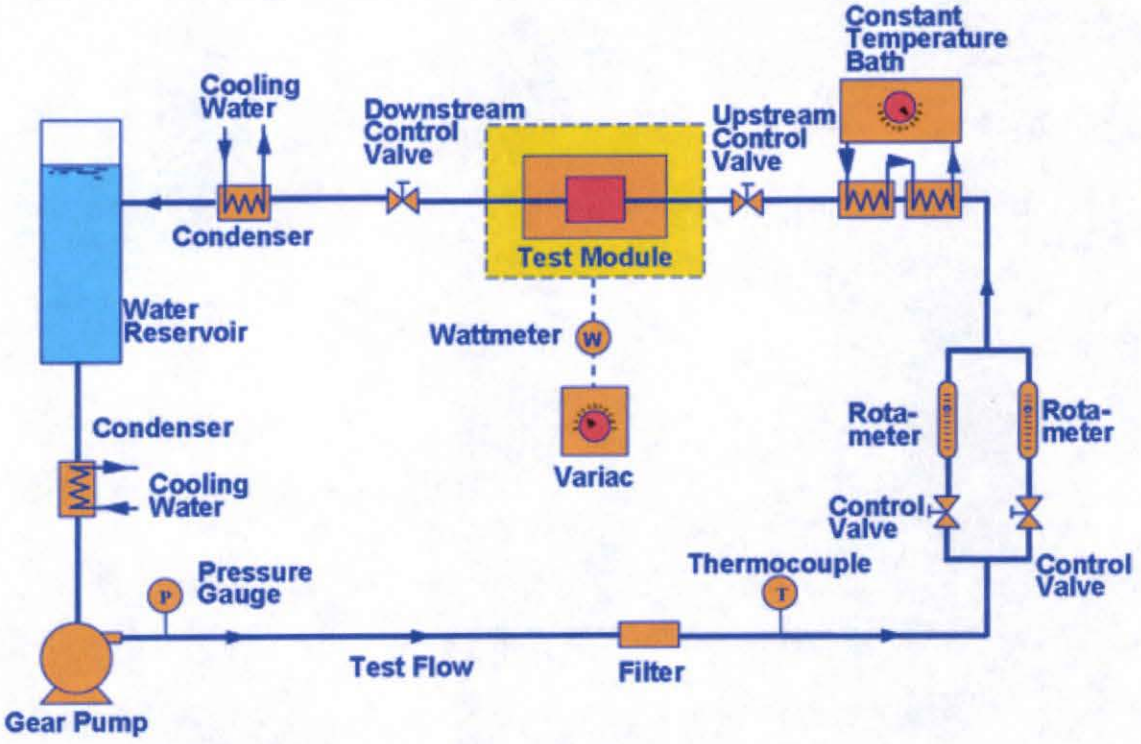

Figure 5.15: Schematic of a typical flow loop

5.3.3 Instrumentation

Two K-type thermocouples were placed at the entrance and exit of the micro-channel heat sink to measure the inlet and outlet liquid coolant temperature as shown in Fig. 5.17. The inlet and outlet thermocouples were connected to Omega DPi32 thermocouple indicators (Fig. 5.16). Six J-type thermocouples were placed into the holes drilled into the copper test heater to measure the temperature distribution in the test heater (Fig. 5.11). The six J-Type thermocouples were connected to the PC based Data Acquisition Unit (DAU) for measurements.

A differential pressure gauge, Honeywell model, KZ 5 psid, was used to measure the pressure drop across the micro-channel heat sink and a Honeywell model Z, 25 psia, to measure the absolute pressure at the heat sink outlet. The pressure transducers were connected to Honeywell model GM indicators and also to the PC based Data Acquisition Unit (DAU). Figure 5.18 shows the instruments for pressure drop and outlet pressure measurements

A PC based Data Acquisition Unit (DAU) was developed to automatically record temperature and pressure data during testing. The PC based Data Acquisition Unit used an Agilent 34970A connected to a PC. The LabVIEW software was used to create a VI to record the temperatures in the test heater and the pressure drop as well as absolute outlet pressure in the heat sink. Figure 5.19 shows the PC based Data Acquisition Unit and Figure 5.20 shows the user interface for the virtual instrument.

Figure 5.16: Thermocouple indicators for the pump discharge water temperature, inlet and exit water/coolant temperature.

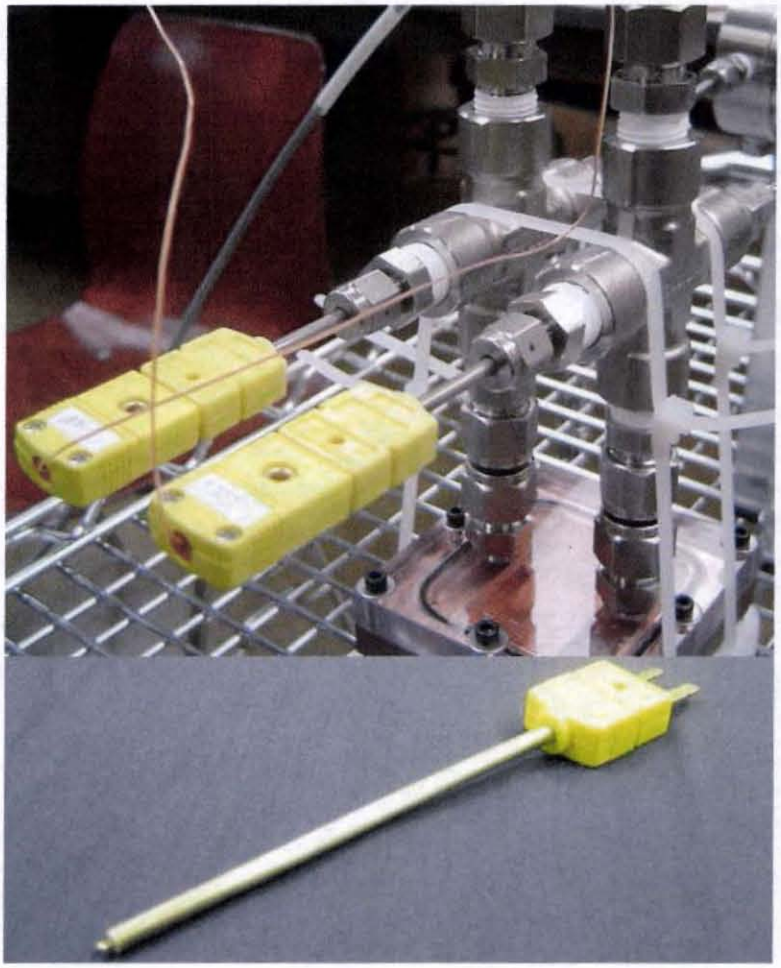

Figure 5.17: Type K thermocouples used to measure temperatures in the flow system.

Figure 5.18: The pressure measurement system including the absolute and differential pressure transducers and the indicators

Figure 5.19: Agilent 34970A data acquisition unit

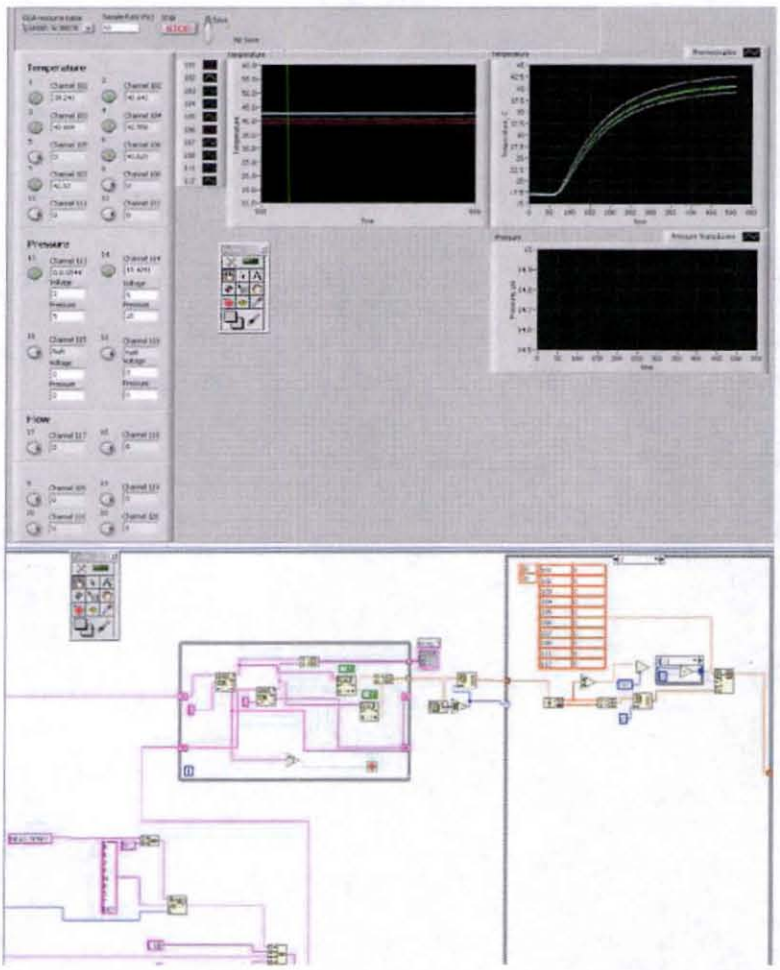

Figure 5.20: Screen shot example of the LabVEIW program developed for data acquisition

5.3.4 Construction

The flow loop adjusts the liquid coolant, DI water in this project, to its desired operating conditions and supplies it to the micro-channel heat sink. The flow loop consisted of a 1-gallon Alloy Products Corp water reservoir, a Cole-Parmer 75211-10 variable speed gear pump, two SWEP B5H×10 compact brazed heat exchangers, a 40 μm filter. The flow loop was mounted on a cart. The flow loop interfaced with the refrigeration bath, the NESLAB RTE7, which was modified by adding caster wheels to make it mobile.

Two rotameters were used to measure liquid coolant flow rate: FL-3839-G and a FL-3839-ST 150 mm flow meters. A two bar pressure gauge was employed to monitor the pump outlet pressure. Figure 5.24 shows the rotameters and Figure 5.25 pressure gauge.

The assembled flow loop cart with the refrigerated bath is shown below. The front of the flow loop cart has the instrument panel that includes the pressure gauge to measure the pump pressure, the two flow meters to measure the flow rate, and three temperature indicators to show the temperature of the flow loop water as well as the heat sink inlet water temperature and the heat sink exit water temperature. The back of the flow loop has the fittings to connect the flexible hoses that lead to the refrigerated bath and to the heat sink. The back panel also has three valves to shut of the water going out of the cart and to bypass those lines so that the water will only flow within the cart. This allows an easy attachment and removal of the heat sink to and from the cart.

Figure 5.21: Water reservoir

Figure 5.22: Pump

Figure 5.23: Compact brazed heat exchangers

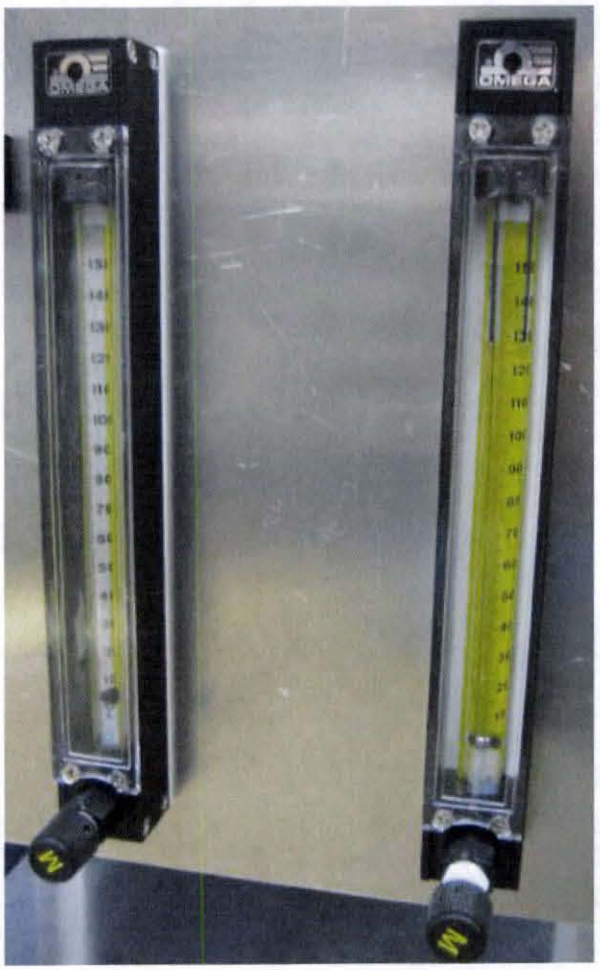

Figure 5.24: Rotameters for flow measurements

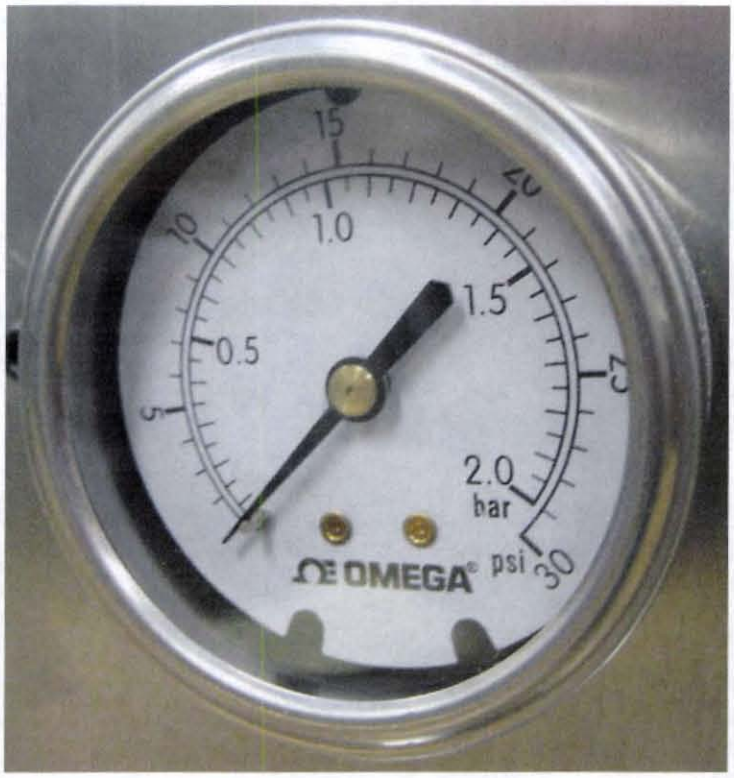

Figure 5.25: Pressure gauge to monitor pump outlet pressure

Figure 5.26: Refrigeration bath

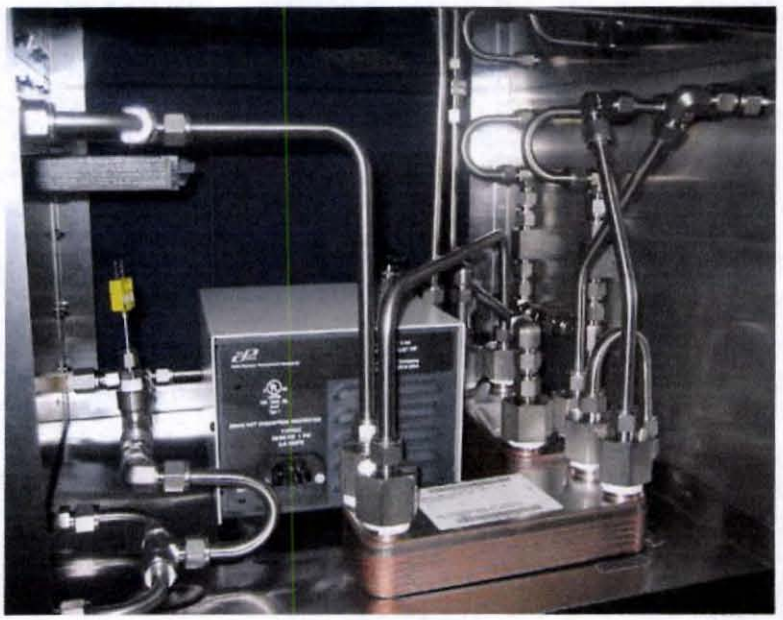

Figure 5.27: Internal look at the flow loop cart

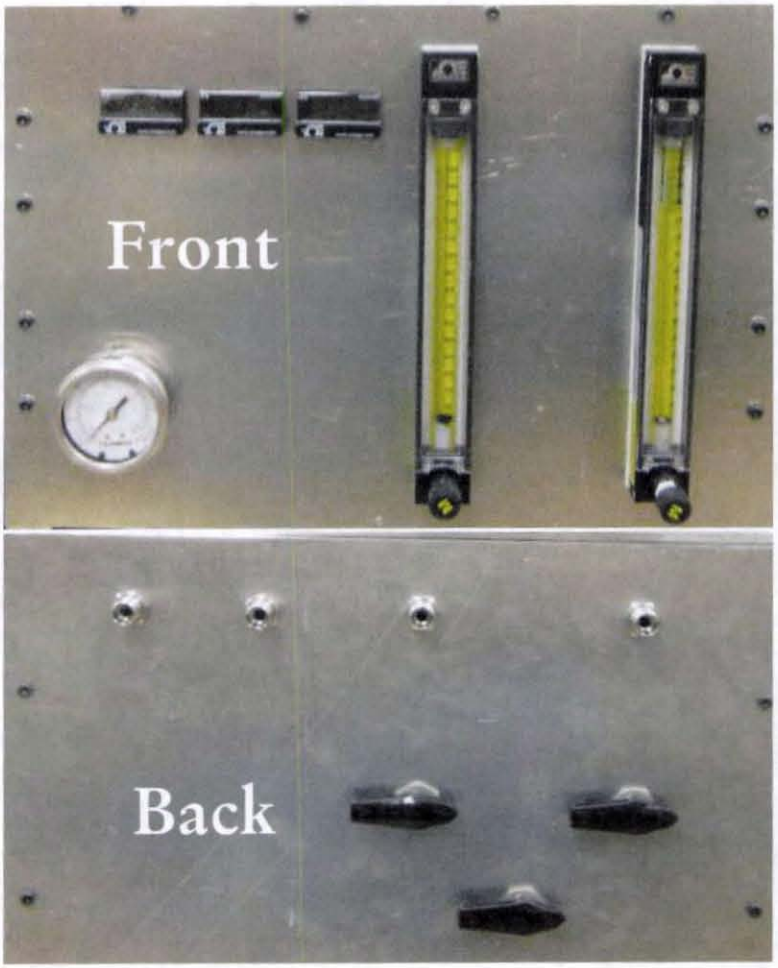

Figure 5.28: Front and back panels of the flow loop cart.

Figure 5.29: Flow loop cart.

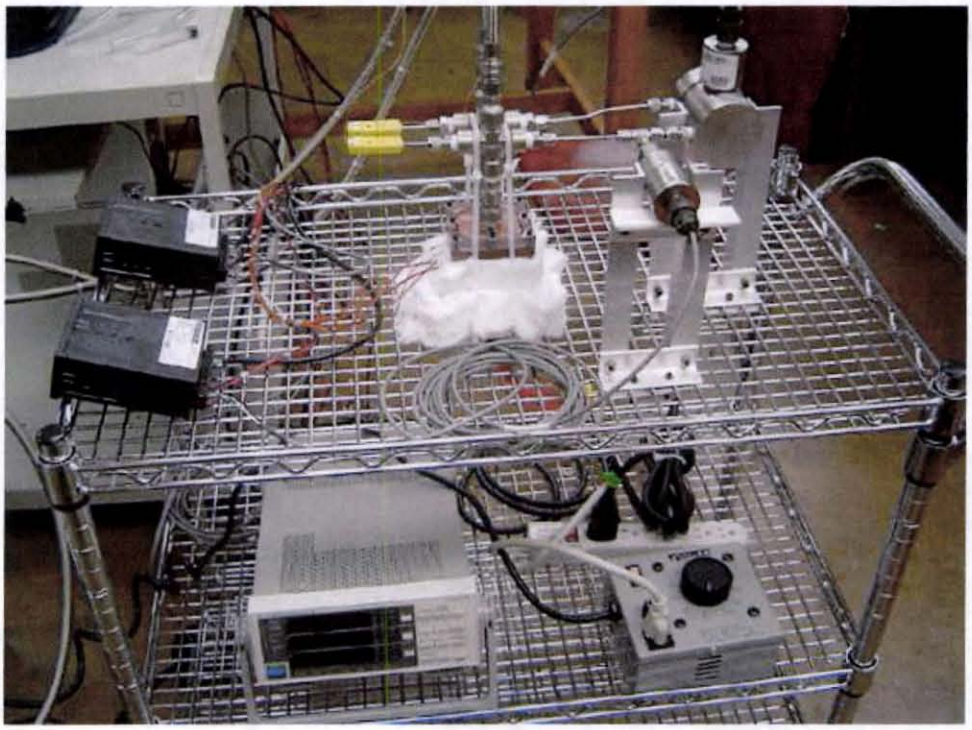

Figure 5.30: Test cart

Figure 5.31: Heat sink testing system including testing cart, flow loop cart, and refrigeration bath.

5.4 Results and Discussion

5.4.1 Experimental Error

The thermocouples in the test heater had an accuracy of 0.75%. The heater temperature data was obtained by the use of the data acquisition unit. The error associated with the data acquisition unit is 0.03°C. The system was allowed to reach steady state and then data was collected for approximately one minute at 5 samples per second. The temperature readings were averaged and the standard deviation was calculated for use in reading precision errors.

The thermocouples measuring the coolant inlet and outlet temperatures had an accuracy of 0.4%. The coolant inlet and outlet temperatures were read from the temperature indicator which had a resolution of 0.1 °C. Coolant inlet and outlet temperatures were recorded at steady state at the beginning of the data collection for each flow rate.

The pressure transducers had an accuracy of 0.25% of the full scale. Pressure data was obtained at the same time and in the same manner as the heater temperatures. The error associated with the data acquisition unit is 0.0002% of the reading + 0.0001% of the range. The pressure readings were averaged and the standard deviation was calculated for use in reading precision errors.

5.4.2 Experimental Results

Figure 5.32 shows the experimental results for a power level of 80 W and a flow rate of 200 ml/min and compares them to the predictions of the 2D model. In the 2D modeling the substrate and heater were considered continuous and did not include any interface resistance, which most likely accounts for the difference between the experimental data. The value of the resistance due to the interfacial contact was estimated by the difference in temperature and included in Figure 5.33. The contact resistance of the interface was found to be about $2.16\times10^{-4}\frac{m^2°C}{W}$. The 2D modeling was performed in the heat sink substrate and a 1D heat conduction was assumed to calculate the temperatures in the test heater. The estimated contact resistance value was applied to other testing conditions. Figure 5.34

Table 5.1: Heat sink geometrical parameters

Flowrate (ml/min)	Power (W)	Voltage (V)	Current (A)	HS Inlet Water Temp (°C)	HS Outlet Water Temp (°C)
102	81.20	82.78	0.981	24.9 ±0.11	35.1 ±0.15
151	80.87	82.62	0.9785	25.0 ±0.11	32.3 ±0.14
199	80.81	82.60	0.9875	25.0 ±0.11	30.3 ±0.13
250	80.30	82.37	0.976	25.0 ±0.11	29.2 ±0.13
299	80.30	82.34	0.9749	25.0 ±0.11	28.6 ±0.12
102	—	—	—	—	—
151	101.19	92.46	1.0944	25.1 ±0.11	34.3 ±0.15
199	101.21	92.48	1.0944	25.1 ±0.11	31.8 ±0.14
250	101.57	92.62	1.0962	25.1 ±0.11	30.5 ±0.13
299	101.42	92.57	1.0958	25.1 ±0.11	29.6 ±0.13

shows the experimental results for a power level of 100 W and a flow rate of 200 ml/min. The good agreement between the experimental data and the model prediction verified that the contact resistance at the interface is approximately that value that was calculated. Figure 5.35 shows the variation in temperature of the thermocouple placed closest to the channel outlet with the coolant flow rate and Figure 5.36 shows the variation in the pressure drop across the heat sink with the coolant flow rate. All the temperatures fall below the maximum allowable temperature of 65 °C. The pressure drop across the heat sink is small and is lower than the projected value in the initial design (Fig. 5.7). This is most likely due to the actual viscosity of the water varying with the temperature.

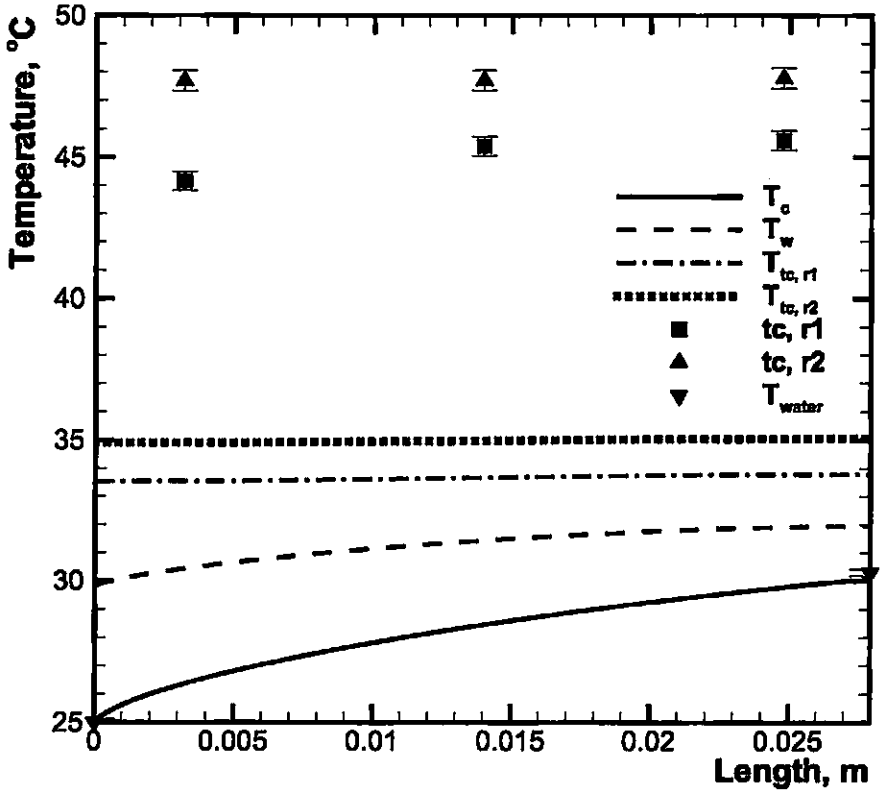

Figure 5.32: Single-phase heat sink thermal performance results for 80 W with a coolant flow rate of 200 ml/min. The difference between the numerical prediction and experimental values are due to an interfacial resistance between the test heater and the heat sink.

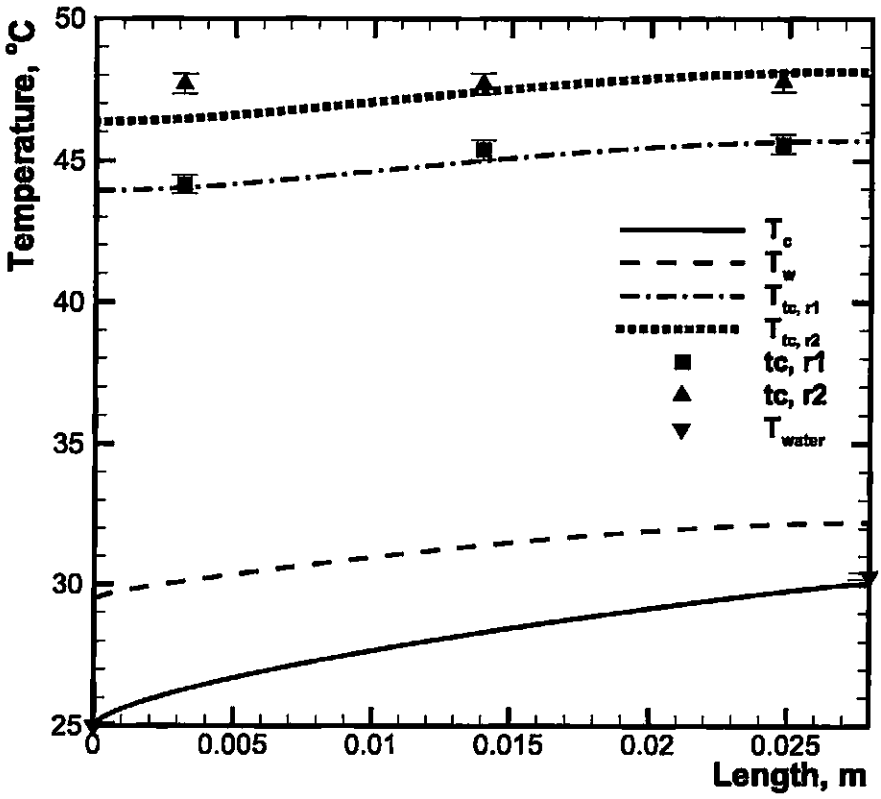

Figure 5.33: Single-phase heat sink thermal performance results for 80 W with a coolant flow rate of 200 ml/min. By adding the resistance of the interface the numerical predictions match the experimental values better.

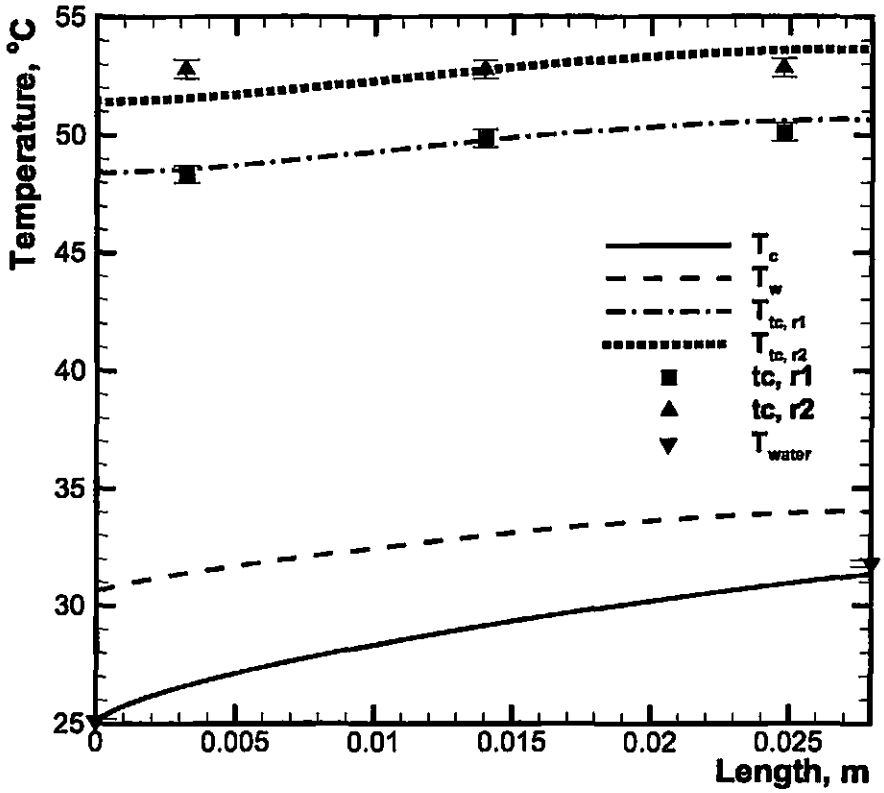

Figure 5.34: Single-phase heat sink thermal performance results for 100 W with a coolant flow rate of 200 ml/min using the thermal resistance calculated from the best fit for 80 W at 200 ml/min.

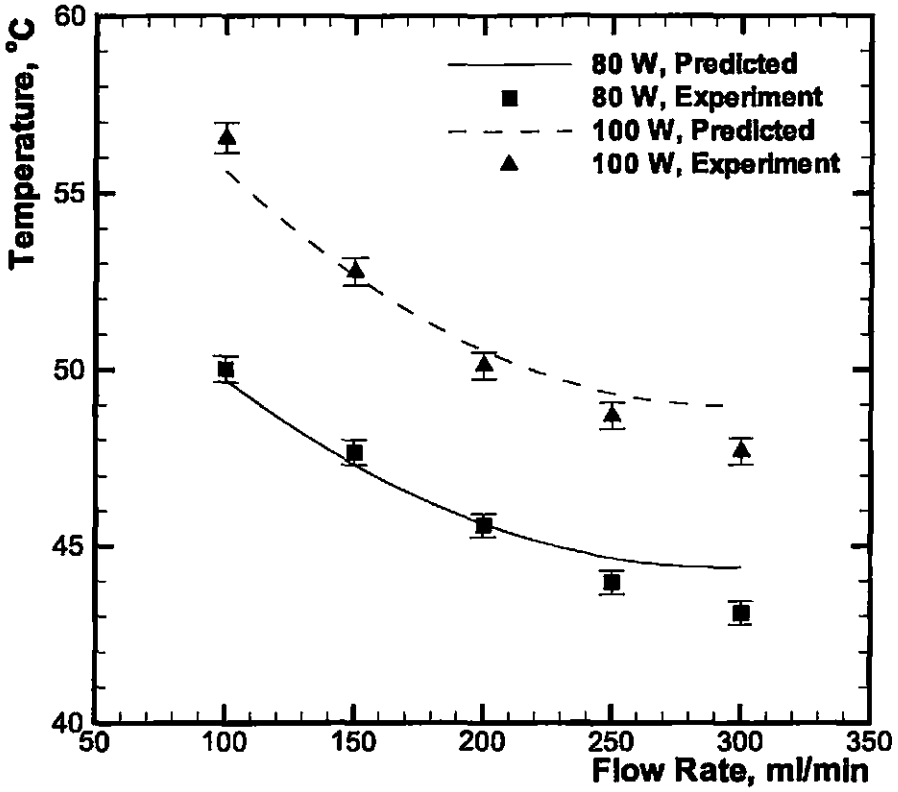

Figure 5.35: Temperature variation with coolant flow rate for the thermocouple closest to the channel outlet.

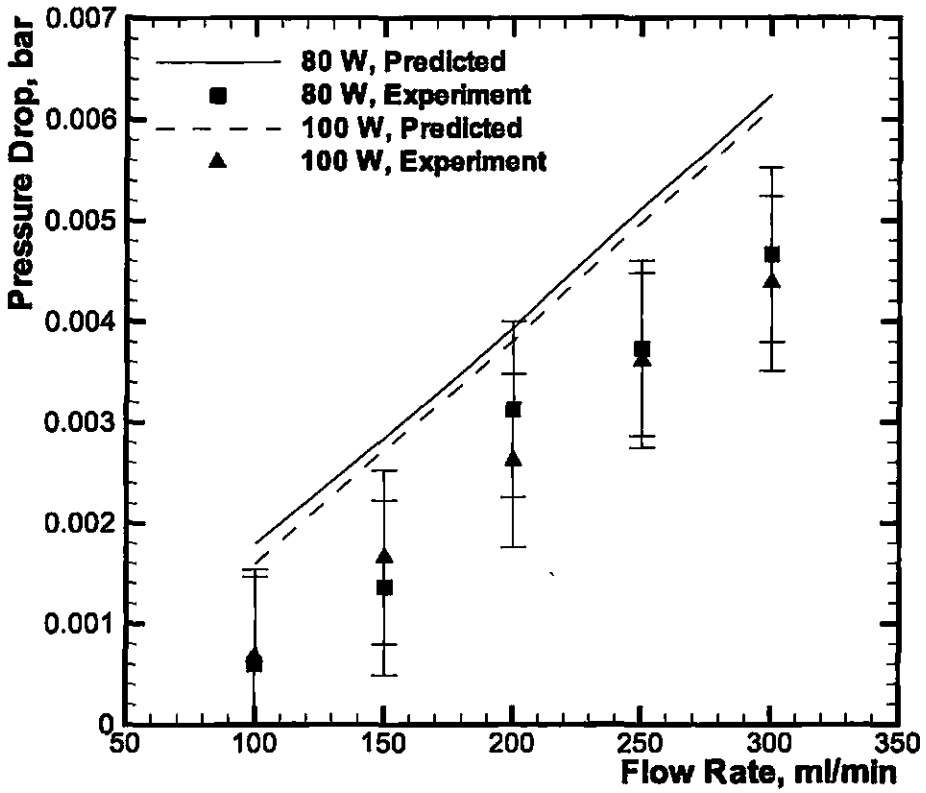

Figure 5.36: Single-phase heat sink hydraulic performance. Pressure drop across the heat sink for various flow rates.

5.5 Summary

A single-phase micro-channel heat sink was successfully designed and tested for the cooling of a high-power radar amplifier. The temperature within the test heater was well below the 65 °C limit for the amplifier even with an increased heat load of 100 W. This shows that micro-channels can be used to effectively dissipate waste heat from high power electronics. The thermal design procedure developed in chapter 4 was used in the initial design of the enhanced heat transfer surface to determine appropriate micro-channel dimensions. A small problem did arise with the unknown contact resistance between the test heater and the heat sink. The use of the 2D analysis developed in chapter 3 allowed adjustments to be made to calculate the temperature where the thermocouples were located.

Chapter 6

Design of a FC-72 Cooled Two-Phase Heat Sink

The primary objective is to develop a FC-72 cooled two-phase micro-channel heat sink experimental system that consists of a heat sink test module, a flow loop, and instrumentations. The testing system is to be used to explore thermal performance of a novel type of two-phase micro-channel heat sink. This includes design and fabrication of a two-phase micro-channel heat sink module, design and construction of a flow loop and instrumentations, and assembly of the testing system.

6.1 Design Parameters

6.1.1 Geometrical Parameters

The length, L, and width, W, of the heat sink will be set to 15.0 mm by 15.0 mm. Cover plate of the heat sink will be made from a transparent polycarbonate plastic Lexan to allow direct visual access to the flow boiling in micro-channels. The cover plate will not affect the performance of the heat sink, as its thermal conductivity is much lower than that of the copper heat sink. The thickness of the cover plate H_c is set to be 0.5 inch.

Key objective of the thermal design of the micro-channel heat sink is to determine micro-channel dimensions (W_{ch} , H_{ch} , and W_w). Deeper micro-channels always produce better heat sink performance. H_{ch} should therefore be made as large as possible. However, there is always a practical maximum value for H_{ch} that is set by machining and/or structural limitations. For the present design, H_{ch} is set to be 600 μm. Selection of (W_{ch} and W_w

) was achieved by applying best available empirical correlations to different combinations and observing the trend in performance. For this project, the combination is selected to be (100 μm and 100 μm).

6.1.2 Operating Parameters

The operating parameters are summarized below.

- The heat sink material that will be used will be oxygen free copper.
- The coolant will be Fluorinert FC-72.
- The target total power to be dissipated by the two-phase micro-channel heat sink test module will be about 225 W, which is 100 W/cm^2 in terms of the effective input heat flux.
- The inlet temperature will be 25 °C, corresponding to normal room temperature.
- The outlet pressure will be about 1.1 bar, which is slightly higher than the ambient atmospheric pressure.

Coolant flow rate will be within the range of 60 to 210 ml/min. Figure 6.1 shows the variations of $Q_{t,tpmax}$ and $Qt, tpmin$ with effective input heat flux q''_{eff} . Two-phase maximum flow rate $Q_{t,tpmax}$ is the highest flow rate that can sustain saturated flow boiling in the micro-channels for a given q''_{eff}. It represents the total coolant flow rate that causes saturated flow boiling to first occur at the channel outlet. $Q_{t,tpmax}$ is set equal to the coolant flow rate value corresponding to zero thermodynamic equilibrium quality at the channel outlet, $x_{e,out}$=0 . Two-phase minimum flow rate $Q_{t,tpmin}$ is the lowest flow rate that can still sustain effective cooling by saturated flow boiling in the micro-channels for a given heat flux q''_{eff}. It represents the coolant flow rate that causes complete evaporation of FC-72 coolant. $Q_{t,tpmin}$ is set equal to the coolant flow rate value corresponding to unit thermodynamic equilibrium quality at the channel outlet, $x_{e,out}$=1.The two-phase micro-channel heat sink flow rate has to be within the region defined by the two lines. For the

present project, several flow rates in the range corresponding to 100 W/cm^2 of the effective input heat flux (60–210 ml/min) should be tested.

6.1.3 Thermal Fluid Parameters

Two-phase pressure drop and heat transfer correlations that will be used as design equations for the present micro-channel heat sink test module come from two journal papers by Jaeseon Lee and Issam Mudawar ([41] and [42]).

The thermal/fluid parameters indicate the micro-channel heat sink performance, which include maximum heat sink temperature and pressure drop. Four (W_{ch}, W_w) combinations (100×100, 200×200, 300×300, 400×400 μm) are examined for q''_{eff}= 100 W/cm^2 . Figures 6.2 to 6.5 show the variations of highest heat sink temperature $T_{w,out}$ and total pressure drop ΔP with Q_t in two-phase region $Q_{t,tpmin} \leq Q_t \leq Q_{t,tpmax}$) for the four (W_{ch}, W_w) combinations.

It should be noted that the empirical correlations developed using liquid coolant other than FC-72 are employed for the calculation. For example, the pressure drop correlation was developed using R134a and water data, and heat transfer correlation using FC-84 and water data. Therefore, figures 4-7 only shows qualitative trend and large errors are expected. For the present project, the combination of (200 μm and 200 μm) will be used. The dataset from the experimental study will be used to assess the feasibility of the exiting correlations at predicting FC-72 performance. If necessary, new reliable correlation should be developed based the FC-72 database to facilitate the future design of FC-72 cooled two-phase micro-channel heat sink.

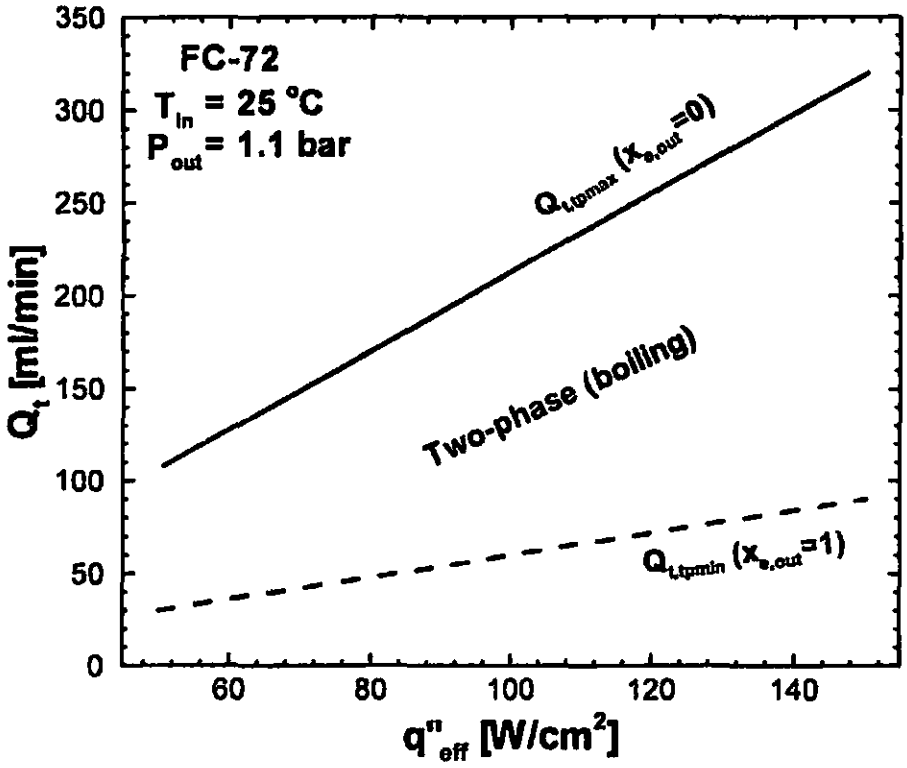

Figure 6.1: Variation of two-phase minimum flow rate and two-phase maximum flow rate with effective heat flux.

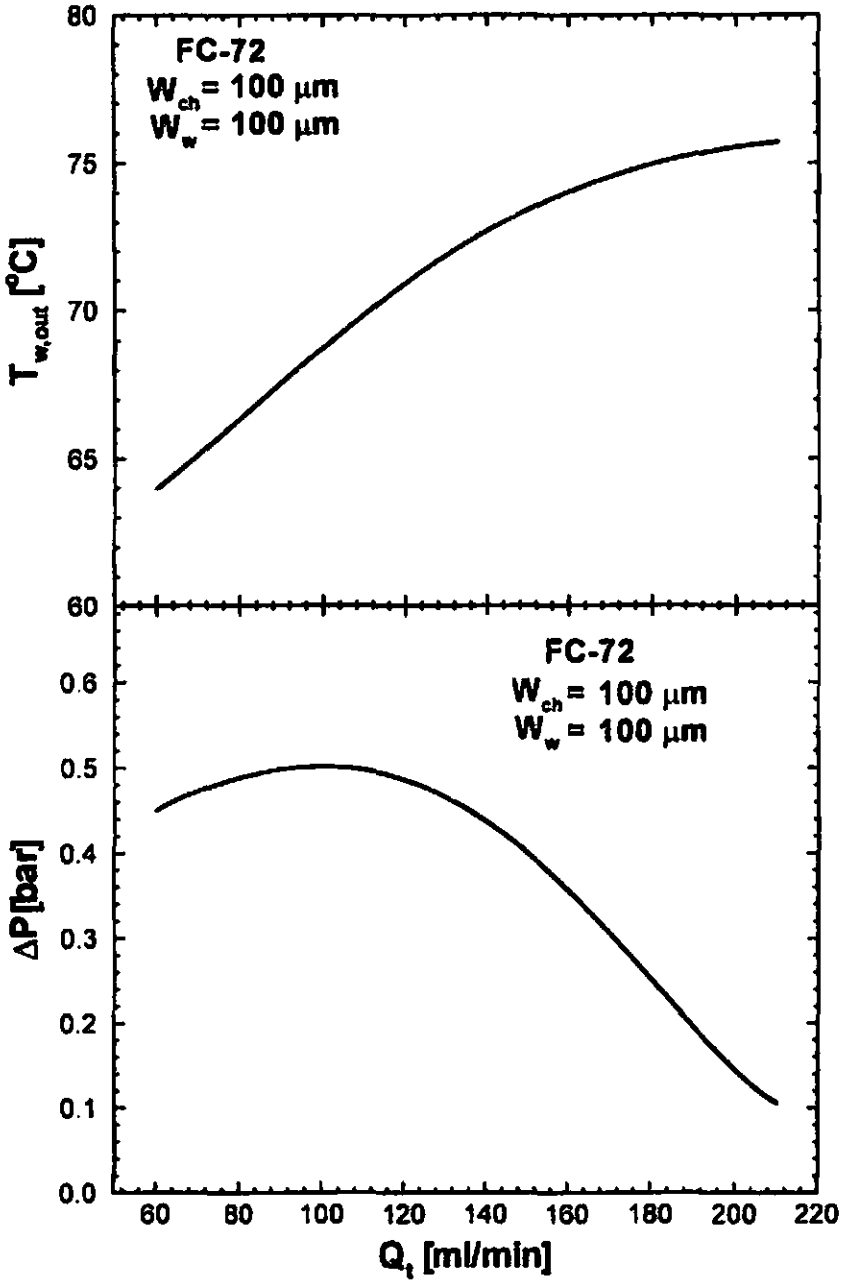

Figure 6.2: Variation of highest heat sink temperature and pressure drop for $W_{ch} = 100$ μm and $W_w = 100$ μm

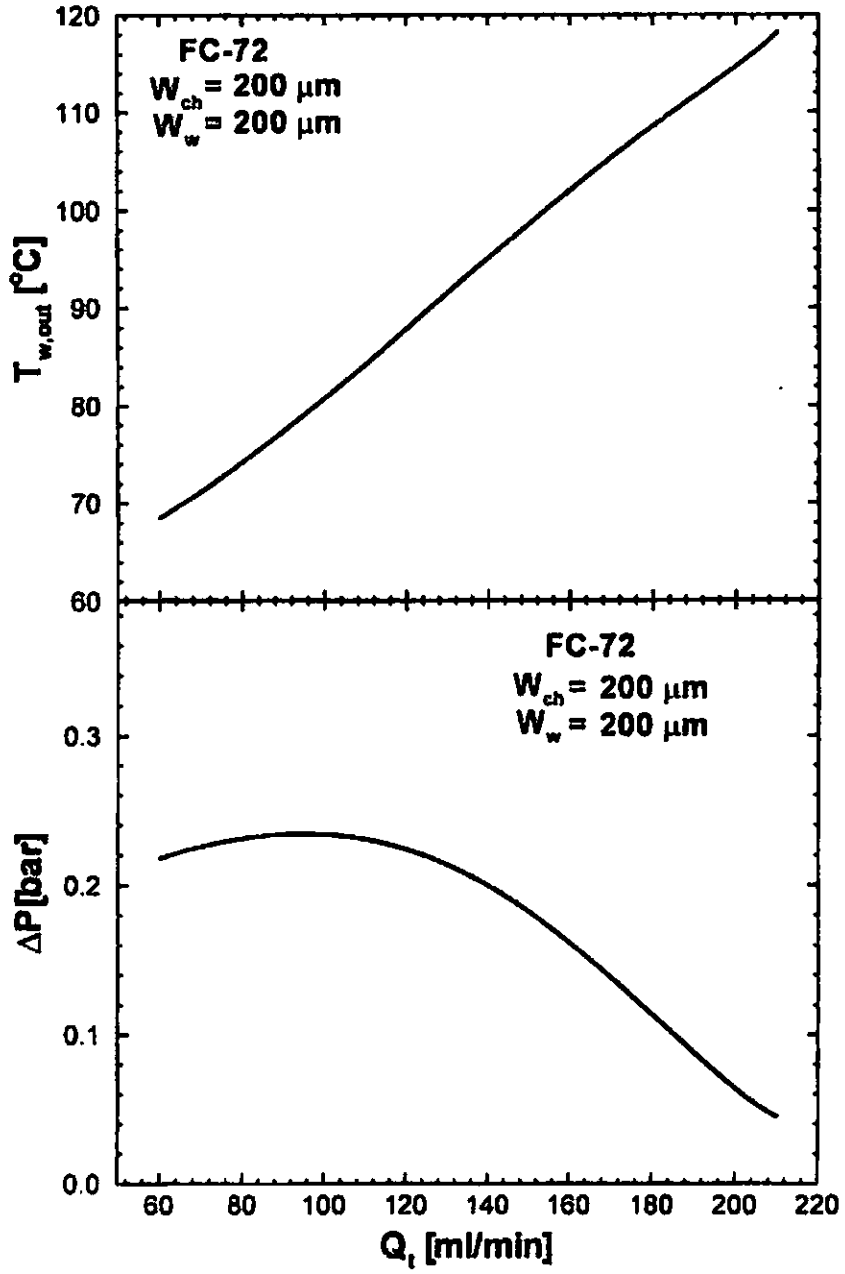

Figure 6.3: Variation of highest heat sink temperature and pressure drop for $W_{ch} = 200$ μm and $W_w = 200$ μm

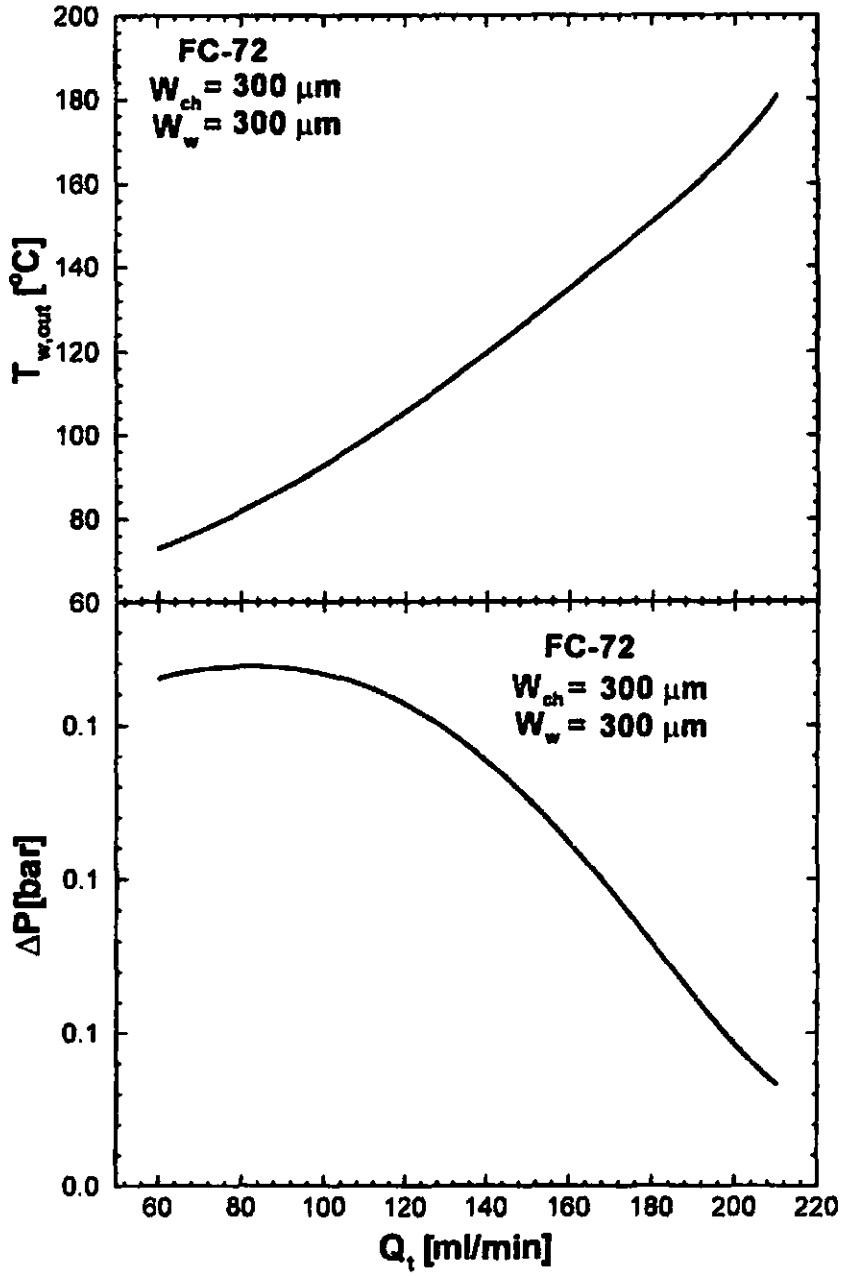

Figure 6.4: Variation of highest heat sink temperature and pressure drop for W_{ch} = 300 μm and W_w = 300 μm

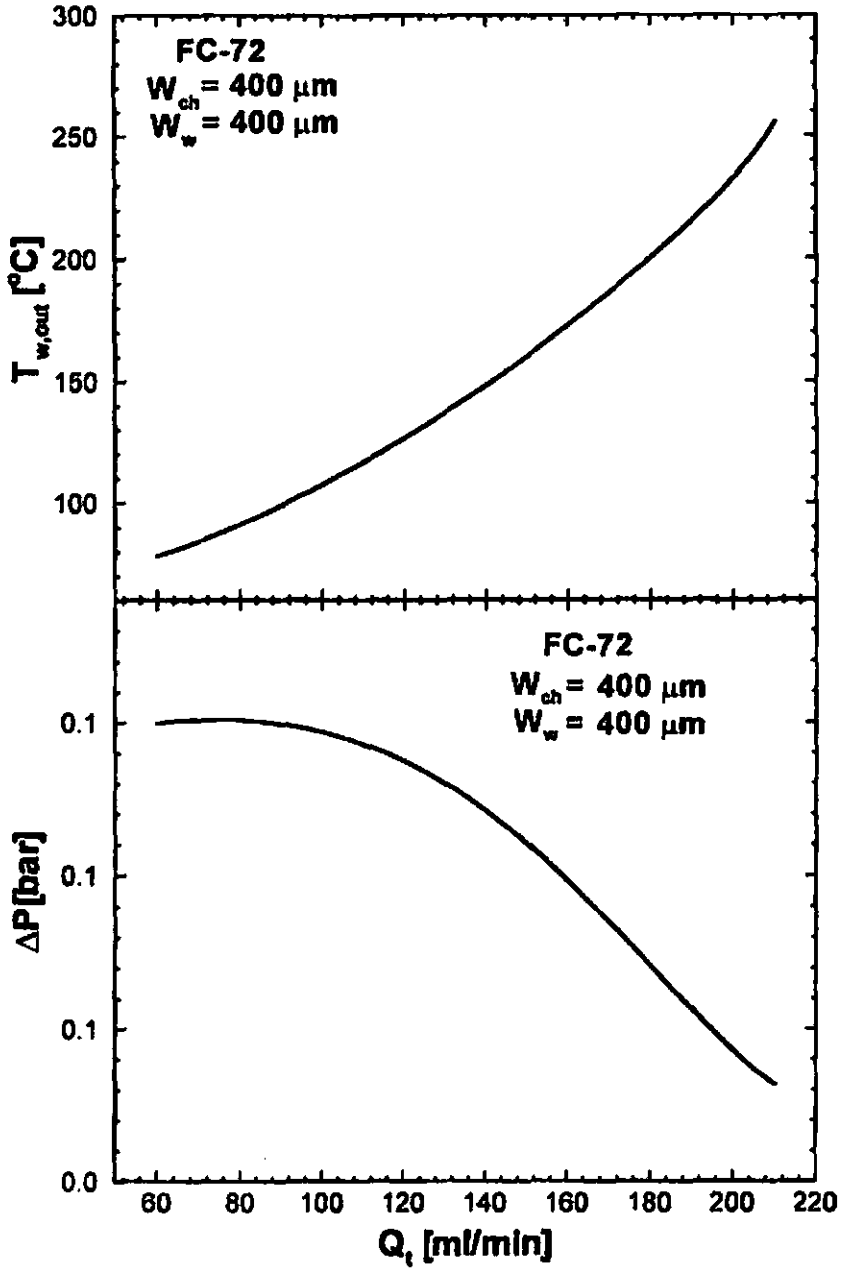

Figure 6.5: Variation of highest heat sink temperature and pressure drop for W_{ch} = 400 μm and W_w = 400 μm

6.2 Experimental Design

6.2.1 Fluid Properties

Saturated thermophysical properties of the FC-72 liquid and vapor are needed when perform thermal design using the above correlations. A table of saturated properties of the FC-72 liquid and vapor was obtained from the 3M Electronics Markets Materials Division. The important properties that vary with temperature are plotted in Figures 6.6–6.9. To use the data conveniently in a computer program based design scheme, a curve fit was done within a working region from 20 to 80 °C.

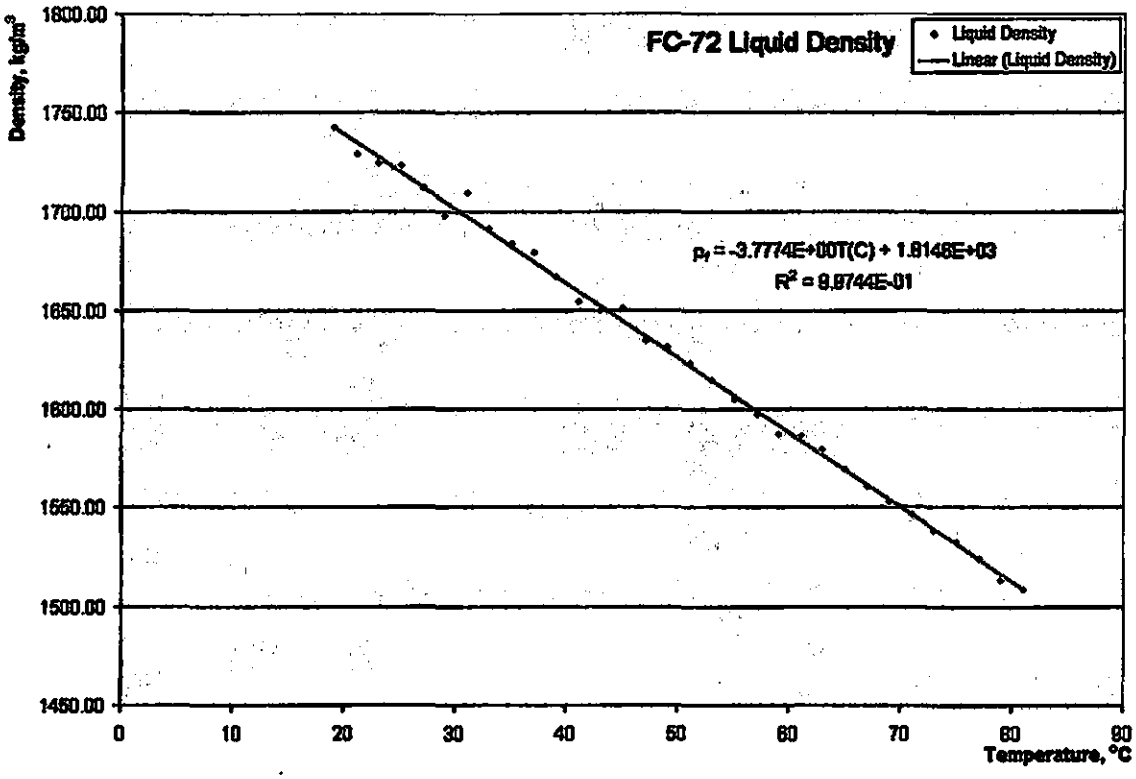

Figure 6.6: Best-fit equation for FC-72 saturated liquid density versus temperature from 20 °C to 80 °C

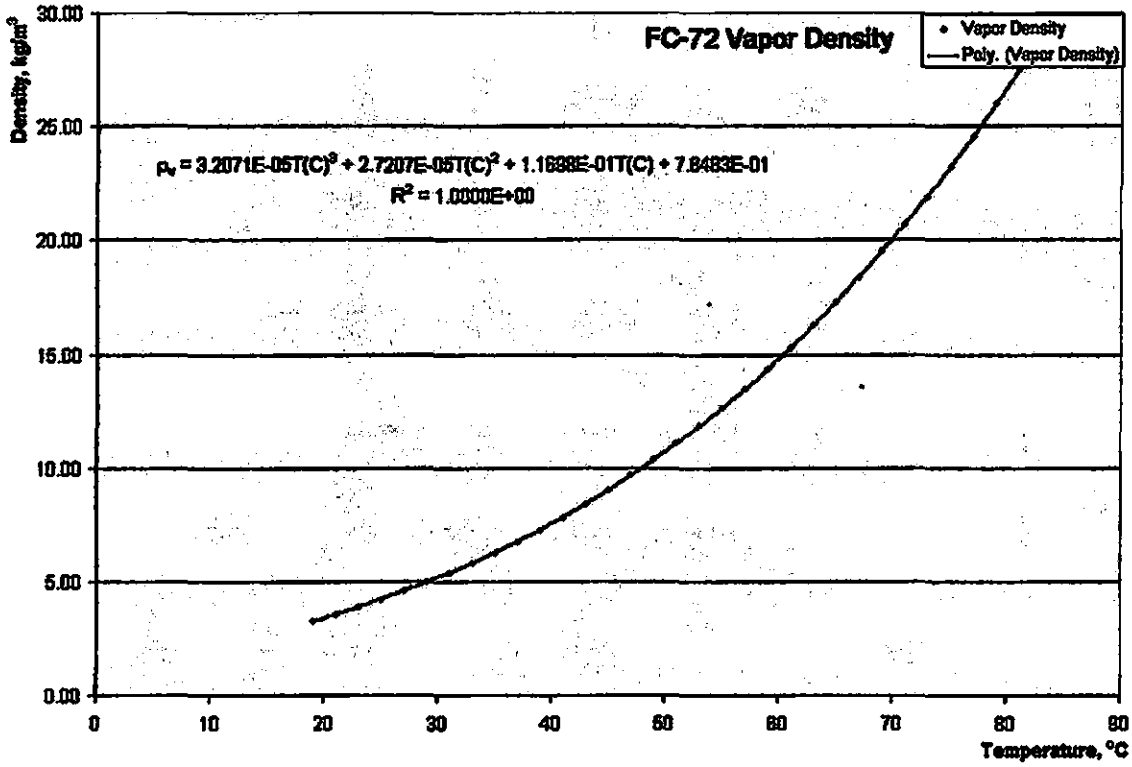

Figure 6.7: Best-fit equation for FC-72 saturated vapor density versus temperature from 20 °C to 80 °C.

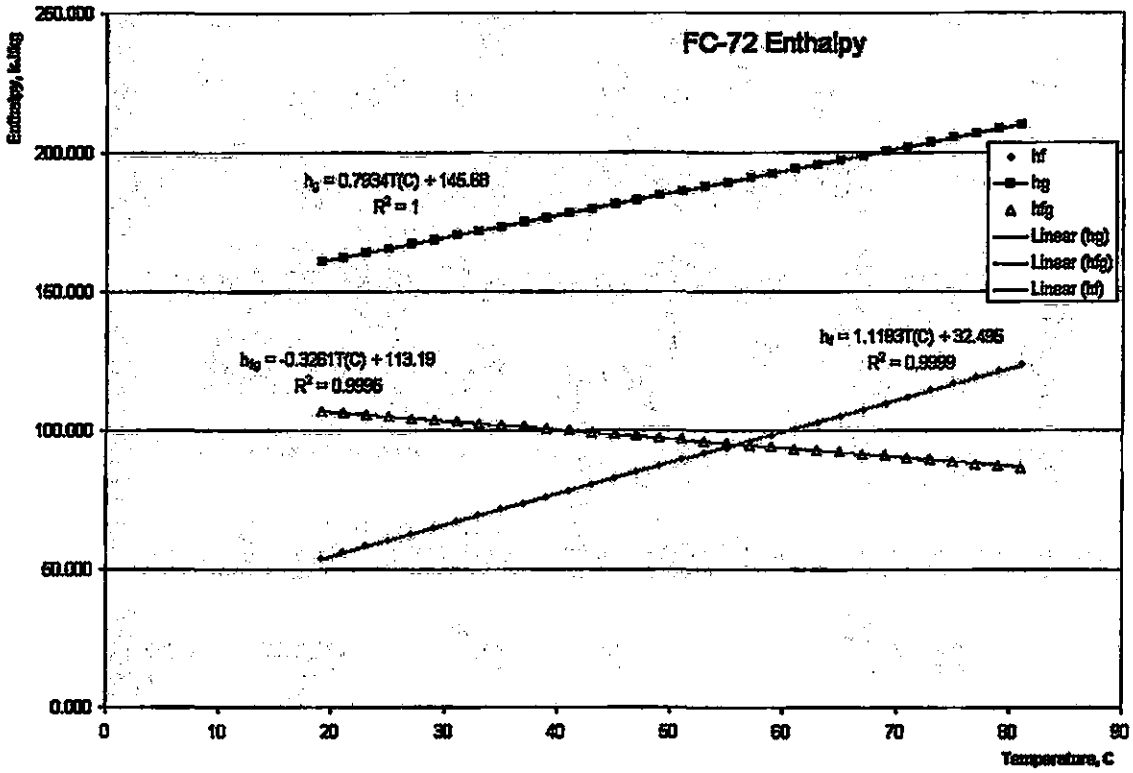

Figure 6.8: Best-fit equation for FC-72 saturated enthalpy versus temperature from 20 °C to 80 °C.

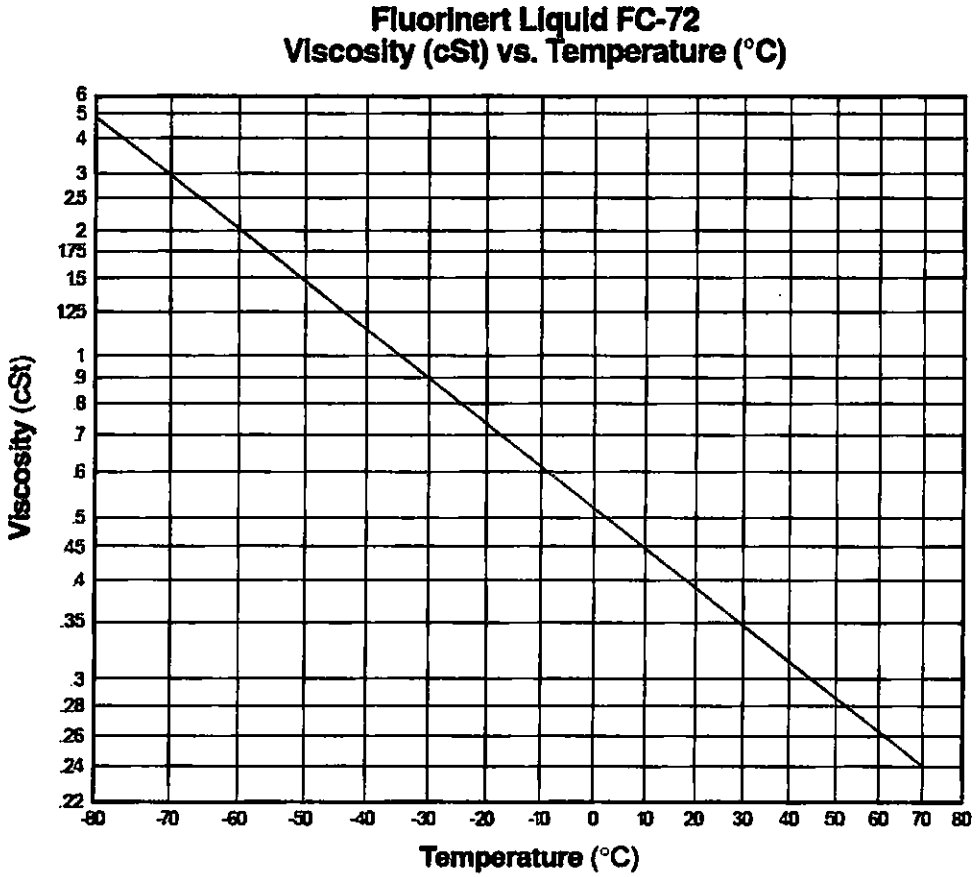

Figure 6.9: FC-72 saturated liquid viscosity data versus temperature.

The viscosity data as a function of temperature was not provided on the table obtained from 3M. A graph for the liquid viscosity was provided and an approximation for the vapor viscosity based on a CFC-113 that has a similar vapor density.

FC-72 saturated liquid viscosity can be evaluated from

$$\mu_g = 10^{-6}(-2.638 \times 10^{-4}T^2 + 7.0786 \times 10^{-2}T + 7.7884) \tag{6.1}$$

The fluid thermal conductivity is given by

$$k_f = 0.060 - 0.00011T \tag{6.2}$$

Similarly, the vapor thermal conductivity is given as an approximation from the CFC-113.

$$k_g = 3.761 \times 10^{-8}T^2 + 4.4786 \times 10^{-5}T + 7.428 \times 10^{-3} \tag{6.3}$$

6.2.2 Test Section Design

Heater

The micro-channel heat-sink test section will be a single copper piece, incorporating the both the enhanced micro-channel surface and the simulated electronic device. Four holes will be made in the base of the test section to allow for the cartridge heaters to be inserted in to the test section. The cartridge heaters will be 1/8 inch in diameter and will be one inch long and capable of producing up to 120 W each (maximum 480 W total).

Temperature measurements in the test section will be made at three positions along the flow direction and with three rows of thermocouples. The additional rows of thermocouples will allow the heat flux to be calculated.

A thin layer of material will be removed from the test section where the thermocouples will be located. This will allow for a copper shim to be placed over the thermocouples,

making a smooth surface for sealing the test section into the housing. Grooves will also be cut into the test section to allow the thermocouples to be routed down the face and out of the test section assembly without interfering with the sealing of the housing.

Housing

The design of the housing includes two ports for measuring the temperature of the coolant at the inlet and exit of the test section as well as two ports for measuring the pressure drop across the test section. The housing will be made of G-7 fiberglass.

Assembly

Figure 6.14 shows the heat sink test section assembly including the test section, housing, cover plate, insulation, and ceramic and aluminum base plates.

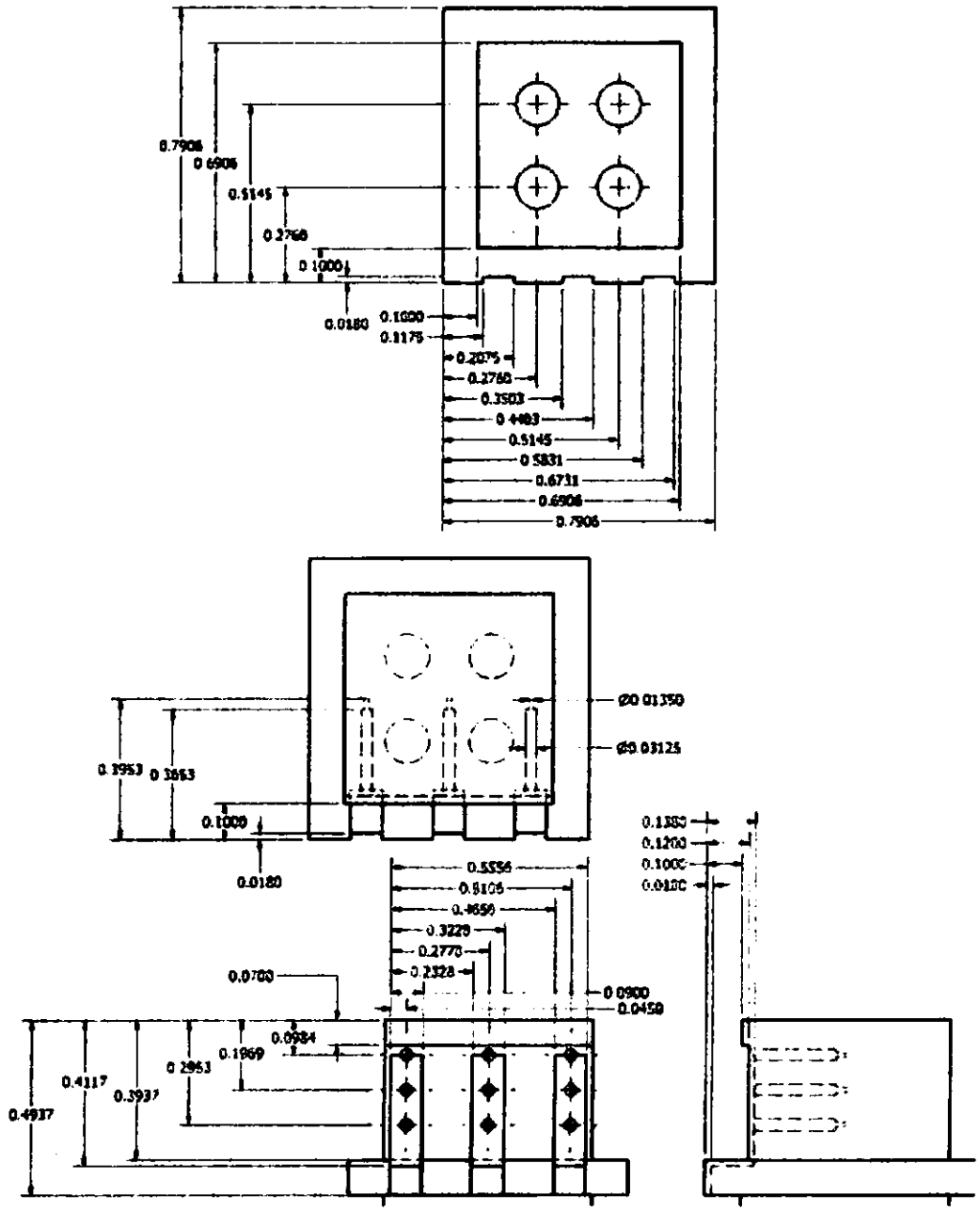

Figure 6.10: Drawings of the two-phase heat sink test section.

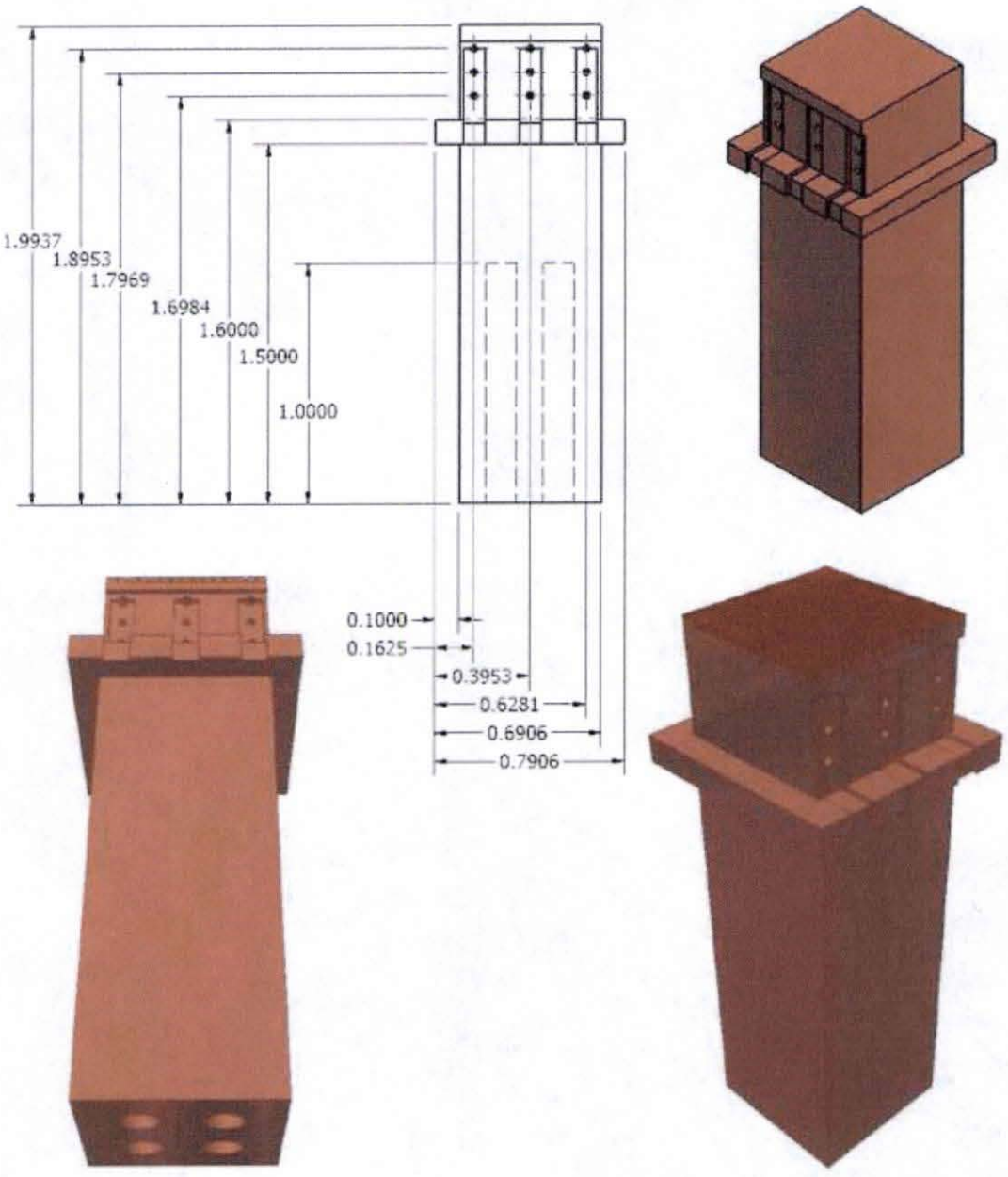

Figure 6.11: Solid model and drawings of the two-phase heat sink test section.

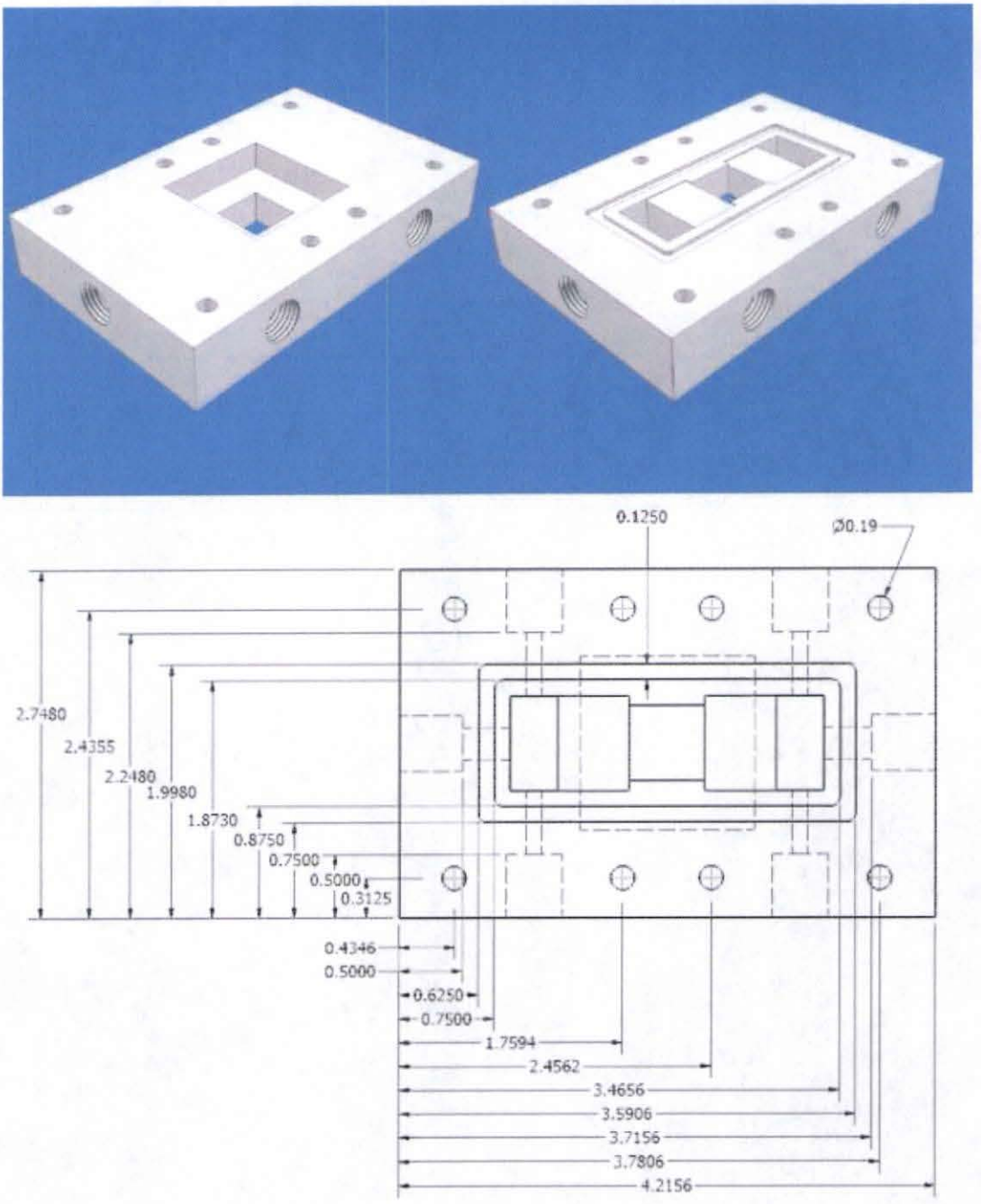

Figure 6.12: Solid model and drawings of the two-phase heat sink housing.

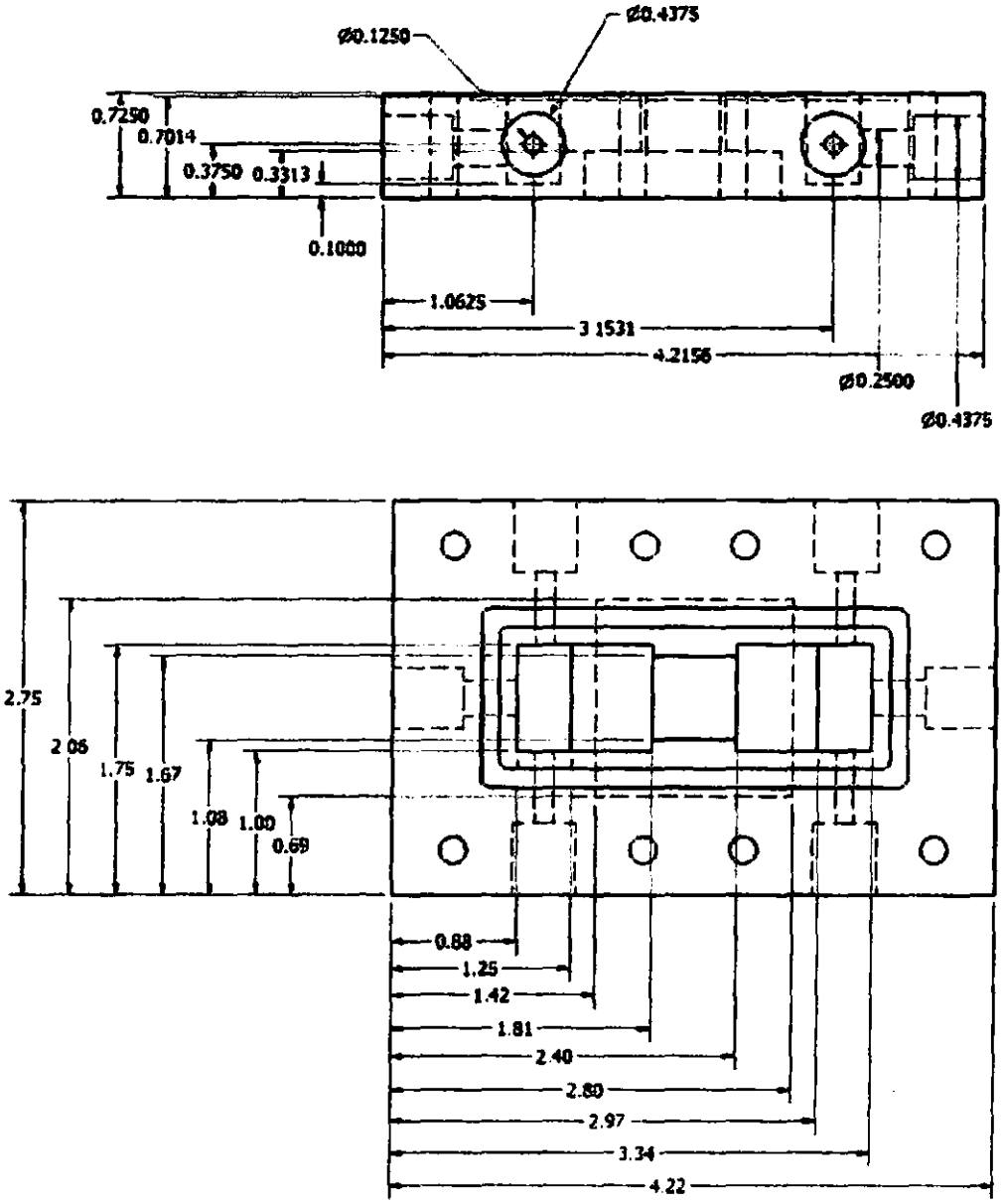

Figure 6.13: Drawings the two-phase heat sink housing.

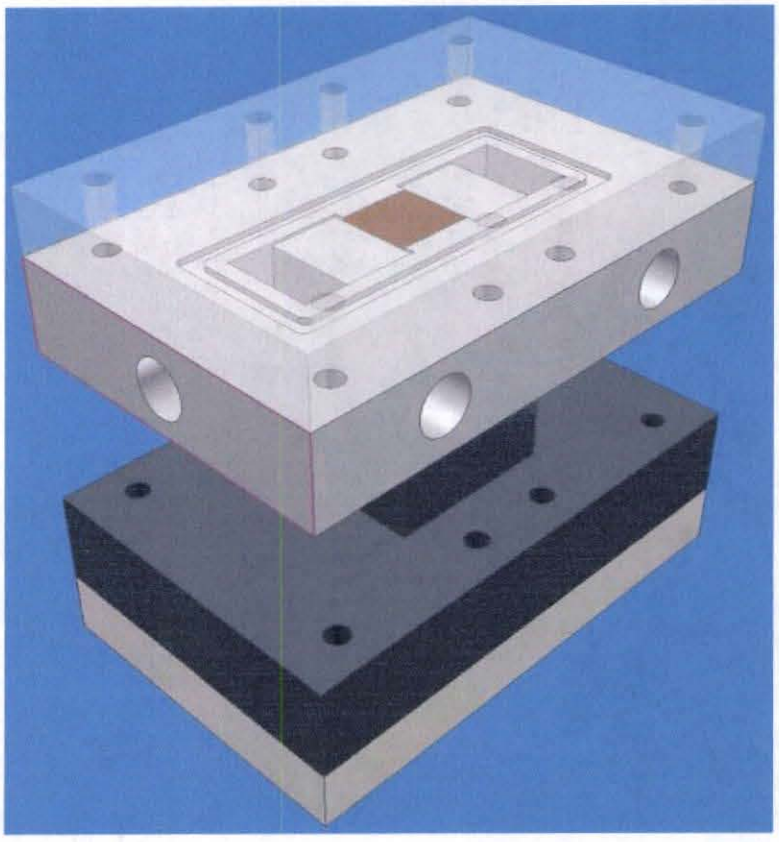

Figure 6.14: Solid model of the two-phase heat sink test section assembly

6.2.3 Flowloop Design

6.2.4 Pump

Micropump was contacted to size a pump for this application. A flow rate of 40-220 ml/min, a viscosity of 0.64 centipose, and a ΔP of at least 0.5 bar was given to Micropump for sizing. Micropump recommended a model GA-T23 suction shoe style magnetic drive gear pump. The pump had has a working viscosity range of 0.2 to 1500 cp, a maximum differential pressure of 5.2 bar, and is capable of a flow rate around 400 ml/min at 5,000 rpm.

A Micropump suction shoe style pump head and modular pump drive with analog remote control was ordered from Cole-Parmer. The modular pump drive was selected so that control of the pump could be handled from the instrumentation cart instead of the flow loop cart. The maximum rpm of the pump drive was 3,600 rpm and so a pump head with a higher flow rate range was needed. Model 73004-00 has the same working viscosity range, a maximum differential pressure of 8.6 bar, and is capable of a flow rate around 900 ml/min at 3450 rpm and 1305 ml/min at 5,000 rpm as the model GA-T23 Micropump head.

Reservoir Design

The purpose of the reservoir is to store and degas extra FC-72 for the flow loop system. Within the reservoir the air will be removed from the FC-72 by boiling the fluid. Air will be allowed to leave the reservoir through a vent at the top and a condensing coil will be placed inside near the top to condense back the FC-72 vapor.

The reservoir will be made of clear polycarbonate, LEXAN. This will allow for a visual monitoring of the FC-72 fluid level. The reservoir will have internal dimensions of approximately 4 x 3 x 6 inches, allowing for a total volume of 1 L, of which 750 ml will be for the fluid with space at the top for the condensing coil. The reservoir will be assembled pieces cut from a $\frac{1}{2}$ inch thick sheet. The cover of the reservoir will be held down with draw latches.

Figure 6.15: Pump drive with remote control

Fittings for ventilation and FC-72 return will be screwed in to the cover. A fitting for the FC-72 supply will be placed at the bottom of the reservoir. The fittings will accommodate 3/8" tubing that will be used for the flow loop.

A low power heater will be placed in the reservoir to boil FC-72 so that the dissolved air can be removed. The heater will be of 0.26 inch diameter with sheath length of approximately 20 inches. The maximum power of the heater will be 280 W at 240 V.

6.2.5 Instrumentation Cart

The computer stand that was ordered will be used as the instrumentation cart for the flow loop system. The power meter and data acquisition units will be placed on the top of the cart with the data acquisition computer will be on the middle shelf. An aluminum plate will be mounted such that the pressure transducer meters, variable output transformers and surge protectors can be mounted on to the cart. The pump drive remote will also be placed on this cart. The leveling screws that were shipped with the computer stand will be replaced with caster wheels to add mobility to the computer stand.

The multiplexer module was wired to accommodate 11 type K thermocouples and 2 voltage inputs for the pressure transducers. The data acquisition software (LabVIEW and Agilent) was loaded onto the data acquisition computer. The computer and the data acquisition unit (Agilent 34970A) was successfully linked and the software was tested.

6.3 Summary

A two-phase FC-72 cooled micro-channel heat sink was designed. The thermal design methodology from chapter 4 was again used in this chapter to select the micro-channel dimensions, although this time a performance map could not be completed with this fluid for the known fluid properties. The temperature and pressure drop were calculated for four different combinations of channel widths and channel wall widths. A single piece test

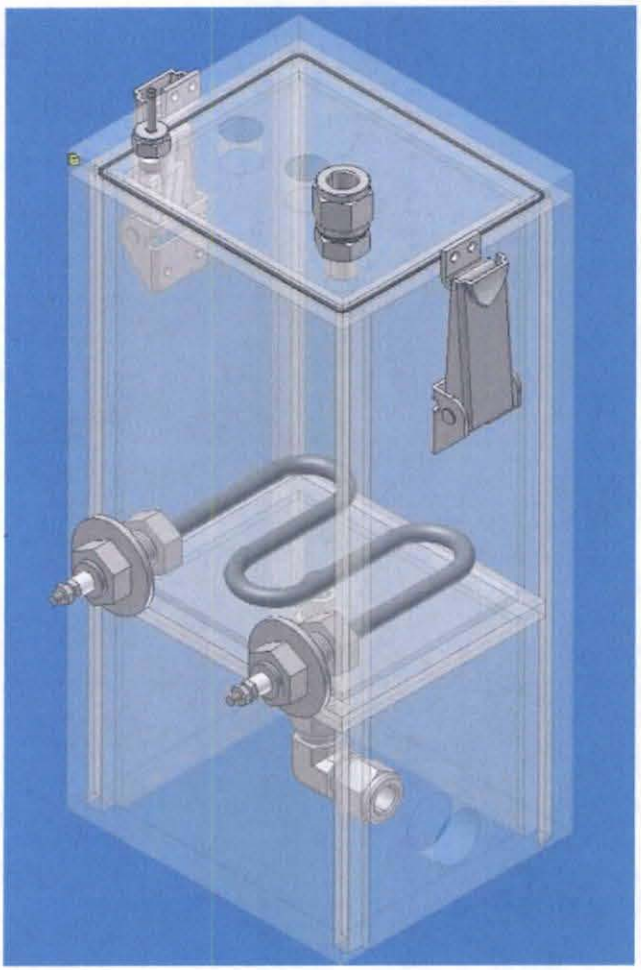

Figure 6.16: FC-72 coolant reservoir with a heater for degassing the coolant.

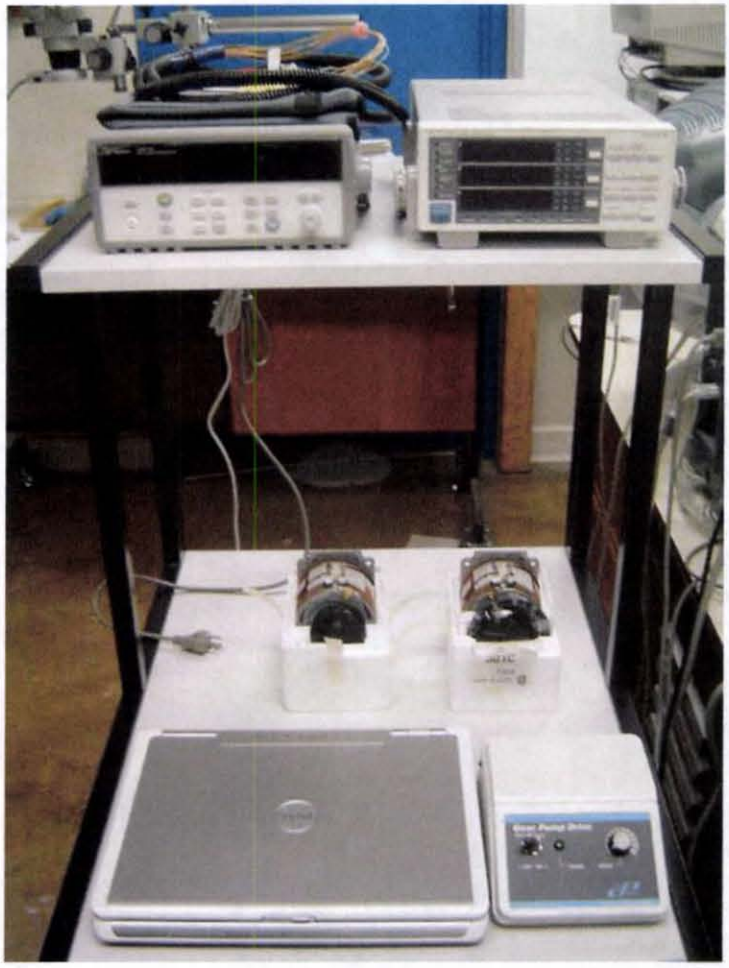

Figure 6.17: Instrumentation cart holding the data acquisition unit and computer, variable output transformers, power meter, pump control, and pressure indicators.

section was selected to avoid problems with contact resistance which was seen in the previous chapter. A completed test section was designed which included the housing and cover plate for the heat sink.

Chapter 7

Conclusions

Having a quick and effective tool for predicting the thermal performance of a micro-channel heat sink is important and valuable to design engineers. This thesis has looked at the usage of a 1D analysis as a basis for a thermal design methodology which can provide a strong starting point in the design of a micro-channel heat sink. It may be necessary to expand from the 1D analysis to incorporate the effects of axial conduction through the use of a 2D numerical modeling. It has been found that the 2D results will provide results that are close enough to a full 3D numerical analysis, [38], such that the reduction in time makes up for the small deviation in temperature for a uniform heat flux boundary condition. This thesis did not investigate a non-uniform heat flux generated by an electronic component. For a non-uniform heat flux it may be necessary to then use the 3D analysis to find the temperature distributions within the heat sink.

A systematic thermal design methodology for both single-phase and two-phase micro-channel heat sinks under a low fixed liquid coolant flow rate was developed. An acceptable design region is first identified which encompasses all possible micro-channel dimensions corresponding to the prescribed dissipative heat flux and liquid coolant flow rate. Heat sink performance maps are then constructed within the acceptable design region. Finally, micro-channel dimensions yielding most desirable heat sink performance can be selected using the performance maps.

A single-phase heat sink testing system was designed, fabricated, and tested. The use of the thermal design methodology has been demonstrated experimentally for a single-phase heat sink. A two piece testing section has the drawback of a interfacial contact resistance which can cause higher temperatures than desired and so should be avoided in testing phases. The use of a single-phase heat sink can easily manage the cooling of an electronic device producing 80 W with an area of 1.1 × 2 inches while keeping the temperature well under 65 $^{\circ}C$.

A two-phase heat sink testing system was also designed. The technical merits of the design include the use of the FC-72 fluorinert for the coolant which will allow for saturated boiling to occur at a lower temperature than water, keeping the electronic device in a better temperature range, and not damaging the electronic components in the event of a leak.

Appendix A

Predictive tools for single-phase and two-phase micro-channel heat sinks

A.1 Single-phase

A.1.1 Heat transfer coefficient

The single-phase heat transfer coefficient, h_{sp}, [34] can be determined by:

$$h_{sp} = \{Nu_4 + 8.68\left(10^3 L^*\right)^{-0.506}\exp[(9.9776\ln(\beta) - 26.379)L^*]\} \left(\frac{Nu_3}{Nu_4}\right)\left(\frac{k_f}{d_h}\right)\left(\frac{\mu_w}{\mu_b}\right)^{-0.14} \quad \text{(A.1)}$$

where the non-dimensional distance is defined as

$$L^* = \frac{L}{Re_{sp} d_h Pr_f} \quad \text{(A.2)}$$

and the aspect ratio of the channel

$$\beta = \frac{W_{ch}}{H_{ch}} \quad \text{(A.3)}$$

and,

$$Nu_3 = 8.235(1 - 1.883\beta + 3.767\beta^2 - 5.814\beta^3 + 5.361\beta^4 - 2.0\beta^5) \tag{A.4}$$

and,

$$Nu_4 = 8.235(1 - 2.042\beta + 3.085\beta^2 - 2.477\beta^3 + 1.058\beta^4 - 0.186\beta^5) \tag{A.5}$$

A.1.2 Pressure drop components

The total single-phase pressure drop is $\Delta P = \Delta P_c + \Delta P_{sp,dh} + \Delta P_{sp,fh} + \Delta P_e$ (4.6) The pressure drop components are determined by the following: Pressure drop due to contract effects at the inlet, [43],

$$\Delta P_c = \frac{v_f}{2}(1 + K_c)\, G^2 \tag{A.6}$$

where,

$$K_c = 0.6740 + 1.2501\beta + 0.3417\beta^2 - 0.8358\beta^3 \tag{A.7}$$

Pressure drop due to the expansion effects at the exit, [43],

$$\Delta P_e = 0 \tag{A.8}$$

Pressure drop along the single-phase hydraulically developing region, [34],

$$\Delta P_{sp,dh} = \frac{2 f_{app,dh} G^2 L_{sp,dh} v_f}{d_h} \tag{A.9}$$

where,

$$L_{sp,dh} = \left(0.06 + 0.07\beta - 0.04\beta^2\right) Re_{in} d_h \tag{A.10}$$

$$f_{app,dh} = \frac{1}{Re_{sp}} \left[3.44(L^+_{sp,dh})^{-0.5} + \frac{K(\infty)/(4L^+_{sp,dh}) + f_{sp,fh}Re_{sp}(L^+_{sp,dh})^{-0.5}}{1 + C(L^+_{sp,dh})^{-2}} \right] \left(\frac{\mu_w}{\mu_b} \right)^{0.58} \quad \text{(A.11)}$$

$$f_{sp,fh}Re_{sp} = 24(1 - 1.355\beta + 1.947\beta^2 - 1.701\beta^3 + 0.956\beta^4 - 0.254\beta^5) \quad \text{(A.12)}$$

$$L^+_{sp,dh} = \frac{L_{sp,dh}}{Re_{sp}d_h} \quad \text{(A.13)}$$

$$K(\infty) = 0.6740 + 1.2501\beta + 0.3417\beta^2 - 0.8358\beta^3 \quad \text{(A.14)}$$

$$C = (0.1811 + 4.3488\beta - 1.6027\beta^2) \times 10^{-4} \quad \text{(A.15)}$$

Pressure drop along the single-phase hydraulically fully developed region, [34],

$$\Delta P_{sp,fh} = \frac{2[f_{sp,dh}(\mu_w/\mu_b)^{0.58}]G^2 L_{sp,fh} v_f}{d_h} \quad \text{(A.16)}$$

where,

$$L_{sp,fh} = L - L_{sp,dh} \quad \text{(A.17)}$$

A.2 Two-phase

A.2.1 Saturated flow boiling heat transfer coefficient

The two-phase heat transfer coefficient, h_{tp}, [13], [16],can be determined by:

$$h_{tp} = \frac{Nu_3}{Nu_4}(Eh_{sp4}) \quad \text{(A.18)}$$

Where, Nu_3 and Nu_4 are the same as in A.1 and can be found from A.4 and A.5.

$$h_{sp4} = Nu_4 \frac{k_f}{d_h} \tag{A.19}$$

and,

$$E = 1.0 + 6Bo^{1/16} + f(Bo)x_e^{0.65} \tag{A.20}$$

where,

$$Bo = \frac{q''_p}{Gh_{fg}} \tag{A.21}$$

$$f(Bo) = -5.3(1 - 855Bo) \tag{A.22}$$

$$q''_p = \frac{q''_{eff}(W_{ch} + W_w)}{W_{ch} + 2H_{ch}} \tag{A.23}$$

A.2.2 Pressure drop components

The two-phase pressure drop is $\Delta P = \Delta P_c + \Delta P_{sp,dh} + \Delta P_{sp,fh} + \Delta P_{tp} + \Delta P_e$ (4.7). ΔP_c, ΔP_e, $\Delta P_{sp,dh}$, and $\Delta P_{sp,fh}$ are the same as for single-phase and can be found with equations A.6, A.8, A.9, and A.16, respectively, the rest of the components can be found by:

[15]

$$\Delta P_{tp,f} = \frac{L_{tp}}{x_{e,out}} \int_0^{x_{e,out}} \frac{2f_f G^2 (1 - x_e)^2 v_f}{d_h} \phi_f^2 dx_e \tag{A.24}$$

Where,

$$L_{tp} = L - L_{sp} \tag{A.25}$$

$$f_f Re_f = 24(1 - 1.355\beta + 1.947\beta^2 - 1.701\beta^3 + 0.956\beta^4 - 0.254\beta^5) \tag{A.26}$$

and,

$$Re_f = \frac{G(1 - x_e)d_h}{\mu_f} \tag{A.27}$$

and,

$$\phi_f^2 = 1 + \frac{C}{X_{vv}} + \frac{1}{X_{vv}^2} \tag{A.28}$$

and,

$$C = 21[1 - \exp(-0.319 \times 10^3 d_h)](0.00418G + 0.0613) \tag{A.29}$$

and,

$$X_{vv} = \left(\frac{\mu_f}{\mu_g}\right)^{0.5} \left(\frac{1 - x_e}{x_e}\right)^{0.5} \left(\frac{v_f}{v_g}\right)^{0.5} \tag{A.30}$$

[15], [44]

$$\Delta P_{tp,a} = G^2 v_f \left[\frac{x_{e,out}^2}{\alpha_{out}} \frac{v_g}{v_f} + \frac{(1 - x_{e,out}^2)}{1 - \alpha_{out}} - 1\right] \tag{A.31}$$

Where,

$$\alpha_{out} = \frac{1}{1 + \left(\frac{1-x_{e,out}}{x_{e,out}}\right)\left(\frac{v_g}{v_f}\right)^{2/3}} \tag{A.32}$$

A.2.3 Critical heat flux CHF

The critical heat flux, q''_{max}, can be found by [18]:

$$q''_{max} = min(q''_{max1}, q''_{max2}) \tag{A.33}$$

$$q''_{max1} = \frac{q''_{p,m}(W_{ch} + 2H_{ch})}{W_{ch} + W_w} \tag{A.34}$$

Where,

$$q''_{p,m} = 33.43(Gh_{fg}) \left(\frac{\rho_g}{\rho_f}\right)^{1.11} We^{-0.21} \left(\frac{L}{d_e}\right)^{-0.36} \tag{A.35}$$

and,

$$We = \frac{G^2 L}{\sigma \rho_f} \tag{A.36}$$

and,

$$d_e = \frac{4W_{ch}H_{ch}}{W_{ch} + 2H_{ch}} \tag{A.37}$$

and,

$$q''_{max2} = \frac{\rho Q_t [c_{p,f}(T_{sat} - T_{in}) + h_{fg}]}{WL} \tag{A.38}$$

References

[1] D.B. Tuckerman and R.F.W. Pease. High-performance heat sinking for vlsi. *IEEE Electronic Devices Letters*, vol. EDL-2:126–129, 1981.

[2] T. Kishimito and T. Ohsaki. Vlsi packaging technique using liquid-cooled channels. *IEEE Transactions on Components, Hybrids, and Manufacturing Technology*, CHMT-9, no. 4:328–335, 1986.

[3] M.M. Rahman and F. Gui. Experimental measurements of fluid flow and heat transfer in microchannel cooling passages in a chip substrate. *Advances in Electronic Packaging*, ASME EEP-vol. 4:495–506, 1993.

[4] K. Kawano et al. Micro channel heat exchanger for cooling electrical equipment. *Proceedings of the ASME Heat Transfer Division*, ASME, HTD-vol. 361-3/PID-vol. 3:173–180, 1998.

[5] T.M. Harms et al. Developing convective heat transfer in deep rectangular microchannels. *International Journal of Heat and Fluid Flow*, vol. 20:149–157, 1999.

[6] W. Qu and I. Mudawar. Experimental and numerical study of pressure drop and heat transfer in a single-phase micro-channel heat sink. *International Journal of Heat and Mass Transfer*, 45:2549–2565, 2002.

[7] P.S. Lee et al. Investigation of heat transfer in rectangular microchannels. *International Journal of Heat and Mass Transfer*, 48:1688–1704, 2005.

[8] M.B. Bowers and I. Mudawar. High flux boiling in low flow rate, low pressure drop mini-channel and micro-channel heat sinks. *International Journal of Heat and Mass Transfer*, 37:321–332, 1994.

[9] T.S. Ravigururajan. Impact of channel geometry on two-phase flow heat transfer characteristics of refrigerants in microchannel heat exchangers. *ASME Journal of Heat Transfer*, 120:485–491, 1998.

[10] G.M. Roach et al. Low-flow critical heat flux in heated microchannels. *Nuclear Science and Engineering*, 131:411–425, 1999.

[11] L. Zhang et al. Measurement and modeling of two-phase flow in microchannels with nearly-constant heat flux boundary conditions. *Micro-Electro-Mechanical Systems (MEMS) - 2000*, MEMS-Vol.2:129–135, 2001.

[12] L. Jiang et al. Forced convection boiling in a microchannel heat sink. *Journal of Microelectromechanical Systems*, 10:80–87, 2001.

[13] et al. G.R. Warrier. Heat transfer and pressure drop in narrow rectangular channel. *Experimental Thermal and Fluid Science*, 26:53–64, 2002.

[14] et al. G. Hetsroni. A uniform temperature heat sink for cooling of electronic devices. *International Journal of Heat and Mass Transfer*, 45:3275–3286, 2002.

[15] W. Qu and I. Mudawar. Measurement and prediction of pressure drop in two-phase micro-channel heat sinks. *International Journal of Heat and Mass Transfer*, 46:2737–2753, 2003.

[16] W. Qu and I. Mudawar. Flow boiling heat transfer in two-phase micro-channel heat sinks–i. experimental investigation and assessment of correlation methods. *International Journal Heat and Mass Transfer*, 46:2755–2771, 2003.

[17] W. Qu and I. Mudawar. Flow boiling heat transfer in two-phase micro-channel heat sinks–ii. annular two-phase flow model. *International Journal of Heat and Mass Transfer*, 46:2773–2784, 20003.

[18] W. Qu and I. Mudawar. Measurement and correlation of critical heat flux in two-phase micro-channel heat sinks. *International Journal of Heat and Mass Transfer*, 47:2045–2059, 2004.

[19] M.E. Steinke and S.G. Kandlikar. An experimental investigation of flow boiling characteristics of water in parallel microchannels. *ASME Journal of Heat Transfer*, 126:518–526, 2004.

[20] J. Lee and I. Mudawar. Two-phase flow in high-heat-flux micro-channel heat sink for refrigeration cooling applications: Part i-pressure drop characteristics. *Journal of Heat and Mass Transfer*, 48:928–940, 2005.

[21] J. Lee and I. Mudawar. Two-phase flow in high-heat-flux micro-channel heat sink for refrigeration cooling applications: Part ii-heat transfer characteristics. *International Journal of Heat and Mass Transfer*, 48:941–955, 2005.

[22] R.J. Phillips. Micro-channel heat sinks. In *Advances in Thermal Modeling of Electronic Components.*

[23] et al. R.W. Knight. Optimal thermal design of forced convection heat sinks - analytical. *ASME Journal of Electronic Packaging*, 113:313–321, 1991.

[24] R.W. Knight. Heat sink optimization with application to microchannels. *IEEE Transactions on Components*, 15:832–842, 1992.

[25] S.F. Choquette. Optimum design of microchannel heat sinks. *Micro-Electro-Mechanical Systems (MEMS)*, DSC-vol. 59:115–126, 1996.

[26] D.Y. Lee and K. Vafai. Comparative analysis of jet impingement and microchannel cooling for high heat flux applications. *International Journal of Heat and Mass Transfer*, 42:1555–1568, 1999.

[27] J. Li and G.P. Peterson. Geometric optimization of a miro heat sink with liquid flow. *IEEE Transactions on Components and Packaging Technologies*, 29:145–154, 2006.

[28] S.V. Garimella and C.B. Sobhan. Transport in microchannels – a critical review. *Annual Review of Heat Transfer*, 13:1–50, 2003.

[29] G.L. Morini. Phase convective heat transfer in microchannels: a review of experimental results. *International Journal of Thermal Sciences*, 43:631–651, 2004.

[30] W. Qu and I. Mudawar. A systematic methodology for optimal design of two-phase micro-channel heat sinks. *ASME Journal of Electronic Packaging*, 127:381–390, 2005.

[31] T. S. Fisher and K. E. Torrance. Constrained optimal duct shapes for conjugate laminar forced convection. *International Journal of Heat and Mass Transfer*, 43:113–126, 2000.

[32] T. S. Fisher and K. E. Torance. Optimal shapes of fully embedded channels for conjugate cooling. *IEEE Transactions on Advanced Packaging*, 24:555–562, 2001.

[33] P. Wibulswas. *"Laminar-Flow Heat-Transfer in Non-Circular Ducts"*. PhD thesis, PhD Thesis, London University (1966)., 1966.

[34] R.K. Shah and A.L. London. *Laminar Flow Forced Convection in Ducts: a Source Book for Compact Heat Exchanger Analytical Data, Supl. 1.* Academic press, New York, 1978.

[35] P. Lee and S. V. Garimella. Thermally developing flow and heat transfer in rectangular microchannels of different aspect ratios. *International Journal of Heat and Mass Transfer*, 49:3060 – 3067, 2006.

[36] K. W. Shade K. R. Perkins and D. M. McEligot. Heated laminarizing gas flow in a square duct. *International Journal of Heat and Mass Transfer*, 16:98 – 104, 1973.

[37] A. R. Chandrupatla and V. M. K. Sastri. Laminar forced convection heat transfer of a non-newtonian fluid in a square duct. *International Journal of Heat and Mass Transfer*, 20:1315 – 1324, 1977.

[38] W. Qu and I. Mudawar. Analysis of three-dimensional heat transfer in micro-channel heat sinks. *International Journal of Heat and Mass Transfer*, 45:3973–3985, 2002.

[39] S. V. Patankar. *Numerical Heat Transfer and Fluid Flow.* Hemisphere, Washington DC, 1980.

[40] J.H. Ferziger and M. Peric.

[41] J. Lee and S. I. Mudawar. Two-phase flow in high-heat-flux micro-channel heat sink for refrigeration cooling applications: Part i — pressure drop characteristics. *International Journal of Heat and Mass Transfer*, 48:928 – 940, 2005.

[42] J. Lee and S. I. Mudawar. Two-phase flow in high-heat-flux micro-channel heat sink for refrigeration cooling applications: Part ii — heat transfer characteristics. *International Journal of Heat and Mass Transfer*, 48:941 – 955, 2005.

[43] R.D. Blevins. *Applied Fluid Dynamics Handbook.* Van Nostrand Reinhold Company, New York, 1984.

[44] S.M. Zivi. Estimation of steady-state steam void-fraction by means of the principle of minimum entropy production. *ASME Journal of Heat Transfer*, 86:247–252, 1964.